AN ABSTRACT OF THE THESIS OF

Xingjian Jiang for the degree of Master of Science in Atmospheric Sciences presented on November 25, 1986.

Title: Role of Oceanic Heat Transport Processes in CO_2-induced Warming: Analysis of Simulations by the OSU Coupled Atmosphere-Ocean General Circulation Model

Abstract approved: Michael E. Schlesinger

The OSU global coupled atmosphere/ocean general circulation model (A/O GCM) has been used to simulate the present ($1xCO_2$) climate and to investigate a CO_2-induced ($2xCO_2$) climate change. Previous analysis of the $1xCO_2$ simulation showed distinct errors in the simulated sea surface temperature (SST) and sea ice which were attributed primarily to the atmospheric GCM (AGCM). Analysis of the $2xCO_2$ simulation showed that the CO_2-induced warming penetrated into the ocean; this caused a delay in the equilibration of the climate system with an estimated e-folding time of 50-75 years. The present study has two objectives. The principal objective is to answer the question: By what pathways and through which physical processes does the simulated ocean general circulation produce the penetration of the CO_2-induced warming into the ocean? The secondary objective is to evaluate the performance of the oceanic GCM (OGCM) in the $1xCO_2$ simulation.

The comparison of the simulated $1xCO_2$ internal oceanic fields with the corresponding observations shows that although they are basically similar, there are distinct errors. Further analysis shows that these errors were generated by the OGCM during its spin-up integration prior to its coupling with the AGCM. This study thus shows that it is not sufficient to compare the simulated SST with the observed SST to evaluate the performance of the OGCM. It is also necessary to compare the simulated internal oceanic quantities with the corresponding observed quantities.

The global mean analysis of the CO_2-induced climate changes shows that the ocean gains heat at a rate of 3 W/m^2 due to the CO_2 doubling. This heat penetrates downward into the ocean predominantly through the reduction in the convective overturning. The zonal mean analysis shows that the surface warming increased from the tropics toward the midlatitudes of both hemispheres and penetrated gradually to the deeper ocean. The oceanic warming penetrated to a greater depth in the subtropics and mid-latitudes than in the equatorial region. A zonal mean heat budget analysis shows that the CO_2-induced warming of the ocean occurs predominantly through the downward transport of heat, with the meridional heat flux being only of secondary importance. In the tropics the penetration of the CO_2-induced heating is minimized by the upwelling of cold water. In the subtropics the heating is transported downward more readily by the downwelling existing there. In the high latitudes the suppressed convection plays the dominant role in the downward penetration of the CO_2-induced heating.

Role of Oceanic Heat Transport Processes in CO_2-induced Warming: Analysis of Simulations by the OSU Coupled Atmosphere-Ocean General Circulation Model

by

Xingjian Jiang

A THESIS

submitted to

Oregon State University

in partial fulfillment of
the requirements for the
degree of

Master of Science

Completed November 25 1986

Commencement June 1987

APPROVED:

Redacted for Privacy

Professor of Atmospheric Sciences in charge of Major

Redacted for Privacy

Chairman of the Department of Atmospheric Sciences

Redacted for Privacy

Dean of Graduate School

Date thesis is presented November 25 1986

Typed by Dee Dee Gibson for Xingjian Jiang

ACKNOWLEDGEMENTS

I am deeply indebeted to my major professor, Dr. Michael E. Schlesinger, for his invaluable guidance and support throughout the course of my study. Without his continous encouragement and help, I could never have finished this study.

I would like to thank William McKie and Robert Mobley for their indispensible assistance at the computing facility of the OSU Climatic Research Institute, and for their helpful discussions. Computing facilities were provided on the CRAY-1 computer by the National Center for Atmospheric Research, and on a PDP-11/70 by the OSU Climatic Research Institute. I would also thank Zongci Zhao and Jough-Tai Wang for their fruitful suggestions and discussions. Thanks to Mrs. Dee Dee Gibson for her skillful typing of the manuscript.

Special thanks to my parents and my fiancee, for their continous encouragement and care during my study at OSU. I also thank my friends Kaijun Lin and Min Wang for their help in preparing some of the figures. Finally, I would like thank the Government of the Peoples Republic of China for the financial support during my first year's study at OSU.

This study was suppported by the National Science Foundation under grant ATM-8511889.

TABLE OF CONTENTS

TABLE OF CONTENTS (Continued)

LIST OF FIGURES

LIST OF FIGURES (Continued)

LIST OF FIGURES (Continued)

LIST OF FIGURES (Continued)

LIST OF FIGURES (Continued)

LIST OF FIGURES (Continued)

Role of Oceanic Heat Transport Processes in CO_2-induced Warming: Analysis of Simulations by the OSU Coupled Atmosphere-Ocean General Circulation Model

1. INTRODUCTION

The OSU atmospheric general circulation model (AGCM) and oceanic general circulation model (OGCM) have been coupled and used to simulate both the present climate and the climate change induced by a doubling of the CO_2 concentration. Preliminary results of the coupled general circulation model (CGCM) have been given by Gates et al. (1985), Han et al. (1985) and Schlesinger et al. (1985).

The analysis by Gates et al. (1985) showed that the coupled model simulated a climate that was similar in most respects to that produced by the uncoupled AGCM. However, the study also showed that the January mean sea surface temperature (SST) simulated by the CGCM, when compared with observation, displayed several conspicuous discrepancies, particularly in the eastern tropical oceans, the western oceans of the Northern Hemisphere, and in the Southern Ocean. The study by Han et al. (1985) showed that the first two SST errors of the CGCM developed during the first several months after coupling the atmosphere and ocean GCMs. There was also an early indication of a steady SST warming and sea ice melting at high latitudes in the Southern Ocean. Both the annual mean and the seasonal variation of the simulated Antarctic sea ice area were found to be much smaller than that observed. Han et al. (1985) concluded that the SST errors of the CGCM simulation were

largely due to the errors introduced by the atmospheric component of the CGCM.

However, the studies by Gates et al. (1985) and Han et al. (1985) did not compare the simulated interior oceanic quantities to the observations, and did not, therefore, investigate the contribution of the oceanic component of the CGCM to any errors in these quantities. Thus, further analysis of the CGCM control ($1xCO_2$) simulation would be useful to evaluate the performance of the OGCM, and to understand the source for any errors thereby revealed. Therefore, one objective of the present study is to evaluate critically the performance of the OGCM in the $1xCO_2$ simulation by the CGCM.

The analysis of the CO_2-induced climate change by Schlesinger et al. (1985) showed that the evolution of the global mean temperature difference displayed a rapid warming of the atmosphere followed by a more gradual warming of the ocean and atmosphere. The CO_2-induced oceanic warming increased from the tropics toward the midlatitudes of both hemispheres at the surface, and penetrated to a greater depth in the subtropics and midlatitudes than in the equatorial region. The decrease with time in the warming rate of the atmosphere and sea surface was the result of the downward transport of heat into the interior of the ocean. However, this study only focussed on the global mean characteristics of the CO_2-induced warming, and did not address the question: by what pathways and through which physical processes does the simulated ocean general circulation produce the penetration of the CO_2-

induced warming into the ocean? Thus, the principal objective of the present study is to answer this question.

In the following chapter we give a brief review of the CO_2-induced climate change issue and some results for both the CO_2-induced equilibrium and transient climate change. Then a description of the OSU coupled model and its simulations is given together with some preliminary results. In Chapter 3 the comparison of the CGCM control simulation with observations in terms of oceanic quantities is given. Chapter 4 investigates the CO_2-induced ocean temperature changes and heat transport processes in terms of global and zonal means. Discussion of the results is given in Chapter 5 together with conclusions and recommendations for future work.

2. BACKGROUND

2.1. The CO_2-Climate Issue

Although carbon dioxide (CO_2) constitutes only a small percentage (0.035%) of the Earth's atmosphere, a change in its concentration can have a large effect on the global thermal regime. As some investigators have observed, the carbon dioxide concentration has been increasing as a result of the burning of fossil fuels and the large-scale clearing of forests. In order to estimate how much CO_2 has been added to the atmosphere as a result of human activity, various methods have been used to estimate the pre-industrial CO_2 level; these methods give values of 260 to 280 parts per million by volume (ppmv) (WMO, 1983). Measurements taken at Mauna Loa, Hawaii show that the CO_2 concentration has increased from 316 ppmv in 1959 to 342 ppmv in 1983 (Elliott et al., 1985), an 8% increase in 24 years. A study by Rotty (1983) also reported that the CO_2 concentration increased from 1860 to 1973 due to the nearly constant 4.6% per year growth rate in the consumption of fossil fuels, and has continued to increase since 1973 due to the diminished growth rate of 2.3% per year in fossil fuel consumption. An analysis of the future usage of fossil fuels predicts about an 80% chance that the CO_2 concentration will reach twice the pre-industrial value by the year 2100 (Nordhaus and Yohe, 1983).

As the CO_2 level increases, less of the temperature-dependent infrared radiation emitted by the Earth can escape through the atmosphere to space, while the amount of solar radiation absorbed

by the Earth is almost unchanged. It is to be expected that this so-called "greenhouse" effect will result in a warming of the average temperature of the Earth such that a balance between the solar heating and infrared cooling will be restored. However, it is also to be expected that the temperature change at any location will be higher, lower, or even of opposite sign from the average, and that there will be changes in other climate elements such as precipitation and cloudiness.

Although there is little doubt that an increase in the atmospheric CO_2 concentration will induce a change in the climate, the principal questions are: (1) What is the likely change in the equilibrium climate of the Earth for the projected CO_2 doubling, and (2) How long will it take for the Earth's climate to achieve that new equilibrium state? The answers to these questions have a direct bearing on both the impact and detection of a CO_2-induced climate change.

2.2. Methods for Studying the CO_2-Climate Issue

The degree of warming for a given increase in the CO_2 concentration is difficult to predict and will depend on the complex interactions of physical processes in the atmosphere-ocean-cryosphere-lithosphere-biosphere system which control climate change. In practice, there is simply no way to design a laboratory experiment, as one does in physics or chemistry, to simulate the CO_2-induced climate change because of the extreme complexity of the

climate system. An approach is to use the seasonal and regional patterns of past warm climates as "analogs" of a future warmer climate (e.g., Kellogg and Schware, 1982). However, because the causes of these past warm climates are not known, a future CO_2-induced climate might differ subtantially from the "analogs." This will in fact be the case unless the climate system warms in a similar manner regardless of the cause of the warming. Thus, past warmer climates may not be analogs of a future CO_2-induced climate change.

The atmosphere and ocean, however, are geophysical fluids which follow the fundamental laws of fluid mechanics and thermodynamics. These fundamental laws can be expressed in terms of partial differential equations that involve the field variables such as temperature, pressure and velocity. The representation of the Earth's climate system by these mathematical expressions of the fundmental physical laws is called a physically-based climate model. Because these models have been used on computers to simulate what a possible future CO_2-induced climate change might be like, it is useful to review them here before presenting their results in section 2.3.

A mathematical climate model is comprised of a set of mathematical equations that describe the behavior and interactions of the physical components of the Earth's climate system. Several types of climate model have been developed which differ in their intended use and in the comprehensiveness of their treatment of different climate system components. To understand fully the

impact of fossil fuel CO_2 on world climate, it is necessary to be able to predict the response of a broad range of climatological variables with sufficient spatial resolution to determine regional effects. The development of this capability requires the use of comprehensive coupled general circulation models (CGCMs) of the Earth's atmosphere and oceans. However, certain essential features of the problem can be illustrated with simpler energy balance models (EBMs) and radiative-convective models (RCMs) which are classified as thermodynamic climate models. These one-dimensional climate models have been used to estimate the change in the globally average temperature due to a doubling of CO_2.

2.2.1. Energy balance models

Energy balance models (EBMs) predict the change in temperature at the Earth's surface, T_s, from the requirement that $N = 0$, where N is the net energy flux expressed by $N = N(\vec{E}, T_s, \vec{I})$. Here $\vec{E}$ is a vector of quantities that are external to the climate system, that is, quantities whose change can lead to a change in climate, but which are independent of the climate. $\vec{I}$ is a vector of quantities that are internal to the climate system, that is, quantities that can change as the climate changes. An energy balance model can be expressed as (Schlesinger, 1985)

$$C_s \frac{\partial \Delta T_s}{\partial t} = \Delta Q - \frac{\Delta T_s}{G_o} (1 - G_o F) \qquad (2.1)$$

where C_s is the heat capacity of the climate system,

$$\Delta Q = \sum_i \frac{\partial N}{\partial E_i} \Delta E_i \tag{2.2}$$

is the change in N due to a change in one or more external quantity, E_i,

$$G_o^{-1} = - \frac{\partial N}{\partial T_s} \tag{2.3}$$

is the change in N due to the change in T_s alone, and

$$F = \sum_j \frac{\partial N}{\partial I_j} \frac{dI_j}{dT_s} \tag{2.4}$$

is the change in N due to the change in the internal variable through their dependence on T_s.

The transient solution of Eq. (2.1) is

$$\Delta T_s(t) = (\Delta T_s)_{eq} \left(1 - e^{-\frac{t}{\tau_e}}\right) \tag{2.5}$$

where

$$\tau_e = C_s \frac{G_o}{1-G_o F} \tag{2.6}$$

is the so-called "e-folding" time, and $(\Delta T_s)_{eq}$ is the equilibrium temperature change which is obtained as $t \to \infty$ and $\partial \Delta T_s / \partial t \to 0$. This $(\Delta T_s)_{eq}$ can be expressed as

$$(\Delta T_s)_{eq} = \frac{G_o}{1-G_o F} \Delta Q = \frac{G_o}{1-f} \Delta Q \tag{2.7}$$

or

$$(\Delta T_s)_{eq} = G_f \Delta Q \ , \tag{2.8}$$

where

$$G_f = \frac{G_o}{1-f} \tag{2.9}$$

is the gain (output/input) of the climate system and

$$f = G_o F \tag{2.10}$$

is the feedback.

2.2.2. Radiative-convective models

Radiative-convective models (RCMs) determine the equilibrium vertical temperature distribution for an atmospheric column and its underlying surface for given insolation and prescribed atmospheric composition and surface albedo. An RCM includes sub-models for the transfer of solar and terrestrial radiation (which are frequently identical to those used in GCMs), the turbulent heat transfer between the Earth's surface and the atmosphere, the vertical redistributions of heat within the atmosphere by dry or moist convection, and the atmospheric water vapor content and clouds. However, certain important feedback processes cannot be modelled in RCMs, including those between radiation and dynamics and those dependent on latitude, such as the ice albedo-temperature feedback.

2.2.3. General circulation models

General circulation models (GCMs) of the atmosphere are based on the set of mathematical equations which govern the physical behavior of the atmosphere, that is, the equation of motion, the

thermodynamic energy equation, the conservation equations for mass and water vapor, and the equation of state. Given an initial state of the model atmosphere and appropriate boundary conditions, the model is integrated forward in time to yield the atmospheric state at future times. The principal prognostic variables of an atmospheric GCM are the temperature, horizontal velocity and surface pressure. Since the general circulation of atmosphere is the large-scale, thermally-driven field of motion in which there are interactions between the heating and motion fields, several additional prognostic variables such as the water vapor mixing ratio, ground temperature, soil moisture and mass of snow on the ground must be added to simulate the heating.

Atmospheric GCMs have been used with prescribed sea surface temperature (SST) and sea ice to simulate the seasonal variation of climate. In these models the SST and sea ice thickness are taken from their observed values as given boundary conditions of the models. These models have been used to simulate single winter or summer months (Manabe et al., 1979; Schlesinger and Gates, 1980; Shukla et al., 1981), to simulate the annual cycle over multi-year integrations (Manabe and Hahn, 1981; Schlesinger and Gates, 1981; Hansen et al., 1984) and to reconstruct the most recent ice age (Gates, 1976a,b; Manabe and Broccoli, 1984, 1985a,b). However, to simulate a climate change such as that induced by increase of CO_2 level, it is not possible to treat the SST and sea ice distribution as given boundary conditions because the interaction and feedback among the atmosphere, ocean and sea ice components cannot be

ignored. Consequently, atmospheric GCMs have been coupled with different ocean and sea ice models.

The simplest ocean model is the swamp ocean model in which both the heat storage and heat transport of the ocean are ignored and the SST is diagnostically determined such that the net energy change at air-sea interface is zero (Manabe, 1969). These models cannot include either the diurnal or annual cycles of solar radiation because, if they did, the absence of oceanic heat storage would result in the freezing of the ocean in the nighttime hemisphere. To simulate climate and climatic change with the annual and diurnal cycles, atmosphere GCMs have been coupled to models of the uppermost layer of the ocean, the oceanic mixed layer, wherein the temperature is relatively uniform with depth. Prescribed-depth mixed layer models have been used with atmospheric GCMs by Hansen et al. (1984), Washington and Meehl (1984) to simulate the change in the equilibrium annual cycle induced by doubling the CO_2 concentration. A variable-depth mixed layer ocean model can also be used with atmospheric GCMs to simulate the climate change induced by rising CO_2 (and other forcing).

Although the models of the upper ocean include the storage of heat, and can also include the horizontal heat transport, they do not include the vertical transport of heat associated with the large-scale upwelling and downwelling of water. This vertical heat transport is of particular importance in the heat budgets of the equatorial and polar seas. For this reason models of the oceanic

general circulation have been developed which are the dynamical counterparts to the atmospheric GCMs. In oceanic GCMs the prognostic variables are the temperature, horizontal current and salinity, and the diagnostic variables include density, pressure and the vertical velocity. The solution of the governing equations is obtained numerically in a manner similar to that used for atmospheric GCMs. Oceanic GCMs have been coupled with atmospheric GCMs to simulate the present climate (Manabe, 1969; Wetherald and Manabe, 1972; Washington et al., 1980; Gates et al., 1985; and Han et al., 1985) and aspects of CO_2-induced climate change (Bryan et al., 1982; Schlesinger et al., 1985, and Bryan and Spelman, 1985).

2.3. Results for Equilibrium Climate Change

The CO_2-induced climate change in the equilibrium surface temperature calculated by various EBMs ranges from 0.24°C to 9.6°C. This wide range is due to differences in both ΔQ and G_f among the models, the latter reflecting the difficulty in EBMs of adequately treating those components of the climate system located away from the energy balance level (Schlesinger, 1985).

The equilibrium change in temperature simulated by RCMs for an increase in the CO_2 concentration shows a cooling in the stratosphere and a warming in the troposphere and at the Earth's surface. The equilibrium surface temperature warmings simulated by RCMs for a doubling of the CO_2 concentration range from 0.48°C to 4.20°C. This wide range represents the effects of water vapor feedback,

lapse rate feedback, surface albedo feedback, cloud altitude feedback, cloud cover feedback and cloud optical depth feedback. However, we cannot be highly confident of the results given by RCMs because they are not models of the global climate system and, more importantly, because RCMs must prescribe (or ignore) the behavior of much of that system. In particular, water vapor feedback is predicted assuming constant relative humidity, lapse rate feedback generally is predicted on the basis of baroclinic or moist adiabatic adjustment, and cloud feedbacks are predicted on the basis of greatly simplified cloud models.

Atmospheric GCMs coupled with swamp ocean models having zero heat capacity, no horizontal or vertical heat transport and without the seasonal insolation cycle give a surface air temperature warming of 1.3 to 3.9°C for a doubling of the CO_2 concentration. Atmospheric GCMs coupled with prescribed-depth mixed layer ocean models which have heat capacity, prescribed horizontal heat transports and the seasonal cycle give an annual mean surface air temperature warming of 3.5 to 4.2°C (Schlesinger and Mitchell, 1985).

Scaling the 3.5 to 4.2°C warming projected by the recent GCM simulations for a CO_2 doubling to the CO_2 increase from 1850 to 1980 suggests a warming of 1.1°C during this time period (Wigley and Schlesinger, 1985). However, the reconstructed surface air temperature record indicates a warming from 1850 to 1980 of about 0.6°C (Jones et al., 1986). Does this difference mean that the sensitivity of climate models is too large by a factor of two, for

example, due to their ignoring cloud optical depth feedback, or does this indicate that the actual response of the climate system lags the equilibrium response due to the thermal inertia of the ocean? In the next section we describe several studies that have addressed the latter question.

2.4. Results for Transient Climate Change

In the above we have discussed the long-term equilibrium climate warming that may result from a long-term and sustained change of the atmospheric CO_2 concentration. More recently, concern has been drawn to the non-equilibrium climate problem and focussed on the question: if the globally averaged temperature will eventually increase by a certain amount as a result of a specified increase in the atmospheric CO_2 concentration, how long will it take for that change to occur? The estimates are based on two methods, namely, the observed penetration of passive tracers into the ocean and simulations with climate models.

2.4.1. Estimates based on observations

To determine the rates at which substances are transported and mixed within the deep ocean is a fundamental problem for oceanographers. Direct measurements of all processes on a broad enough scale are impractical with present technology. Therefore one must resort to indirect methods such as the use of tracers,

particularly radioactive ones, whose distributions reflect oceanic horizontal and vertical transport processes.

The injection into the atmosphere of massive amounts of tritium (^{3}H) and carbon-14 (^{14}C) by the nuclear bomb tests of 1958-1962 provided two important tracers for estimating the air-sea exchange and the movement of the ocean water.

The GEOSECS program was started in the Atlantic Ocean in 1972-73 and then continued in the Pacific Ocean during 1973-74, and the Indian Ocean in 1978. The penetrations of the man-made tritium and carbon-14 were observed during an approximate 10-year period. The upper two panels of Fig. 2.1 show the vertical distribution of tritium from the GEOSECS program for the Western Atlantic and Pacific oceans. The Transient Tracers in the Ocean (TTO) program began in 1980 and additional ^{3}H and ^{14}C data were collected during this program. It has been found that deep wintertime convection in the North Atlantic Ocean has transported these tracers to great depth. The analysis of tritium data shows that it has progressed some 8 degrees farther south than was observed during the GEOSECS expeditions.

The distributions of tritium and carbon-14 in the world ocean have been studied by several investigators using modeling approaches (Rooth and Ostlund, 1972; Oeschger et al., 1975; Broecker et al., 1980; Sarmiento, 1983a,b). Most of the models are box-diffusion models in which the global ocean is treated as a fixed-depth mixed layer (the box) surmounting the thermocline wherein heat transport is parameterized as a diffusive process with

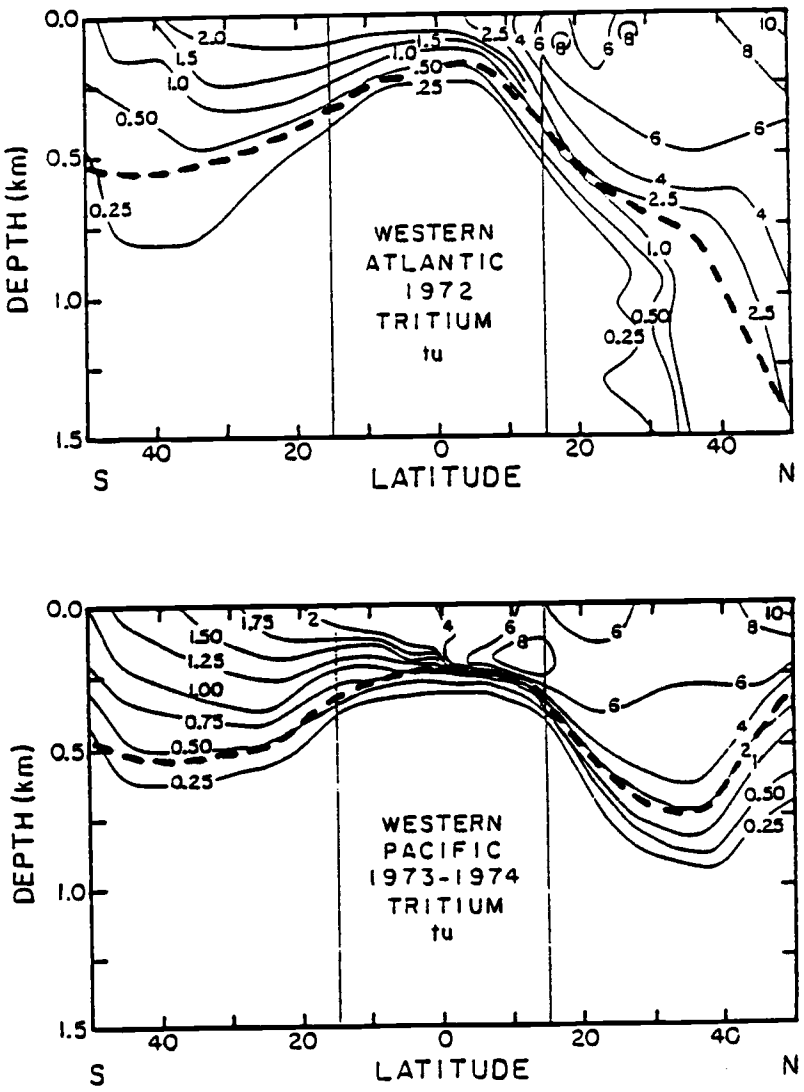

Fig. 2.1. Latitude-depth distribution of tritium in the western of Atlantic (a) and Pacific (b) oceans. (From: Broecker and Peng, 1982.)

a constant effective thermal diffusivity κ. Broecker et al. (1980) determined values of κ by using a box-diffusion model to reproduce the observed penetration of bomb-produced tritium and carbon-14 into the ocean. These authors found that $1.7 < \kappa < 3.3$ cm^2/s with a best estimate of $\kappa = 2.2$ cm^2/s.

Transient tracers, however, may not be a good indicator of the penetration of CO_2-induced heating into the ocean because they are purely passive insofar as their influence on the oceanic circulation, while the heating might change the buoyancy field and thereby the ocean circulation. In fact Kellogg (1983) has speculated that a CO_2-induced heating could penetrate into the ocean more slowly than a passive tracer due to the reduction in the ocean's vertical convection as a result of the heating, and would, thereby, reduce the lag time of the climate system. However, the model studies by Bryan et al. (1984) and Schlesinger et al. (1985) indicated that the penetration of a warming respectively prescribed as 0.5 °C and as induced by a CO_2 doubling would behave much like that of a passive tracer. On the other hand, the recent $4xCO_2$ study by Bryan and Spelman (1985) showed that this CO_2-induced warming suppressed high-latitude convection in the ocean with the result that the ocean took up heat twice as rapidly as a passive tracer. Thus, it is seen the transient tracer data may not be indicative of the vertical penetration of a large heat anomaly into the ocean.

2.4.2. Estimates based on model simulations

The transient response of the climate system to an abrupt CO_2 increase has been investigated with planetary energy balance, radiative-convective and general circulation models. These studies have obtained estimates of the e-folding time, τ_e, that range from 10 to 100 years (Hoffert et al., 1980; Bryan et al., 1982; Hansen et al., 1984; Bryan et al., 1984; Schlesinger et al., 1985). If τ_e is about 10 years, then the actual response of the climate system would be virtually in equilibrium with the instantaneous CO_2 concentration and the difference between the estimated 1.1°C warming from 1850 to 1980 and the actual value of 0.6°C would then likely mean that the gain of our climate models is twice that of nature. On the other hand, if τ_e is about 100 years, then the actual response of the climate system would not be in equilibrium with the instantaneous CO_2 concentration and the difference between the estimated 1.1°C warming from 1850 to 1980 and the actual value of 0.6°C would then likely be due to the slow thermal response of the ocean.

The factors that cause the wide range in τ_e have been discussed by Wigley and Schlesinger (1985) from their analytical solution for an energy balance climate/box-diffusion ocean model. Wigley and Schlesinger found that

$$\tau_e \sim G_f^2 \kappa , \qquad (2.11)$$

where G_f is again the gain of the climate system and κ is the effective thermal diffusivity of the ocean. This quadratic

dependence of τ_e on G_f helps explain why the early model studies with prescribed G_f obtained widely ranging values for τ_e. For example, a model with 4°C warming assumed for a CO_2 doubling will obtain a value of τ_e that is four times larger than the same model with an assumed sensitivity of 2°C for a CO_2 doubling. Furthermore, τ_e is dependent on the value of κ prescribed in these early model simulations. Consequently, to determine the value of τ_e requires a coupled global atmosphere/ocean GCM in which both the climate gain, G_f, and the oceanic heat transport are self-determined.

Pioneering simulations with a coupled atmosphere/ocean GCM of the transient climate response to abrupt increases in the CO_2 concentration have been performed at the Geophysical Fluid Dynamics Laboratory (GFDL) in Princeton by Bryan et al. (1982), Spelman and Manabe (1984), and Bryan and Spelman (1985). However, for computational economy in these simulations, the model atmosphere and oceans were taken as hemispherically-symmetric and periodic in the zonal direction with land and oceans occupying adjacent 60 degree longitudinal sectors.

The results of the transient study of the CO_2-induced climate change by Bryan et al. (1982) are shown in Figs. 2.2 and 2.3. The normalized response of the globally averaged sea surface temperature shown in Fig. 2.2 as a function of time is defined as

$$R = \frac{T - T_o}{T_\infty - T_o} \tag{2.12}$$

where T is the globally averaged sea surface temperature, T_o is its initial equilibrium value for the unperturbed CO_2 concentration, and T_∞ is its final equilibrium value for an increased atmospheric CO_2 concentration. The temperature response rose quickly during the first three years due to the heating of the mixed layer, and then increased more slowly due to the vertical transfer of heat to lower levels in the ocean.

Figure 2.3 shows the time-latitude variation of the zonally averaged normalized response of the sea surface temperature (upper panel) and surface air temperature (lower panel). These results show a relatively rapid warming of the atmosphere equatorward of 45° latitude, and a relatively slow response poleward of that latitude. The temperature response of the ocean was only half as rapid as that of the atmosphere due to the oceanic thermal inertia. After about 10 years the proportion of the atmospheric response became approximately independent of latitude. An e-folding time of about 25 years was obtained by Bryan et al. (1982) and Spelman and Manabe (1984) using this simplified coupled atmosphere/ocean GCM.

Bryan et al. (1984) used an uncoupled global oceanic GCM and found an e-folding time of about 100 years in response to a 0.5°C uniform temperature anomaly imposed at the sea surface. In this study, it was found that the penetration depths of a tracer and the positive heat anomaly were similar, while the penetration of the negative heat anomaly was 25% greater than that of the positive anomaly.

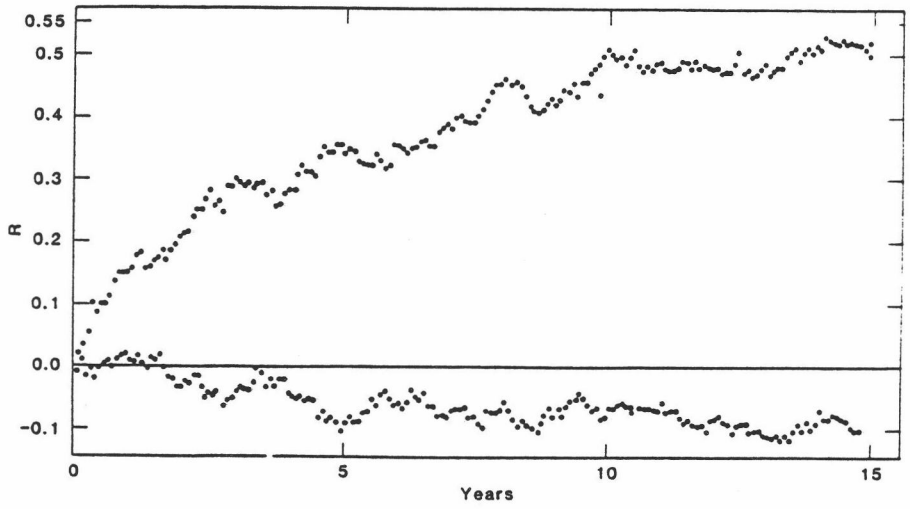

Fig. 2.2. The normalized response of the globally averaged sea surface temperature for a fourfold increase in the atmospheric CO_2 (upper curve); and for the calibration experiment for a normal CO_2 concentration (lower curve). (From: Bryan et al., 1982.)

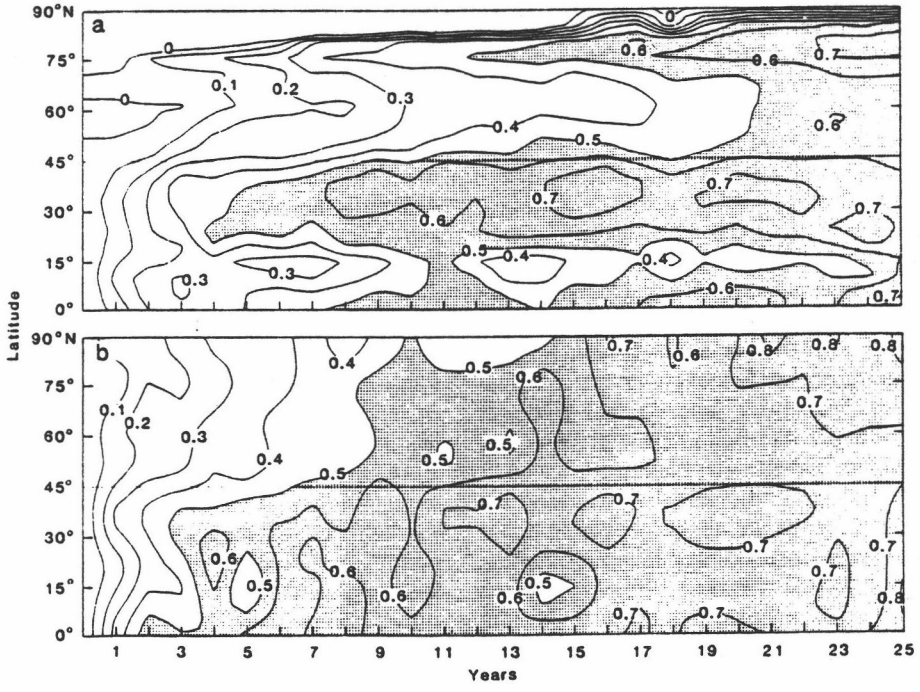

Fig. 2.3. Time-latitude variation of the zonally averaged normalized response of (a) sea surface temperature and (b) surface air temperature for a fourfold increase of atmospheric CO_2. (From: Bryan et al., 1982.)

Recently, Bryan and Spelman (1985) used a coupled atmosphere/ocean GCM to investigate the transient response of climate to a quadrupling of the atmospheric CO_2 concentration, and the behavior of a passive tracer. These authors showed that the CO_2-induced climatic warming suppressed convection in the ocean at high latitudes. The resultant blocking of the normal heat loss at high latitudes greatly enhanced the ability of the ocean model to take up heat, thereby slowing down the rate of warming of the ocean and atmosphere. With this convective feedback the ocean took up heat twice as rapidly as would be predicted from data for passive tracers injected at the surface.

Although the numerical studies described above have shown many important physical processes in the CO_2-induced climate change, they have been performed with models of the climate and ocean in which a variety of simplifications have been made. This includes the studies of Bryan et al. (1982), Spelman and Manabe (1984) and Bryan et al. (1985) in which the model was not global, did not have realistic geography, did not include the orography of the continents and that of the ocean bottom, and prevented the interaction of clouds. Consequently, these simplifications could significantly influence the simulated climate response through their effects on the oceanic heat transport and climate gain.

One calculation with a coupled atmosphere/ocean GCM without these limitations has been performed at Oregon State University. As described in the next section, this OSU model includes realistic

geography, realistic land and ocean-bottom topography, and interactive clouds.

2.5. Study with the OSU Atmosphere/Ocean GCM

The OSU atmospheric general circulation model (AGCM) and oceanic general circulation model (OGCM) have been developed over a period of years and have been tested separately in independent studies. In the following a brief description of the coupled model will first be given, and then selected results from the $1xCO_2$ and $2xCO_2$ simulations will be presented.

2.5.1. Description of the model and simulations

The atmospheric component of the coupled model is basically the same as the atmospheric general circulation model (AGCM) described by Schlesinger and Gates (1980, 1981), and documented by Ghan et al. (1982). It is a two-layer primitive equation GCM formulated using normalized pressure (sigma) as the vertical coordinate, with the top at 200 mb and surface orography as resolved by a horizontal spherical grid of 4 degrees latitude and 5 degrees longitude. The model predicts the atmospheric velocity (wind), temperature, surface pressure, water vapor mixing ratio, surface temperature, snow mass, soil water and clouds, and includes both the diurnal and seasonal variations of solar radiation.

The oceanic component of the coupled model is basically the same as the oceanic general circulation model (OGCM) described by

Han (1984a,b). The ocean model has six layers of unequal mass in the vertical, with the boundaries between the layers located at 50, 250, 750, 1550, 2750 and 4350 m. The OGCM is a primitive equation model of the world ocean that includes realistic lateral and bottom topography as resolved by its 4 degree by 5 degree latitude-longitude grid. However, in distinction from the OGCM described by Han (1984a,b) the current model version has been extended to include the Arctic Ocean. The sea ice model of the OGCM closely follows the basic formulation of Semtner (1976) and Parkinson and Washington (1979). The OGCM predicts the oceanic velocity (current), temperature and salinity (under the constraint of a prescribed surface skin concentration), and the mass of sea ice.

Figure 2.4 shows the vertical structure of the coupled model along with the primary quantities predicted during the simulation. Here T is the temperature, s the oceanic salinity, q the atmospheric water vapor mixing ratio, u and v are respectively the eastward and westward components of the horizontal wind or current, and $\dot{\sigma}$ and w are the atmospheric and oceanic vertical velocities, respectively. For the atmospheric model, $\dot{\sigma} = 0$ at $\sigma = 1$ and $\sigma = 0$ (200 mb), while for the oceanic model, $w = 0$ at $z = 0$ (surface) and $w = \vec{V}_H \cdot \nabla h$ at the oceanic bottom where $\vec{V}_H$ is the horizontal velocity and h is the ocean depth.

Figure 2.5 shows the horizontal resolution of the model, the orographies of the continents, and the depth of layers 1-3, 4-5, and 6 of the ocean model. The boundary conditions for the ocean are the no-slip condition at the bottom and the free-slip condition

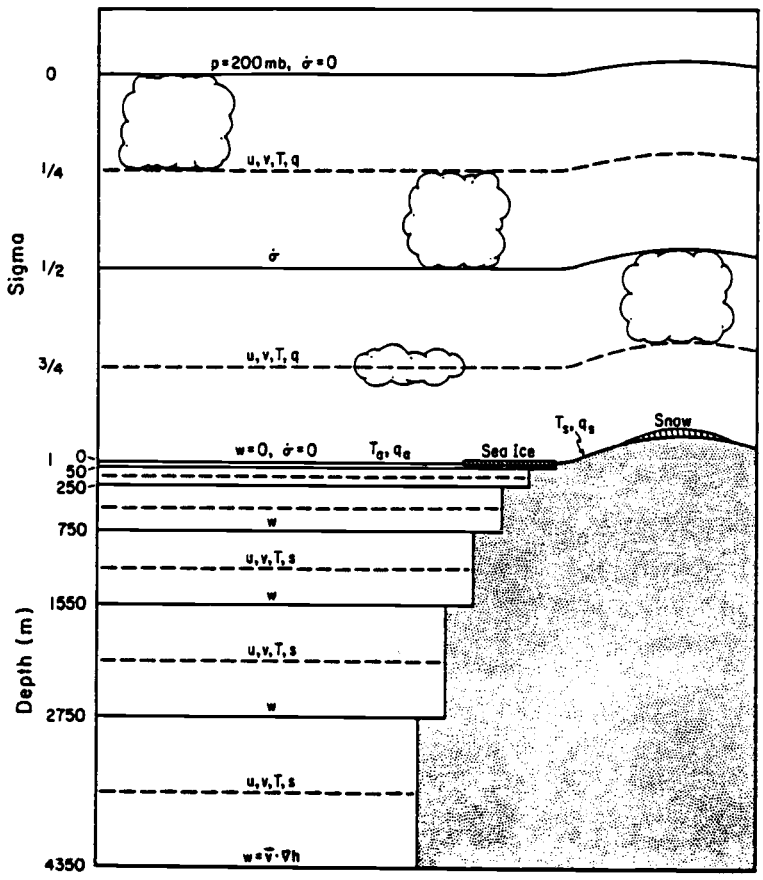

Fig. 2.4. The vertical structure of the coupled model, together with the primary dependent variables and boundary condition in the atmosphere and ocean. The atmospheric GCM uses normalized pressure ($\sigma = (p - p_t)/(p_s - p_t)$, where p is pressure, p_t the 200 mb pressure of the top of the model, and p_s the variable surface pressure) as a vertical coordinate and determines the horizontal velocity components u and v, the temperature T, and water vapor mixing ratio q at two tropospheric levels $\sigma = 1/4$(p ~ 396 mb), and $\sigma = 3/4$(p ~ 788 mb), the vertical velocity σ at $\sigma = 1/2$(p ~ 592 mb), the temperature T_a and water vapor mixing ratio q_a of the surface air, the temperature T_s of the Earth's non-water surface, the soil water q_s, the snow mass, and the cloudiness. The z-coordinate oceanic GCM determines the horizontal velocity components u and v, the temperature T and the salinity s at six levels intermediate to those at which the oceanic vertical velocity w is determined. The boundary condition $\sigma = 0$ is imposed at the model top and at the Earth's surface, while the condition $w = 0$ and $w = \bar{V}\cdot\nabla h$ are imposed at the ocean surface and ocean bottom, respectively, where V is the horizontal velocity and h is the ocean depth. (From Schlesinger et al., 1985.)

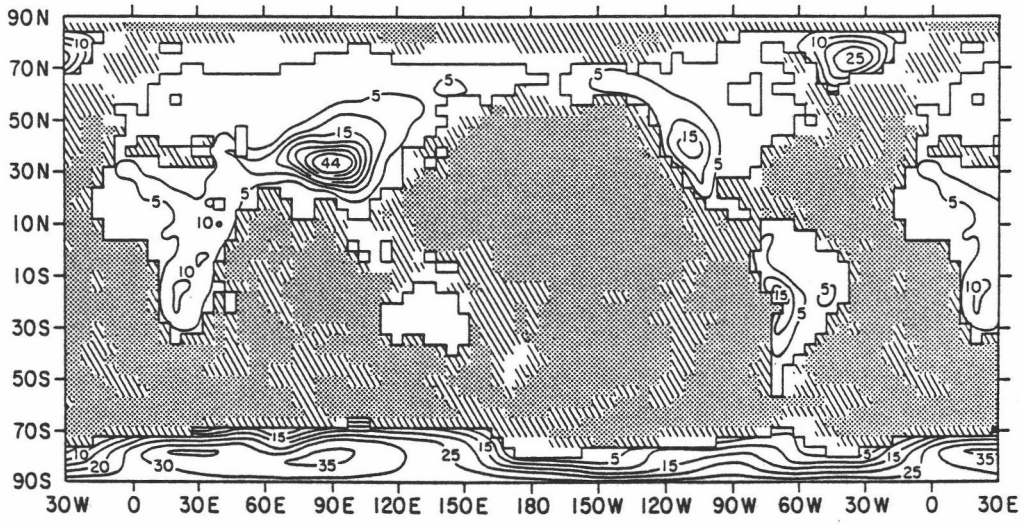

Fig. 2.5. The global domain of the coupled model, showing the continental outline and orography (in 10^2 m), and the oceanic depth resolved by the model's 4° by 5° latitude-longitude grid. Here the unshaded oceanic area is less than 750 m depth, the hatched area is between 750 m and 2750 m depth, and the shaded area is between 2750 m and 4350 m depth. (From Schlesinger *et al.*, 1985.)

at the lateral boundaries, with all but the surface assumed to be impermeable to salt and heat. The surface skin salinity was prescribed from climatology (Levitus, 1982) in order to minimize the uncertainties of the surface salt flux.

The coupling of the atmospheric and oceanic models is synchronous. The atmospheric model is integrated forward in time one hour subject to the sea surface temperature and sea ice thickness fields predicted by the oceanic model, and the latter is integrated forward in time one hour subject to the net surface heat flux and surface wind stress fields computed by the atmospheric model.

Figure 2.6 shows a schematic diagram of the experimental procedure. Two 20-year simulations have been performed with the coupled atmosphere/ocean model (CGCM) that differ only in their prescribed CO_2 concentrations. In the "control" or "1xCO_2" simulation the CO_2 concentration was taken to be constant in space and time and equal to 326 ppmv. In the "experiment" or "2xCO_2" simulation the concentration was doubled to 652 ppmv.

As shown schematically in Fig. 2.6, the initial states of the ocean and sea ice in the CGCM were taken from the results on 1 November of year 8 of an 11-year oceanic GCM integration with prescribed monthly atmospheric forcing. This simulation with seasonal forcing was itself initialized from an earlier 25-year simulation with annually-averaged atmospheric forcing with initial conditions from the observed ocean climatology of Levitus (1982). The initial conditions for the atmospheric component of the CGCM were

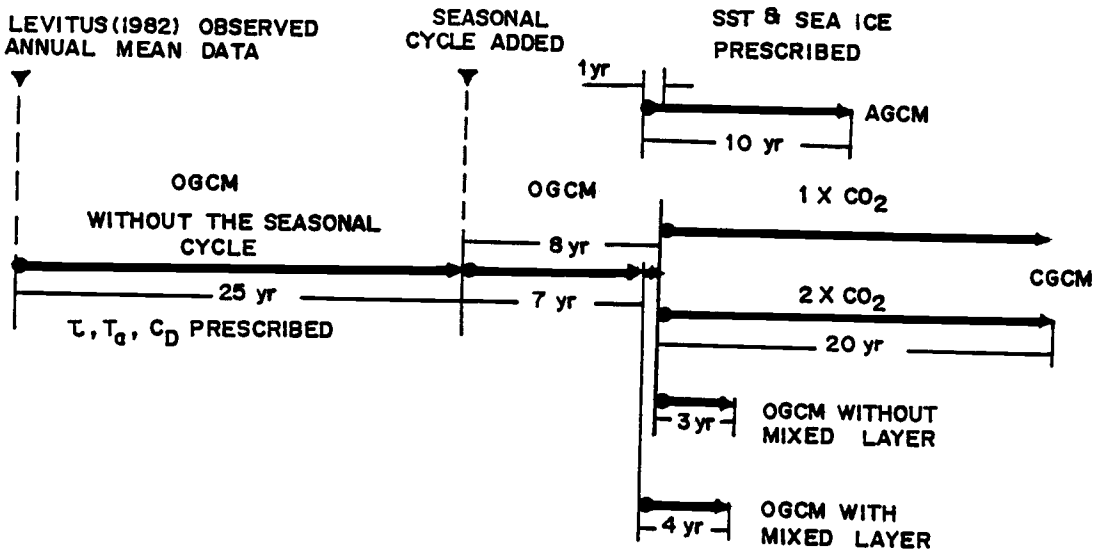

Fig. 2.6. Schematic diagram of the experimental procedure.

taken on 1 November of year 2 of a 10-year atmospheric control run in which the sea surface temperature (SST) and sea ice were prescribed from the observed monthly climatology, and the initial condition on 1 November was taken from an earlier AGCM simulation.

2.5.2. Results for the $1xCO_2$ simulation

The results for the $1xCO_2$ simulation of the OSU coupled atmosphere/ocean GCM have been analyzed by Gates et al. (1985) and Han et al. (1985).

The analysis by Gates et al. (1985) showed that the coupled model simulated a climate that is similar in most respects to that produced by the uncoupled atmospheric GCM. A major exception is that the coupled model fails to simulate a realistic seasonal distribution of surface wind and precipitation over the eastern tropical Pacific Ocean in association with the error in the simulated sea surface temperatures (SST). The latter for January are presented in Fig. 2.7. It can be seen that there is excessively cold water off the east coast of Asia and North America, and excessively warm water off the western coasts of the tropical continents. A similar warm error also causes a progressive loss of sea ice in the Southern Ocean, while the Arctic sea ice is realistically simulated.

The study by Han et al. (1985) showed that the SST errors of the CGCM in the eastern tropical oceans and in the western oceans of the Northern Hemisphere developed during the first several

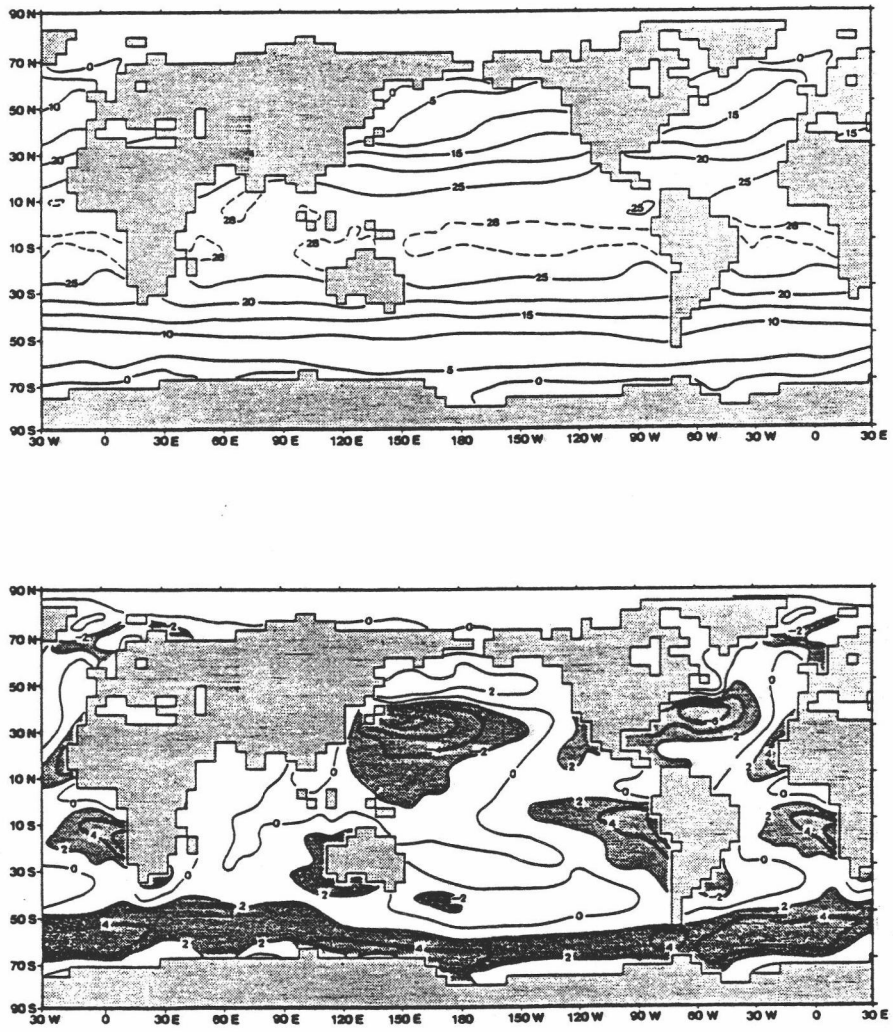

Fig. 2.7. The January sea surface temperature (in °C) simulated by the coupled model (above), and the departure of the simulated sea surface temperature from the observed (below, from Alexander and Mobley, 1976). Here simulation errors greater than 2°C in absolute value are shaded. (From Gates et al., 1985.)

months after coupling the atmosphere and ocean GCMs. There was also an early indication of a steady SST warming and sea ice melting at high latitudes in the Southern Ocean. Both the annual mean and the seasonal variation of the simulated Antarctic sea ice area were found to be much smaller than the observed. Interestingly, similar discrepancies have also been found in previous coupled model studies (Manabe et al., 1979; Washington et al., 1980), and thus appear to be characteristic errors of the CGCMs. A heat budget analysis of the upper ocean was made by Han et al. (1985) which indicated that the relatively rapid initial warming in the eastern tropical oceans was due to excessively large downward insolation during summer which may be caused by the underestimate of the subtropical stratocumulus clouds by the AGCM. The SST errors in the western ocean were found to be due mainly to the excessively large surface latent and sensible heat fluxes simulated there in winter as a result of the equatorward displacement of the semi-permanent Icelandic and Aleutian low pressure systems by the AGCM.

The critical evaluation by Han et al. (1985) of the $1xCO_2$ simulation by the OSU coupled GCM showed that the SST errors of the CGCM simulations were largely due to errors induced by the AGCM. However, Han et al. (1985) did not compare the simulated interior oceanic quantities to the observations and did not, therefore, investigate the contribution of the OGCM to any errors in these quantities. Consequently, further analysis of the CGCM $1xCO_2$ simulation would be useful to identify the performance of the OGCM and to understand the source for any error thereby revealed.

Therefore, one objective of the present study is the critical evaluation of the performance of the OGCM in the $1xCO_2$ simulation with the coupled atmosphere/ocean GCM.

2.5.3. Results for the $2xCO_2$ simulation

To investigate the transient response of the climate system, a $2xCO_2$ simulation was performed with the OSU coupled atmosphere/ocean general circulation model (Schlesinger et al., 1985). The evolution of the change in global mean temperature induced by the doubled CO_2 concentration is shown in Fig. 2.8 in terms of the vertical distribution of monthly-mean $2xCO_2 - 1xCO_2$ temperature differences for the atmosphere and ocean. The top panel of Fig. 2.8 shows an initially-rapid and vertically-uniform warming of the atmosphere followed by a progressively-slowing atmospheric warming. The bottom panel of Fig. 2.8 also shows an initially-rapid warming of the sea surface followed by a progressively-slowing warming. The decrease with time in the warming rate of the atmosphere and sea surface is the result of a downward transport of heat into the interior of the ocean.

The temperature change shown in Fig. 2.8, when normalized by the equilibrium temperature change, defines the climate response function for the global-mean temperature. Since the simulations were not of sufficient duration for the equilibrium change to have been obtained, estimates of the equilibrium temperature change and the vertical transport characteristics of the ocean were obtained

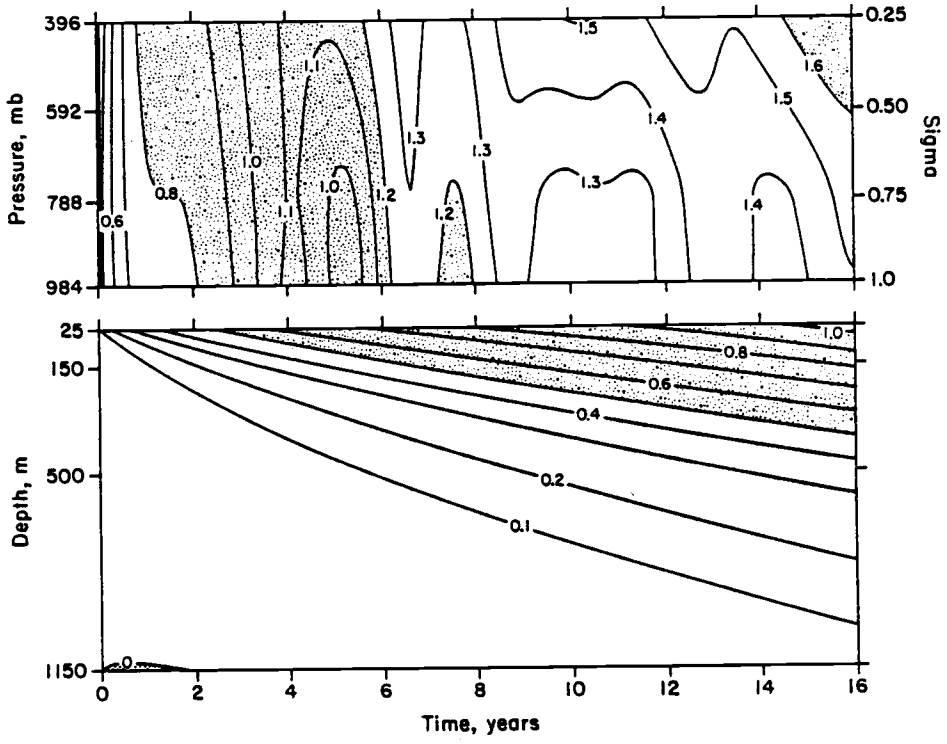

Fig. 2.8. Time-vertical distribution of the $2xCO_2 - 1xCO_2$ difference in the monthly-mean global-mean temperature (°C) of the atmosphere (above) and ocean (below) for the CGCM. Atmospheric warming between 0.8 - 1.2°C and larger than 1.6°C is indicated by light stipple, as is oceanic warming of 0.5 - 1.0°C, while oceanic cooling is indicated by heavy stipple. (From Schlesinger et al., 1985).

from a representation of the time evolution of Fig. 2.8 by a one-dimensional climate/ocean model (Schlesinger et al., 1985). The results from this climate/ocean model show that it is successful in reproducing the evolution of the $2xCO_2$-$1xCO_2$ temperature difference simulated by the coupled GCM. The results of a 200-year projection with the one-dimensional climate/ocean model, when normalized by the estimated equilibrium temperature change of T_{eq} = 2.82°C are presented in Fig. 2.9. It can be seen that the ocean surface layer reaches the e-folding temperature in about 75 years while the air temperature reaches the e-folding point about 50 years. These values of τ_e are closer to 100 years than to 10 years and are due to the sequestering of heat into the ocean by the downward transport from the surface.

The representation of the CGCM results by the one-dimensional climate/ocean model indicates that the gain of the coupled GCM is 0.72°C/(Wm^{-2}), the global-mean air-sea heat transfer coefficient is 8.0 Wm^{-2}/°C, and the effective oceanic thermal diffusivity κ is 3.2 cm^2/s at 50 m depth, 3.8 cm^2/s at 250 m, and 1.5 cm^2/s at 750 m. The mass-averaged κ = 2.25 cm^2/s is in agreement with the best estimate based on the observed penetration of bomb-produced tritium and ^{14}C into the ocean (Broecker et al., 1980).

Although the study by Schlesinger et al. (1985) focussed on the global-mean characteristics of the CO_2-induced warming, the results of the coupled GCM simulations show that warming is geographically distributed both at the Earth's surface and within the ocean. Fig. 2.10 shows the CO_2-induced oceanic warming increases

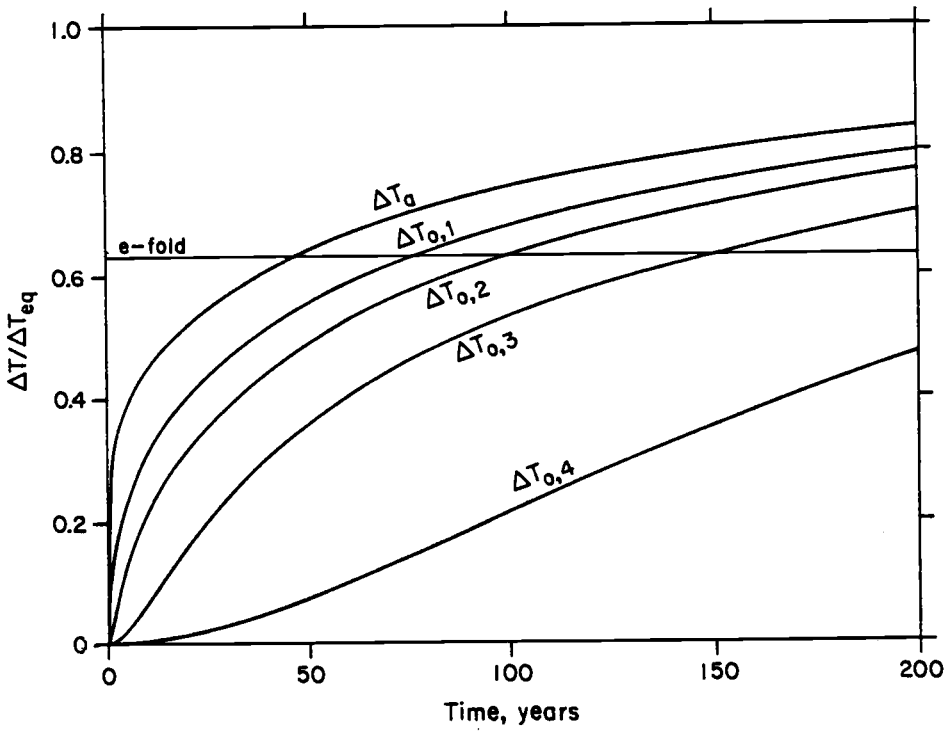

Fig. 2.9. Energy balance climate/multi-box ocean model projection to year 200 of the evolution of the $2xCO_2$-$1xCO_2$ difference in global-mean surface air temperature (T_a) and ocean layer temperature ($T_{o,k}$, k = 1, 2, 3, 4) as a fraction of the equilibrium temperature difference (T_{eq}). The horizontal line labelled e-fold indicates the level at which $\tau/\tau_{eq} = 1^{-1/e} - 0.63$. (From Schlesinger et al., 1985).

from the tropics toward the midlatitudes of both hemispheres at the surface and penetrates to a greater depth in the subtropics and midlatitudes than in the equatorial region. From the point of view of dynamic oceanography, it is fundamental to ask: By what pathways and through which physical processes does the simulated ocean general circulation produce the penetration of the CO_2-induced warming into the ocean? The second and principal objective of the present study is to answer this question.

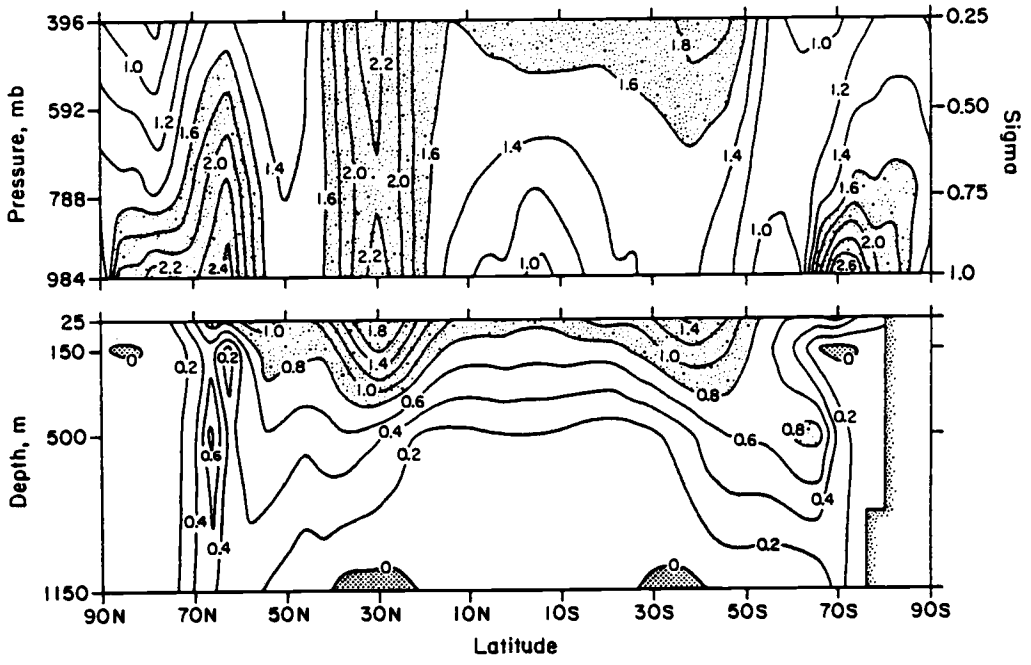

Fig. 2.10. Latitude-vertical distribution of the $2xCO_2-1xCO_2$ difference in the annual-mean zonal-mean temperature (°C) of the atmosphere (above) and ocean (below) for year 16. Atmospheric warming larger than 1.6°C is shown by light stipple, as is oceanic warming larger than 0.8°C, while oceanic cooling is indicated by heavy stipple. (From Schlesinger et al., 1985.)

3. COMPARISONS OF THE CGCM CONTROL RUN WITH OBSERVATIONS

The ability of a climate model to simulate the change of climate due to doubling CO_2 depends in part on how well it reproduces the present climate and in part on the response of the model to a change of boundary condition, namely, the doubling of CO_2. We cannot test the latter against reality until nature has "performed the experiment" in the decades ahead, but we can gain considerable confidence in the model if it reproduces the present climate reasonably well.

For the oceanic component of the coupled model, it is important to reproduce the observed temperature, salinity and circulation patterns insofar as they are known. In general, the oceanic general circulation patterns have been derived mainly from the distribution of sea water characteristics. The large-scale distributions of the temperature and salinity fields are analogous to a long-period, integrating current meter. These fields respond to the "average" advection-diffusion condition of the ocean. Because the observed temperature and salinity distributions are in a near-steady state, one can assume they respond to a circulation pattern nearly invariant in time and hence represent the general circulation. Thus, in order to assess the simulation capability it is important to compare the distributions of oceanic properties simulated by the coupled model with the corresponding observations.

The $1xCO_2$ results from the OSU coupled model have been presented by Gates et al. (1985) and were critically evaluated by

Han et al. (1985) as previously mentioned in Chapter 2. The latter study showed that the CGCM simulation errors for the sea surface temperature (SST) were largely due to errors induced by the AGCM. However, Gates et al. (1985) and Han et al. (1985) did not compare the simulated interior oceanic quantities to the corresponding observed quantities, and did not, therefore, investigate the contribution of the OGCM to any such errors. The objective of this chapter is to compare the CGCM simulation of the interior oceanic quantities with the corresponding observations.

Considering the long oceanic thermal adjustment time scale (100 - 1000 years), the present 20-year coupled integration is not long enough to yield a true oceanic equilibrium. However, a close inspection of the time behavior of the coupled system reveals a relatively rapid initial adjustment of the upper three layers, accompanied by very small changes in the deeper ocean. By year 16 of the coupled integration the ocean surface layer has already reached near equilibrium except at high latitudes in the Southern Ocean (Han et al., 1985 and Schlesinger et al., 1985). Therefore, because the OGCM was initialized with the observed zonal mean quantities, any deviation of the simulation from the initial conditions represents an error introduced by the OGCM during its spinup and/or by the CGCM after coupling.

As a first step in a comprehensive analysis of the $1xCO_2$ simulation, we restrict attention here to the annual zonal mean fields of selected oceanic quantities and heat transport processes near the middle of the 20-year integration, namely for year 12.

Because of the large differences in the depths of the ocean model's layers, the results are presented here in figures having two panels, each of which is linear in depth, one for the surface to 1150 m, and the other from 1150 to 3550 m. In the following we shall first compare the annually and zonally averaged potential temperature, salinity and potential density simulated by the CGCM, and by the uncoupled OGCM, with the corresponding observations of Levitus (1982). Then we shall present some additional fields which are of interest but for which there are no observations.

3.1. Potential Temperature, Salinity and Potential Density

Before comparing the simulated and observed fields, it is useful to present a few definitions and the nomenclature used below.

3.1.1. Definitions and nomenclature

Let T, s and p represent the temperature (°C), salinity (parts per thousand or o/oo) and pressure (decibars) of a parcel of sea water, respectively. Because sea water is slightly compressible, a sample brought to the surface from depth will expand and tend to cool. The temperature of a sample brought to the surface adiabatically without thermal contact with the surrounding water will therefore be colder than the surrounding water. The potential temperature of a parcel of sea water is the temperature that the parcel would have if it were displaced adiabatically to the sea

surface. This value is used to eliminate the compressibility effect when comparing water samples at significantly different depths or when considering vertical motions over considerable depth ranges.

The computation of potential temperature θ used in the OGCM is that formulated by Bryden (1973),

$$\theta = T - \int_{p_a}^{p} \Gamma \, dp$$

$$= T - \sum_i \sum_j \sum_k A_{ijk} p^i (s - 35)^j T^k, \qquad (3.1)$$

where Γ is the adiabatic lapse rate, p_a is the atmospheric pressure at the sea surface, and the A_{ijk} are constants.

The density of sea water, ρ, is a function of the temperature, salinity and pressure

$$\rho = \rho(s,T,p) \quad . \qquad (3.2)$$

Following Eckart (1958), the density is calculated from

$$\rho = \rho_o \left[1 + \frac{K}{p + p_o} \right]^{-1} \quad , \qquad (3.3)$$

where

$$p_o = 5890 + 38\ T - 0.375\ T^2 + 3\ s$$

$$\rho_o = 1.4327 \qquad (3.4)$$

and $$K = 1779.5 + 11.25\ T - 0.0745\ T^2 - (3.8 + 0.01\ T)\ s$$

where T is in °C, s in o/oo, p and p_o are in atmospheres (1 atmosphere = 1.03323 kg/cm = 1.01325 bar), and ρ_o is in g/cm^3.

For the range of temperature and salinity observed in the world ocean, density changes due to the compressibility of sea water are much larger than density changes due to either thermal expansion or saline expansion. The quantities sigma-t, σ_t, and potential density, σ_θ, are used to exclude the effects of changes in temperature and salinity on the density of a parcel of sea water. The definition of σ_t for a parcel of sea water with temperature T and salinity s is

$$\sigma_t = [\rho(s,T,0) - 1] \times 10^3 \quad , \tag{3.5}$$

and represents the density the parcel would have at the pressure of the sea surface which is taken as zero. The potential density is expressed as

$$\sigma_\theta = [\rho(s,\theta,0) - 1] \times 10^3 \quad , \tag{3.6}$$

and represents the density the parcel would have if it were adiabatically brought to the sea surface. In Eqs. (3.5) and (3.6) unity is subtracted from the density and the result multiplied by 10^3 for numerical convenience. Since the density values for most of the world ocean range from 1.01 to 1.05 g/cm^3, typical values of σ_t and σ_θ range from 10 to 50.

In the deep water the temperature often increases slowly with depth due to the effect of increasing pressure. When considering oceanic situations where considerable changes in the depth of water masses occur, it is best to present the potential temperature rather than the temperature to eliminate the effect of the depth change. Thus, potential temperature is usually used to represent

the oceanic thermal field. For a similar reason the potential density field is chosen to represent the density field.

3.1.2. Simulated and observed potential temperature

Figure 3.1 shows the zonal mean potential temperature θ averaged over year 12 of the CGCM control together with the observed annual mean potential temperature from Levitus (1982). The observed potential temperatures decrease from low latitude to high latitudes and from the ocean surface to the deep layers. The largest horizontal gradients of potential temperature occur in the subtropical and middle latitudes. The largest vertical gradients occur from about 50 to 500 m depth which is the location of thermocline zone. The warmest oceanic water is found in the tropical surface layer. Two warm tongues are evident which extend from the low-latitude upper ocean toward the high-latitude deep ocean in both hemispheres. The observed potential temperature pattern clearly shows the Antarctic Bottom Water contributed by the Weddell Sea and the North Atlantic Deep Water contributed by the Norwegian-Greenland seas. The local potential temperature minimum that is found near the equatorial upper ocean may be caused by the upwelling in that region.

The differences between the simulated and observed potential temperatures are shown in Fig. 3.2 together with the differences between the potential temperature simulated during year 11 of the uncoupled OGCM (see Fig. 2.6) and the observations. This figure

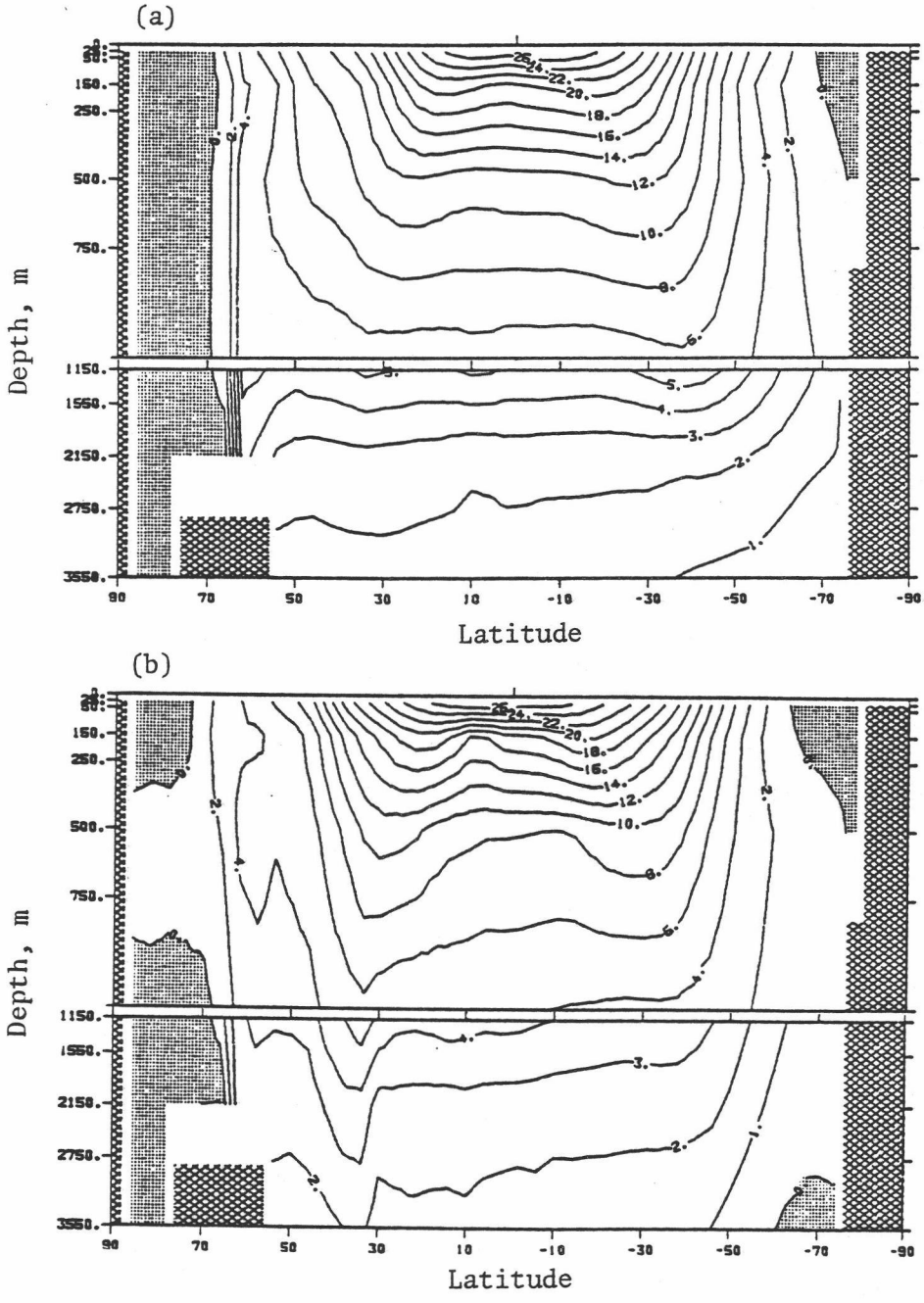

Fig. 3.1. Latitude-depth distribution of the annual zonal mean oceanic potential temperature θ (°C) for: (a) year 12 of the CGCM control run, and (b) the observations of Levitus (1982). Negative values are shaded.

shows that the zonal mean ocean temperatures simulated by the coupled model have drifted from their initial conditions which were the observed zonal mean temperatures. In particular, the simulated temperatures are warmer than the observed temperatures everywhere except in the upper ocean near 30°N and north of 65°N, and in the deep ocean at low latitudes. The largest warming is located in the second and third layers of the ocean model, while the largest cooling occurs near the surface layer.

It is of interest to determine what part of these errors was contributed by the uncoupled OGCM, and what part was due to the coupling of the OGCM with the AGCM. The results of year 11 of the OGCM control are presented here rather than year 8 because the history data were not saved for the early years of the uncoupled OGCM. However, it is likely that the oceanic properties did not change much from year 8 to year 11 of the uncoupled OGCM simulation so that year 11 should be similar to year 8. Consequently, comparison of the upper and lower panels of Fig. 3.2 shows that most of the simulation errors were already introduced by the uncoupled OGCM. Following coupling, these errors increased in the middle and high latitudes of Northern and Southern Hemisphere and decreased in the equatorial region.

Further evidence of the errors introduced by the uncoupled OGCM is provided by the upper panel of Fig. 3.3 which shows the differences between the potential temperatures simulated by the uncoupled OGCM without seasonal cycles at the end of year 25 (see Fig 2.6) and the observed potential temperatures. A comparison of

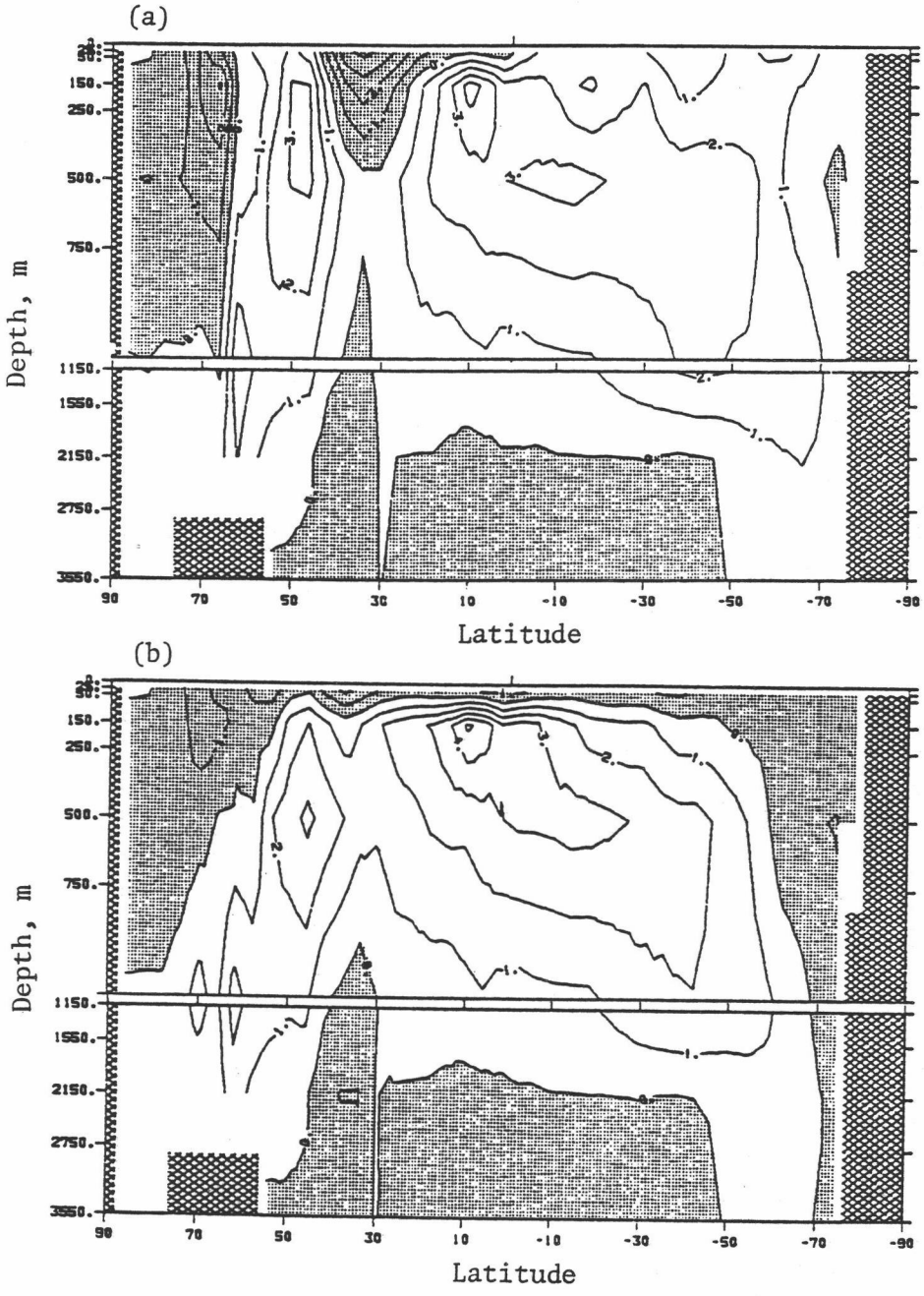

Fig. 3.2. Latitude-depth distribution of the difference in the annual zonal mean oceanic potential temperature θ (°C) for: (a) year 12 of the CGCM control run minus the observations, and (b) year 11 of the OGCM run minus the observations. Negative values are shaded.

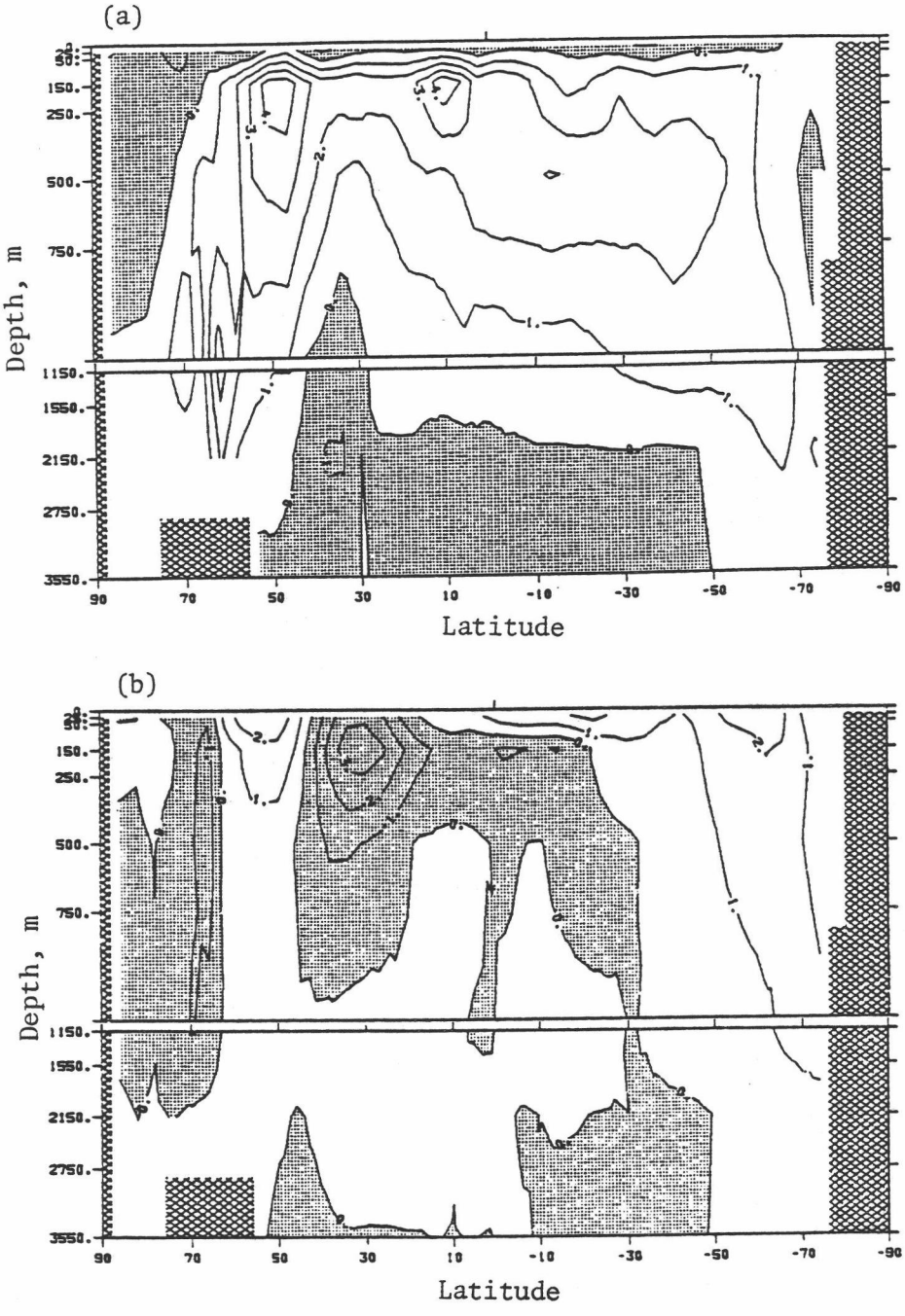

Fig. 3.3. Latitude-depth distribution of the difference in the annual zonal mean oceanic potential temperature θ (°C) for: (a) year 25 of the OGCM run without seasonal cycles minus the observations, and (b) year 12 of the CGCM control run minus year 11 of the OGCM run. Negative values are shaded.

this panel with the lower panel of Fig. 3.2 shows that the temperature errors already occurred during the OGCM simulation without the seasonal cycle, with little additional error being introduced by the OGCM run with the annual cycle.

The errors introduced by the coupling are displayed in Fig. 3.3b which shows the potential temperature difference between year 12 of the coupled run and year 11 of the uncoupled OGCM. It is seen that the largest differences occurred in the second layer near 35°N. This location corresponds to that of the SST errors off the east coast of Asia and North America as shown in Fig. 2.7. Consequently, the error shown near 30°N in Fig. 3.3b represents the penetration into the ocean of the SST error, the latter as a result of the excessively large surface latent and sensible heat fluxes associated with the error in the position of the Icelandic and Aleutian lows simulated by the atmospheric component of the CGCM (Han et al., 1985). This penetration of the cold SST error into the ocean was likely the result of excessively large convection and downwelling processes in those regions.

3.1.3. Simulated and observed salinity

The annual zonal mean salinities simulated by the CGCM for year 12 are shown in Fig. 3.4 together with the observed annual mean salinity from Levitus (1982). In the observed field a salinity maximum is located in the upper layers of the ocean in the subtropics of each hemisphere. These observed subtropical salinity

maxima are the result of the excess of surface evaporation over precipitation in these areas. The model simulates these subtropical salinity maxima reasonably well, but it should be recalled that the OGCM is helped in doing so by the prescribed sea surface salinity boundary condition. The observed salinity exhibit minima in the subpolar regions as a result of the excess of precipitation over evaporation in these regions. In the observations the Antarctic Intermediate Water is clearly represented by a low-salinity tongue which first extends downward and northward in the region of 60°S to 70°S. The model simulates this Antarctic Intermediate Water, but not as distinctly as the observed. The main contribution to the observed high-salinity tongue which extends northward and then downward from the ocean surface near 25°N to very deep layers is in part due to the high salinity water sinking from the ocean surface layer along constant density surfaces (isopycnals), and in part due to the Mediterranean outflow. The major differences between the simulated and observed salinities are discussed below.

The salinity differences between year 12 of the CGCM control run and the observations are shown in Fig. 3.5 together with the differences between year 11 of the uncoupled OGCM run and the observations. The distribution of the difference between the CGCM simulation and the observations shows that the model overestimates the salinity in the middle ocean layers from the tropical to the middle latitudes of the Southern Hemisphere; the latter represents the model's error in simulating the Antarctic Intermediate Water.

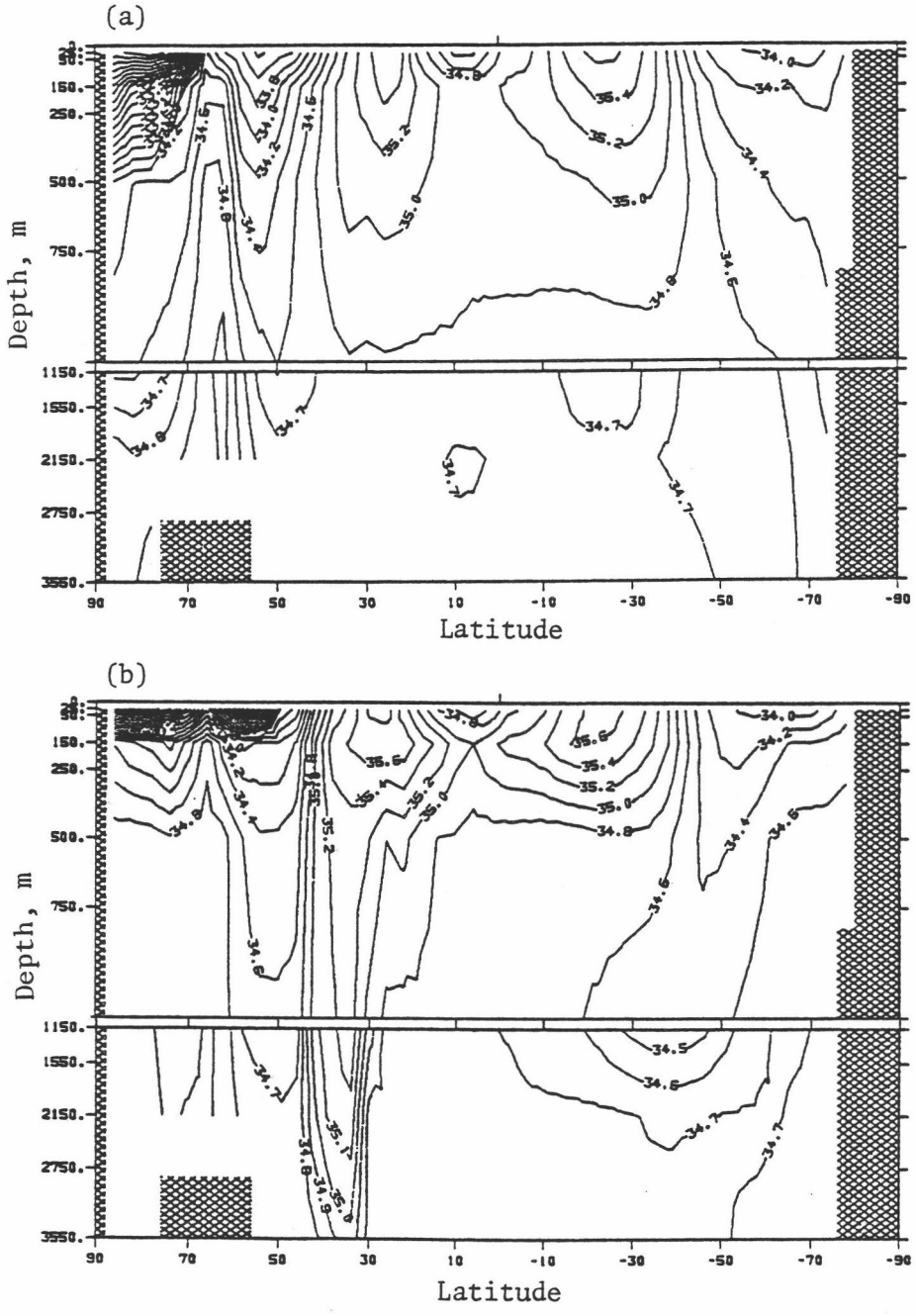

Fig. 3.4. Latitude-depth distribution of the annual zonal mean oceanic salinities (‰) for: (a) year 12 of the CGCM control run, and (b) the observations of Levitus (1982).

The model also overestimates the salinity in the surface layer near 55°N. The model underestimates the salinity everywhere else, with the largest errors occurring in the north polar region and throughout the entire depth of the ocean near 35°N. The latter discrepancy is likely due to the treatment of the Mediterranean Sea in the model as being isolated from the North Atlantic Ocean. The lower panel of Fig. 3.5 indicates that, as for the potential temperature, most of the salinity errors were already introduced before the OGCM was coupled with the AGCM.

Further evidence of the errors introduced by the uncoupled OGCM is provided by the upper panel of Fig. 3.6 which shows the differences between the salinity simulated by the uncoupled OGCM without seasonal cycles at the end of year 25 (see Fig. 2.6) and the observed salinity. A comparison of this panel with the lower panel of Fig. 3.5 shows that the salinity error occurred during the OGCM simulation without the seasonal cycles with little additional error being introduced by the OGCM run with the annual cycle. These results show that the prescription of the surface salinity as a boundary condition is not effective in constraining the simulated salinity below the surface to agree with the observed salinity. Furthermore, these salinity errors together with the potential temperature errors suggest that the simulated oceanic circulation differs from the actual (unobserved) oceanic circulation.

The salinity differences between year 12 of the coupled run and year 11 of the uncoupled OGCM are shown in the lower panel of

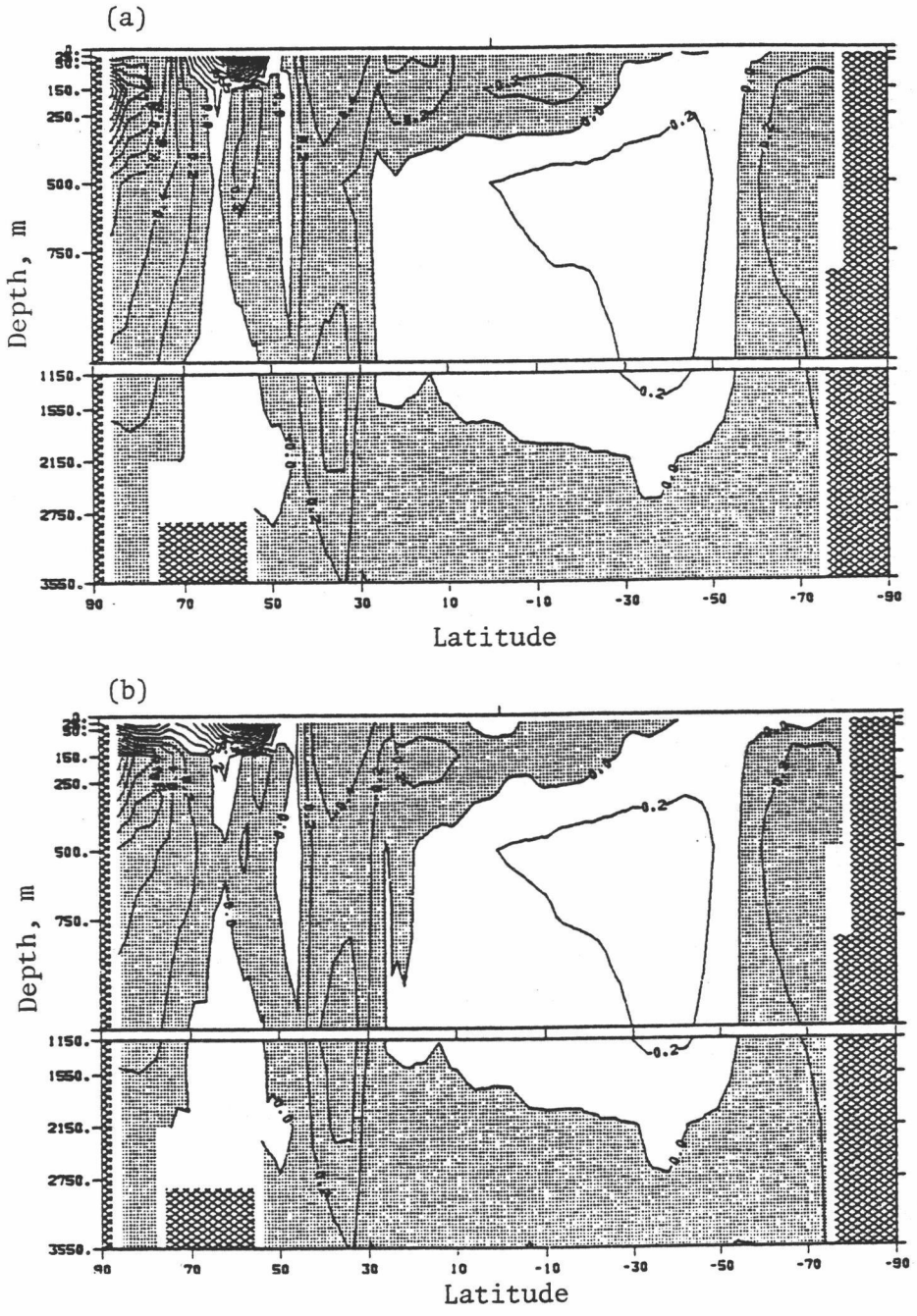

Fig. 3.5. Latitude-depth distribution of the difference in the annual zonal mean oceanic salinities (‰) for: (a) year 12 of the CGCM control run minus the observations, and (b) year 11 of the OGCM run minus the observations. Negative values are shaded.

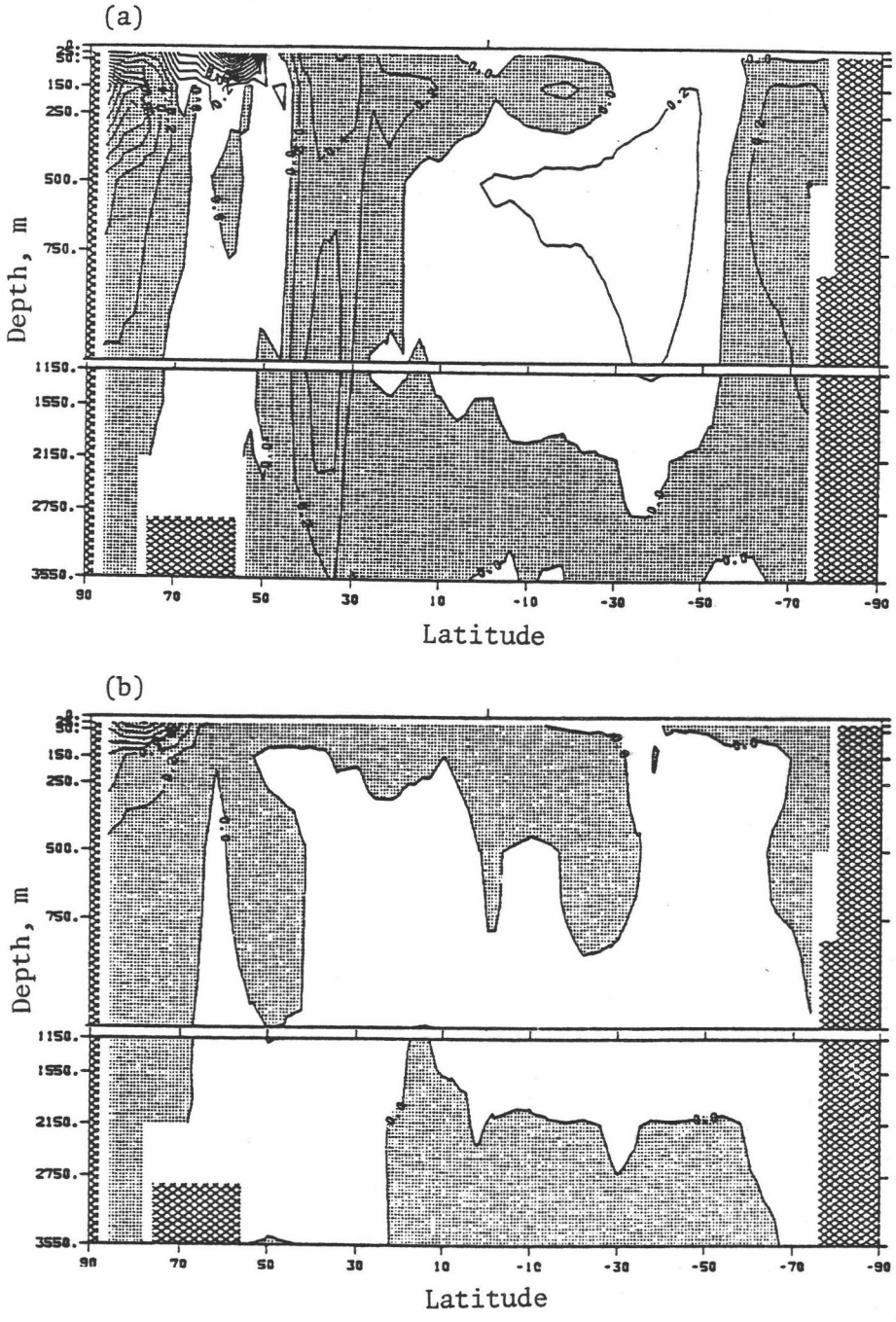

Fig. 3.6. Latitude-depth distribution of the difference in the annual zonal mean oceanic salinities (‰) for: (a) year 25 of the OGCM run without seasonal cycles minus the observations, and (b) year 12 of the CGCM control run minus year 11 of the OGCM run. Negative values are shaded.

Fig. 3.6. This figure shows that coupling the AGCM and OGCM introduced only small errors in the salinity field everywhere except in the north polar region.

3.1.4. Simulated and observed potential density

Figure 3.7 shows the annual zonal mean potential density σ_θ simulated by the CGCM for year 12 along with the observed σ_θ based on the data of Levitus (1982). The observed potential density field is quite similar to the observed potential temperature field (Fig. 3.1b) with extrema that are associated with features of the observed salinity field (Fig. 3.4b). The observed σ_θ increases from low to high latitudes and from the surface to the deep ocean except in the north polar region where σ_θ decreases toward the pole. The smallest values of potential density are located at the surface in the tropics with a minimum centered in the Northern Hemisphere that is associated with the small salinity values in that region (Fig. 3.4b). Near 55°N and in the Arctic there are two areas of small potential density in the surface layer which are also related to minima in the salinity distribution. Two potential density ridges are found near 40°N and 65°N which are associated with the large values of salinity at these latitudes.

The simulated potential density is similar to the observed potential density in most of the oceans. However the observed

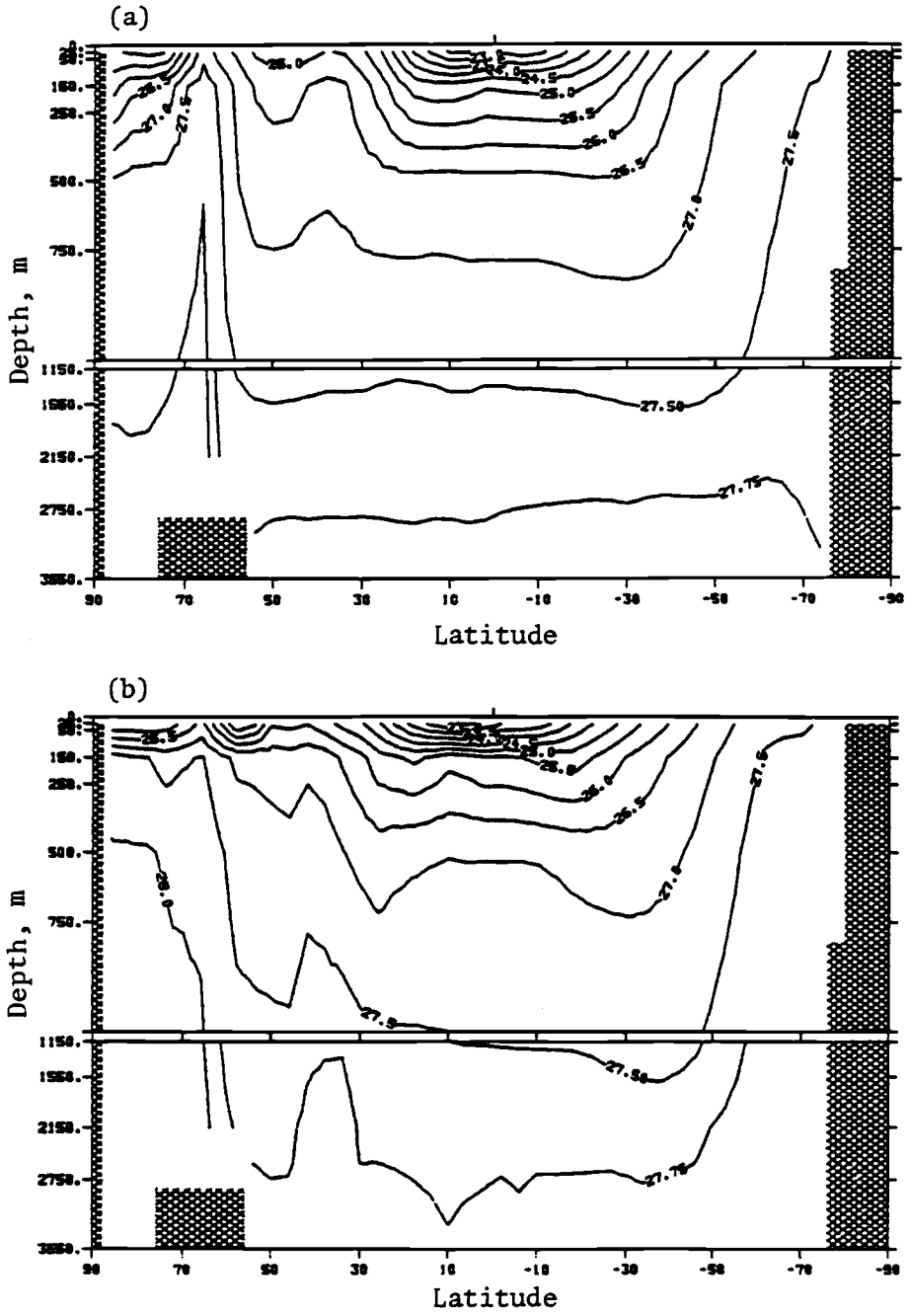

Fig. 3.7. Latitude-depth distribution of the annual zonal mean oceanic potential density σ_θ for: (a) year 12 of the CGCM control run, and (b) the observations of Levitus (1982).

ridge near 35°N in the deep ocean (see the 27.50 and 27.75 isopycnals) is not evident in the simulated field and the observed σ_θ value at the surface near the north polar region is underestimated in the simulation.

The differences between the simulated and the observed potential densities are shown in Fig. 3.8 together with the difference between the potential density simulated during year 11 of the uncoupled OGCM and the observations. This figure shows that the coupled model underestimates the potential density almost everywhere except in the upper layer near 30°N and 60°N. The largest underestimated values occur in the second layer at the North Pole and near 10°N, the latter in association with the overestimation of the potential temperature in this region (Fig. 3.2a). Similarly, the overestimated potential density values near 30°N and 60°N are associated with the underestimation of the potential temperature by the model in these regions.

A comparison of the upper and lower panels of Fig. 3.8 shows that most of the σ_θ errors were already introduced by the uncoupled OGCM. However, unlike the coupled model, the uncoupled OGCM overestimated σ_θ everywhere in the first layer in association with the temperature errors of the uncoupled OGCM (Fig. 3.2b). The underestimation of σ_θ in the upper layer near 30°N by the OGCM became an overestimation after the coupling as a result of the failure of the CGCM to simulate the observed temperature in that region.

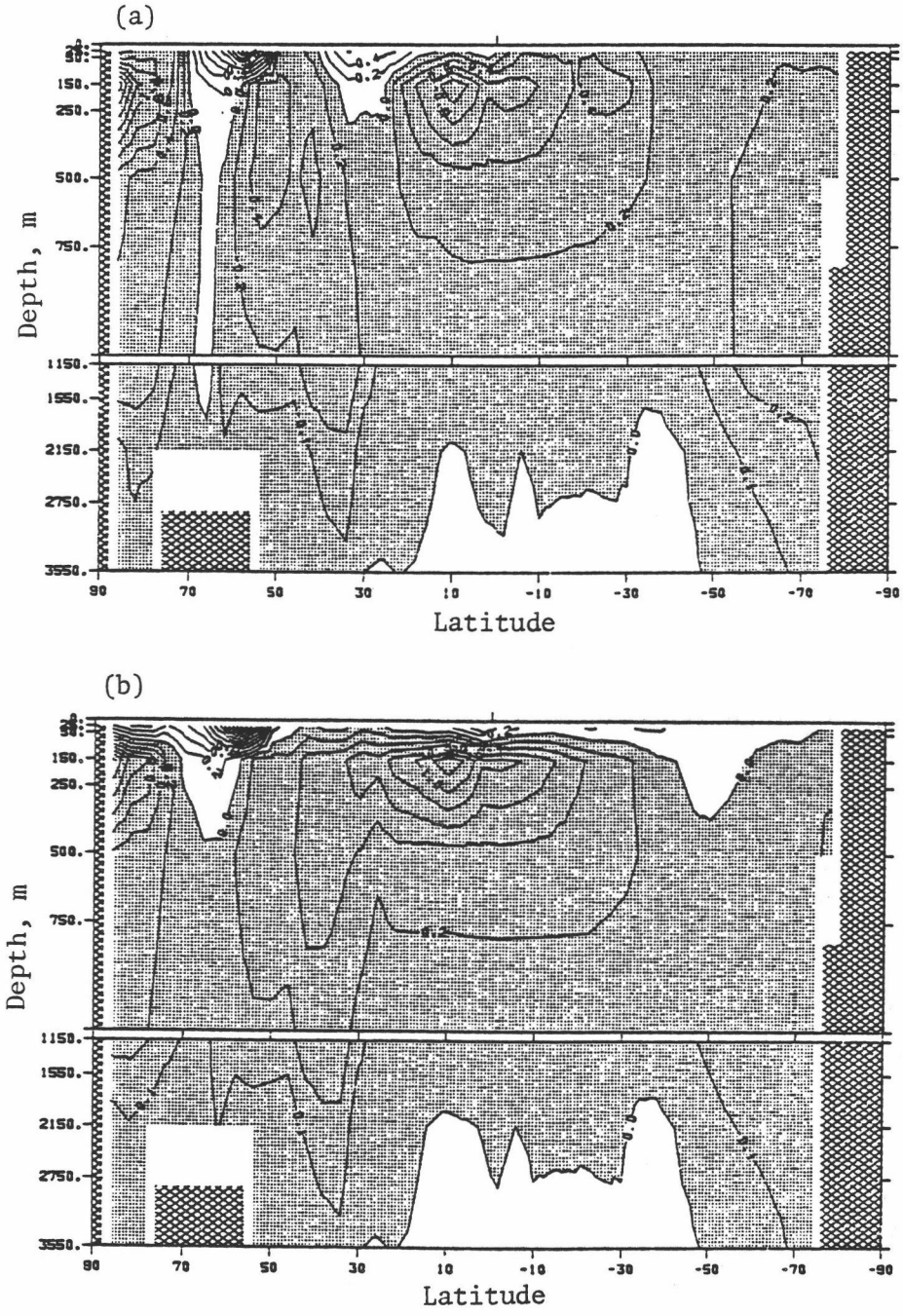

Fig. 3.8. Latitude-depth distribution of the difference in the annual zonal mean oceanic potential density σ_θ: (a) year 12 of the control run minus the observations, and (b) year 11 of the OGCM run minus the observations. Negative values are shaded.

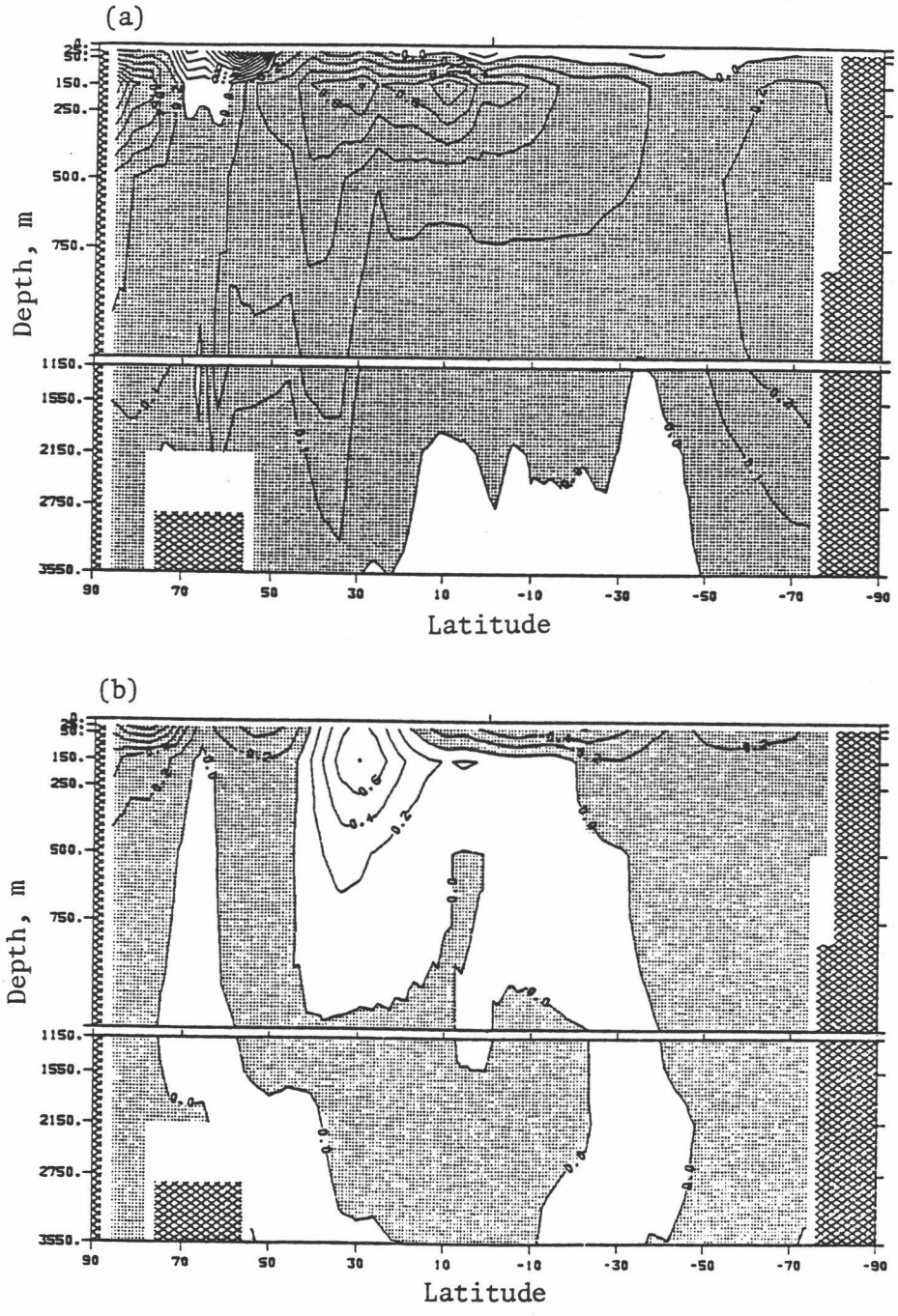

Fig. 3.9. Latitude-depth distribution of the differrence in the annual zonal mean oceanic potential density σ_θ for: (a) year 25 of the OGCM run without seasonal cycles minus the observations, and (b) year 12 of the CGCM control run minus year 11 of the OGCM run. Negative values are shaded.

Further evidence of the errors introduced by the uncoupled OGCM is provided by the upper panel of Fig. 3.9 which shows the difference between the potential density simulated by the uncoupled OGCM without seasonal cycles at the end of year 25 and the observations. A comparison of this panel with the lower panel of Fig. 3.8 shows that the potential density error occurred during the OGCM simulation without seasonal cycles with little additional error being introduced by the OGCM run with the annual cycle.

The potential density differences between year 12 of the coupled control run and year 11 of the uncoupled OGCM run are given in the lower panel of Fig. 3.9. This figure and Fig. 3.3b clearly show that the potential density errors resulting from the coupling are negatively correlated with the potential temperature errors due to the coupling, that is, denser water is associated with cooling and less dense water is associated with warming.

3.2. Ocean Currents and Heat Transports

In the preceding section we presented the annual zonal mean oceanic quantities simulated by the CGCM for which there are corresponding quantitative observations, namely, potential temperature, salinity and potential density. In this section we present selected CGCM simulation results for which there are only corresponding qualitative observations, namely, the ocean currents and heat transports.

3.2.1. Ocean currents

The observations and theories of the ocean circulation have been reviewed by Reid (1981), Warren (1981) and Veronis (1981). Much of this information is qualitative and has been inferred from the location of different water mass types as characterized by their temperature, salinity, dissolved oxygen and chemical properties.

Ocean currents are the result of the wind-driven and thermohaline ocean circulations. The former prevail in the upper ocean, above about 1000 m, and the latter prevail in the deep ocean, below about 1000 m. Although there is direct quantitative information about the circulation in the upper ocean, the information about the circulation of the deep ocean has been inferred largely from the distribution of ocean water mass types and is therefore qualitative.

Due to the constraint of topography, most information about the ocean circulation is shown for the ocean basins (almost exclusively for the Atlantic Ocean), not for the zonal mean. Figure 3.10a shows a schematic diagram of the circulation in the Atlantic Ocean which has been inferred from the different water mass types there. Strong downwellings are found in the subtropical upper ocean and throughout most of the ocean at 70° latitude in both hemispheres. Upwellings occur at the equator (not shown) and 60°S and 40°N in the upper ocean, and at 60°S through much of the ocean. Below the thermocline the water flows from south to north above 1500 m, and from north to south below 1500 m.

Figure 3.10b shows the zonal mean ocean circulation for year 12 of the CGCM control run. In this figure the vertical component of the model's velocity has been multipled by 2000 relative to the meridional component because otherwise the vectors would all be horizontal in this representation. Then, both the meridional and the multiplied vertical velocity components were divided by the magnitude of the resultant velocity. Thus, only an indication of the relative direction of the velocity is shown. Furthermore, direct comparison between the two panels of Fig. 3.10 is difficult because the model is not in equilibrium and the model results are not for the Atlantic Ocean only. Nevertheless, since the observed and theoretical ocean circulations show considerable similarities in both the upper and deeper parts of the major oceans (Stommel, 1958; Gordon, 1975a,b; Wunch, 1984), it is of interest to compare the simulated and observed ocean circulation, at least qualitatively. The lower panel of Fig. 3.10 shows downward motions around 60°N and 70°S which agree with the observations in the Atlantic Ocean. The simulated northward motion at 500 m and the southward motion at 2150 m also agree with the observations in the Atlantic Ocean.

The latitude-depth distributions of the individual vertical and meridional components of the annual zonal mean velocity simulated by the CGCM control run for year 12 are shown in the upper and lower panels of Fig. 3.11, respectively. The upper panel shows upwelling in the equatorial region, with a maximum value of 10 cm/day, and a compensating downwelling in the subtropical latitudes

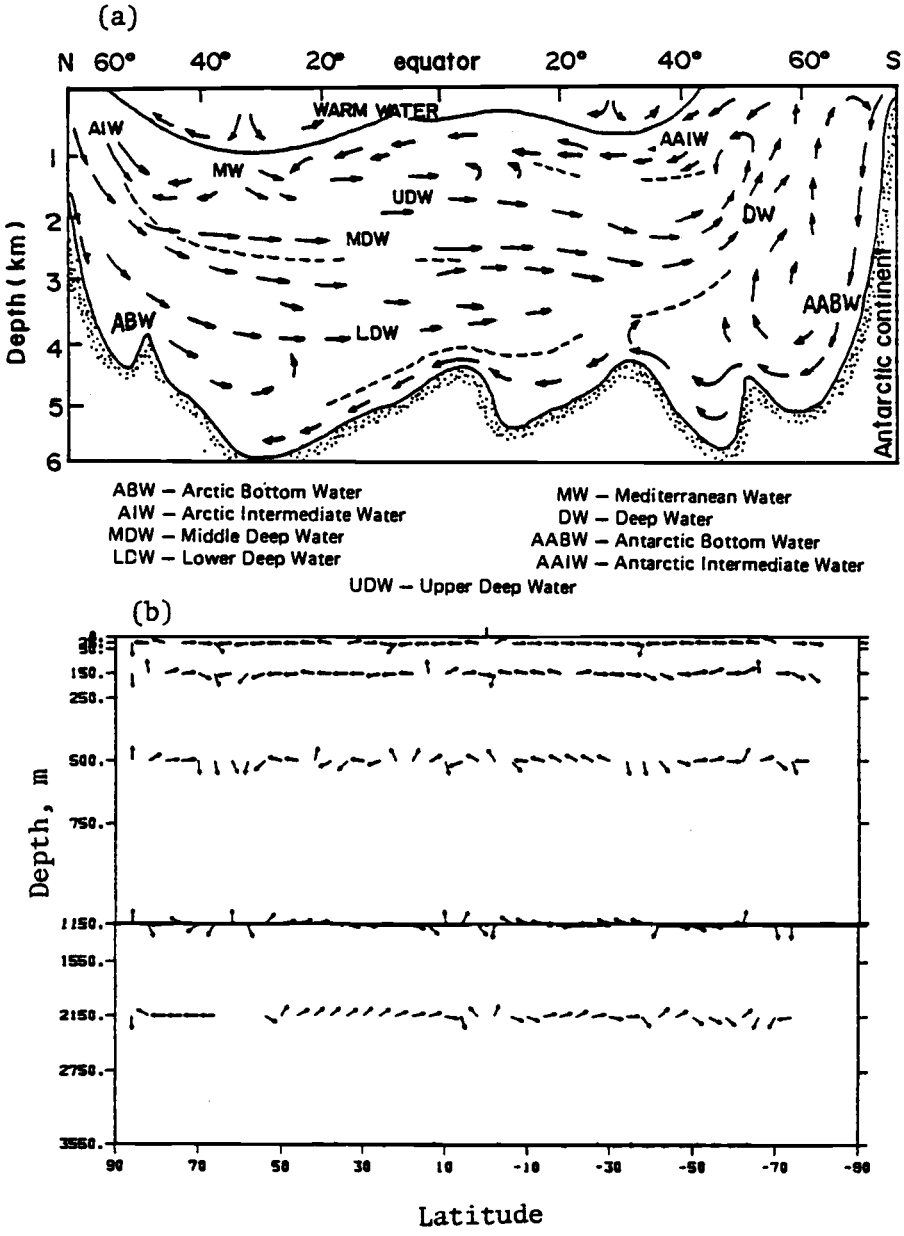

Fig. 3.10. (a) Schematic latitude-depth diagram of the water masses and circulation in the Atlantic Ocean from Stowe (1979), and (b) the annual zonal mean velocity for year 12 of the OSU CGCM control run. In (b) the vertical component of the velocity has been multiplied by 2000 relative to the meridional component, and then both the meridional component and the multiplied vertical component were divided by the magnitude of the resultant velocity.

of each hemisphere. The equatorial upwelling is in good agreement with the observation discussed by Gordon (1975a). This observed equatorial upwelling in the upper ocean may be produced by the equatorial wind system which is responsible for the wind-driven oceanic circulation (Gordon, 1975b). The pattern of the simulated vertical motion is directly related, through the conservation of mass, to the divergence and convergence of the meridional motion in the upper ocean, the latter shown in Fig. 3.11b. Regions of strong sinking motion, with a maximum value of 30 cm/day, are found between 60°N and 70°N, and centered at 70°S. These downwelling regions correspond to the formation of cold North Atlantic and Antarctic water (Stommel, 1958; Stommel and Arons, 1960a,b; Gordon, 1975a,b; Wunch, 1983). The previously noted sinking motion in the subtropical upper ocean in both hemispheres extends downward into the midlatitude intermediate water. These regions of sinking motion are colocated with the regions of high salinity (see Fig. 3.4). As discussed by Levitus (1982), for the observed circulation the denser, more saline water in the subtropical regions sinks along isopycnals until it is completely mixed with the neighboring water. Near 80°N, strong upwelling is simulated above 750m, with strong downwelling below. The latter might be evidence of the formation of the Arctic Bottom Water.

From the distribution of annual zonal mean meridional current shown in Fig. 3.11b it can be seen that the largest poleward currents occur at the surface. The large poleward current centered near 50°N likely corresponds to the intense Kuroshio and Gulf

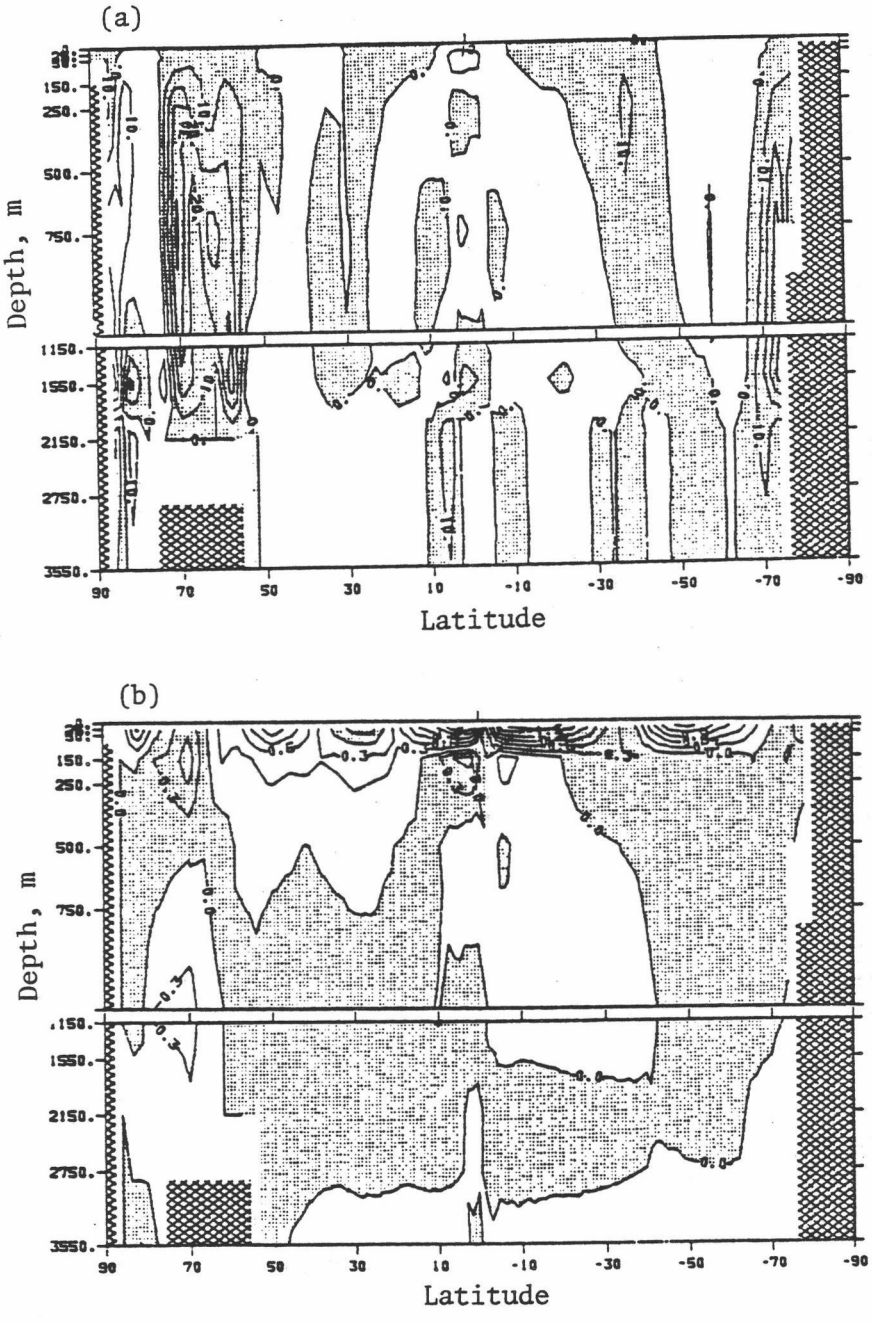

Fig. 3.11. Latitude-depth distribution of the annual zonal mean oceanic velocity for year 12 of the CGCM control run. (a) vertical velocity component (cm/day) with upward motion positive and downward motion negative, and (b) meridional velocity component (cm/sec) with northward motion positive and southward motion negative. Negative values are shaded.

Stream boundary currents. Equatorward motions are found in the subtropical and midlatitude areas of each hemisphere in the third and fourth layers of the ocean model. It should be noted that the meridional currents tend to have opposite directions in the upper and intermediate ocean, and that the largest values of the meridional currents are restricted to the upper ocean layers. The latter likely represent the wind-driven circulation.

It is interesting to note that there are three meridional circulation cells in the Southern Hemisphere in accord with the three-cell structure of the observed atmospheric circulation. However, in the Northern Hemisphere four simulated oceanic circulation cells exist, while only three are generally found in the atmosphere. The vertical motion field of the ocean in the Northern Hemisphere is somewhat more complex than that of the Southern Hemisphere, perhaps because of the more complex distribution of land and ocean.

3.2.2. Ocean heat transports

In order to discuss the ocean heat transport it is useful to consider the First Law of Thermodynamics in spherical coordinates,

$$\frac{\partial T}{\partial t} = -\frac{1}{a\cos\phi}\frac{\partial}{\partial\lambda}(uT) - \frac{1}{a\cos\phi}\frac{\partial}{\partial\phi}(\cos\phi\ vT) - \frac{\partial}{\partial z}(wT)$$

$$+ \frac{1}{a\cos\phi}\frac{\partial}{\partial\lambda}\left(\frac{A_H}{a\cos\phi}\frac{\partial T}{\partial\lambda}\right) + \frac{1}{a\cos\phi}\frac{\partial}{\partial\phi}\left(A_H\frac{\cos\phi}{a}\frac{\partial T}{\partial\phi}\right)$$

$$+ \frac{\partial}{\partial z}\left(\kappa\frac{\partial T}{\partial z}\right) + Q_{conv}\ , \qquad (3.7)$$

where u, v and w are the eastward (zonal), northward (meridional) and vertical velocity components, respectively, λ is longitude, ϕ is latitude and z is the vertical depth measured from the sea surface with positive upward (in agreement with the sign convention of the ocean model), t is time, A_H and κ are the horizontal and vertical eddy diffusivities of heat, respectively, and Q_{conv} is the contribution by convective overturning with

$$Q_{conv} \begin{cases} = 0 \\ \neq 0 \end{cases} \quad \text{for} \quad \frac{\partial \rho}{\partial z} \begin{cases} > 0 \\ < 0 \end{cases} . \tag{3.8}$$

The case $Q_{conv} \neq 0$ represents the instantaneous convective overturning in the OGCM that restores a neutral density stratification whenever a vertically unstable stratification develops.

In the OGCM, u and v are prognostic quantities governed by the horizontal momentum equation, w is a diagnostic quantity determined from the continuity equation, and A_H and κ are prescribed parameters with values of 2×10^7 cm^2/sec and 1 cm^2/sec, respectively.

Taking the zonal average of Eq. (3.7) and using the lateral boundary conditions that $u = 0$ and $\partial T/\partial \lambda = 0$ at the north-south coasts of the model then gives

$$\rho c \frac{\partial \overline{T}^z}{\partial t} = \overline{TADVM}^z + \overline{TADVV}^z + \overline{TDIFM}^z + \overline{TDIFV}^z + \overline{TCONV}^z \quad , \tag{3.9}$$

where "$\overline{\quad}^z$" denotes the zonal average, ρ is density which is considered as constant in the heat transport analysis, c is the heat capacity of the ocean water and

$$\overline{\text{TADVM}}^{z} = -\frac{1}{a\cos\phi}\frac{\partial}{\partial\phi}\left(\cos\phi\ \overline{\rho c v T}^{z}\right)$$

$$= -\frac{1}{a\cos\phi}\frac{\partial}{\partial\phi}\left(\cos\phi\ \overline{\text{FADVM}}^{z}\right) \qquad (3.10)$$

is the contribution to the zonal mean temperature change by the meridional advective heat flux $\overline{\text{FADVM}}^{z}$,

$$\overline{\text{TADVV}}^{z} = -\frac{\partial}{\partial z}\overline{\rho c w T}^{z}$$

$$= -\frac{\partial}{\partial z}\overline{\text{FADVV}}^{z} \qquad (3.11)$$

is the contribution to the zonal mean temperature change by the vertical advective heat flux $\overline{\text{FADVV}}^{z}$,

$$\overline{\text{TDIFM}}^{z} = \frac{1}{a\cos\phi}\frac{\partial}{\partial\phi}\left(\cos\phi\ \overline{\rho c \frac{A_H}{a}\frac{\partial T}{\partial\phi}}^{z}\right)$$

$$= \frac{1}{a\cos\phi}\frac{\partial}{\partial\phi}\left(\cos\phi\ \overline{\text{FDIFM}}^{z}\right) \qquad (3.12)$$

is the contribution to the zonal mean temperature change by the meridional diffusive heat flux $\overline{\text{FDIFM}}^{z}$,

$$\overline{\text{TDIFV}}^{z} = \frac{\partial}{\partial z}\left(\overline{\rho c \kappa \frac{\partial T}{\partial z}}^{z}\right)$$

$$= \frac{\partial}{\partial z}\overline{\text{FDIFV}}^{z} \qquad (3.13)$$

is the contribution to the zonal mean temperature change by the vertical diffusive heat flux $\overline{\text{FDIVF}}^z$, and $\overline{\text{TCONV}}^z$ is the contribution to the zonal mean temperature change by the convective heat flux $\overline{\text{FCONV}}^z$.

Vertical integration of Eq. (3.9) from the ocean surface (z = 0) to the bottom (z = -D) and use of the boundary conditions

$$\overline{\text{FADVV}}^z = \overline{\text{FCONV}}^z = 0 \tag{3.14a}$$

and

$$\overline{\text{FDIFV}}^z = \overline{\text{FTS}}^z \quad \text{at } z = 0 \tag{3.14b}$$

where $\overline{\text{FTS}}^z$ is the zonal mean ocean surface heat flux, and

$$\overline{\text{FADVV}}^z = \overline{\text{FDIFV}}^z = \overline{\text{FCONV}}^z = 0 \quad \text{at } z = -D \ , \tag{3.15}$$

gives

$$\rho c \frac{\partial \{\overline{T}\}^z}{\partial t} = \left\{ \overline{\text{TADVM}}^z + \overline{\text{TDIFM}}^z \right\} + \overline{\text{FTS}}^z \tag{3.16}$$

where

$$\{Y\} = \int_{-D}^{0} Y \, dz \tag{3.17}$$

represents the vertical integral of Y throughout the depth of the ocean. The first two terms on the right-hand side of Eq. (3.16) represent the vertically-integrated zonal mean temperature change

due to the vertically-integrated meridional heat flux, and the second term is the contribution by the ocean surface heat flux.

In the following we first discuss the terms of Eq. (3.16) for the simulated vertically integrated heat budget and compare them with the observations of Esbensen and Kushnir (1981). Then the results for each component of Eq. (3.9) for the simulated vertically distributed heat budget will be presented. This will be useful as background for understanding the CO_2-induced changes in the heat transport processes discussed in Chapter 4. In order to be consistent with the discussion in Chapter 4 we show the heat flux in terms of annual average and the temperature in terms of annual integrals.

a. Vertically-integrated zonal mean heat budget

The upper panel of Fig. 3.12 shows the simulated annually-averaged zonal mean ocean surface heat flux for year 12 of the control run, together with the corresponding observations. In general, both the observation and the simulation indicate that the ocean gains heat from the atmosphere in the tropics and loses heat to the atmosphere in high latitudes. It can be seen that the simulated heat flux agrees quite well with the observed flux in the tropics, but disagrees in high latitudes where the model underestimates the heat loss from the ocean to the atmosphere in the Northern Hemisphere and overestimates the heat loss from the ocean to the atmosphere in the Southern Hemisphere. This disagreement is

in part a consequence of the model's not having achieved equilibrium.

The middle panel shows the change in the annually-averaged vertically-integrated heat content of the ocean for year 12 of the CGCM control. For the observations it is assumed that the annually-averaged change is zero at each latitude. However, the simulation shows that nonzero changes occurred in the tropics and at 60°N and 70°S. These changes again clearly indicate the model's disequilibrium.

The lower panel of Fig. 3.12 shows the change in the annually-averaged, vertically-integrated meridional heat transport for year 12 of the CGCM control, $\{\overline{\overline{TADVM}}^{z} + \overline{\overline{TDIFM}}^{z}\}$, together with that inferred for the observations from Eq. 3.16 and Fig. 3.12a,b. Both the observations and the simulation show that the ocean gains heat at high latitudes and loses heat in the tropics due to the meridional heat transport. It is interesting that the heat gain by the meridional transport poleward of 50°S is much larger in the simulation than that inferred from the observation. This suggests that the warming around Antarctic in the CGCM control noted by Gates et al. (1984) and Han et al. (1985) is not entirely due to errors in the ocean surface flux caused by the atmospheric model, as described by Han et al. (1985), but is also due to an excessive meridional transport contribution by the ocean model.

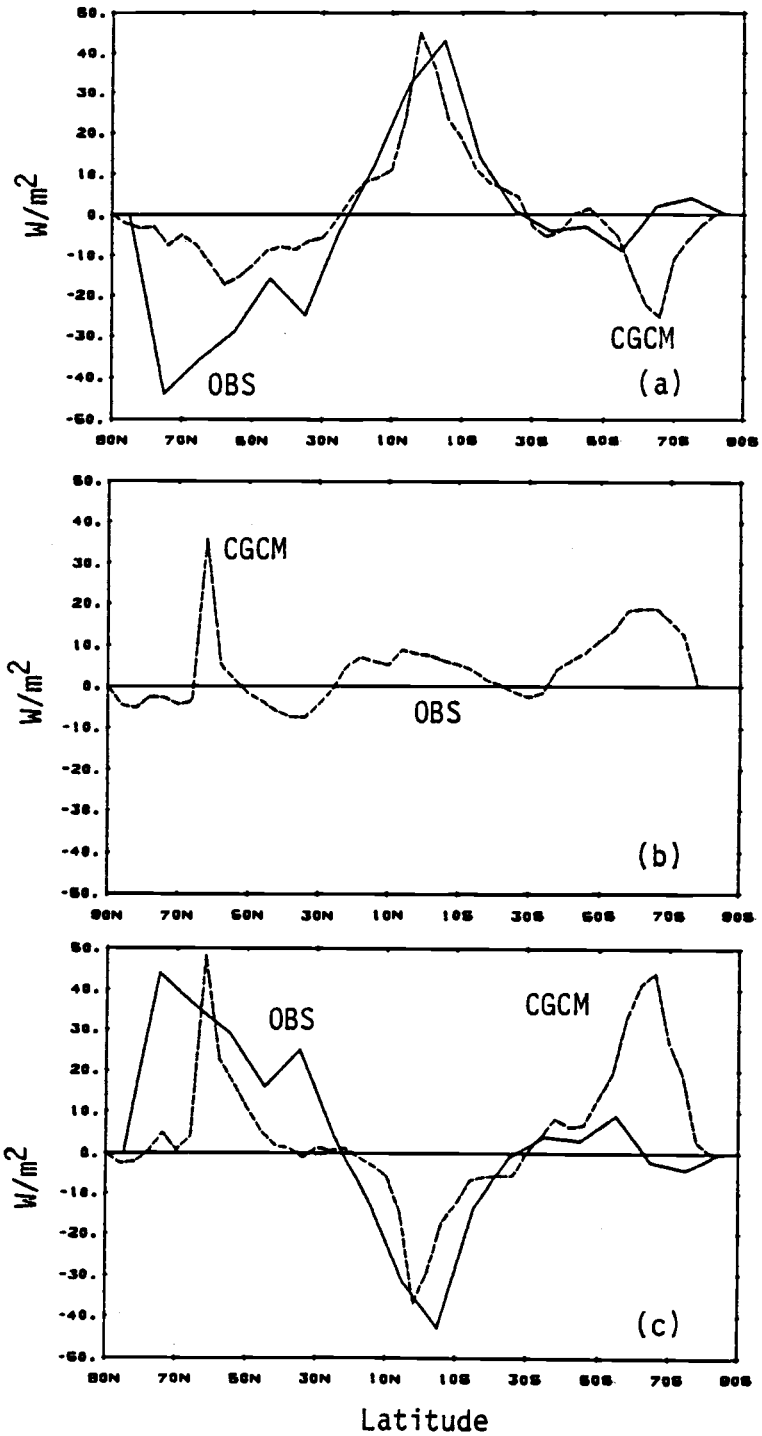

Fig. 3.12. Latitude distributions of the terms in the annually-averaged vertically-integrated zonal mean heat budget Eq. (3.16) averaged for year 12 of the CGCM control run (dashed line) and from the observations of Esbensen and Kushnir (1981, solid line). (a) ocean surface heat flux, (b) change in heat content, and (c) meridional heat transport.

b. Vertical distribution of the zonal mean heat budget

Figure 3.13 shows the annually-integrated zonal mean temperature changes by the vertical and meridional advection, $\overline{TADVV}^z$ and $\overline{TADVM}^z$, for year 12 of the CGCM control run. The largest changes are found in the upper layer of the OGCM in the tropics. The temperature changes by meridional advection and by vertical advection largely compensate each other almost everywhere. The zonal mean temperature change by the vertical and meridional diffusion, $\overline{TDIFV}^z$ and $\overline{TDIFM}^z$, and by the vertical convection, $\overline{TCONV}^z$, are shown in Fig. 3.14. It can be seen that the maximum temperature changes by vertical diffusion occurred in the upper layer of the OGCM with cooling in the subtropical and high latitudes, the warming in the tropics. The temperature changes by meridional diffusion are about one order of magnitude smaller than the changes by the other processes with the largest change occurring at 70°N. Figure 3.14c shows that strong vertical convection occurs between the first and second layers of the OGCM with heating above and cooling below. The convection occurs in the middle and higher latitudes of both hemispheres, and results in a maximum warming of about 5°C in the upper layer.

Figure 3.15 shows the annually-averaged zonal mean heat fluxes by advection, $\overline{FADVV}^z$ and $\overline{FADVM}^z$, for year 12 of the CGCM control run. These fluxes are very similar to the current patterns shown in Fig. 3.11. Strong downward heat transports are found in the subtropical regions in both hemispheres. Another strong downward transport is located between 60°N and 70°N. The meridional

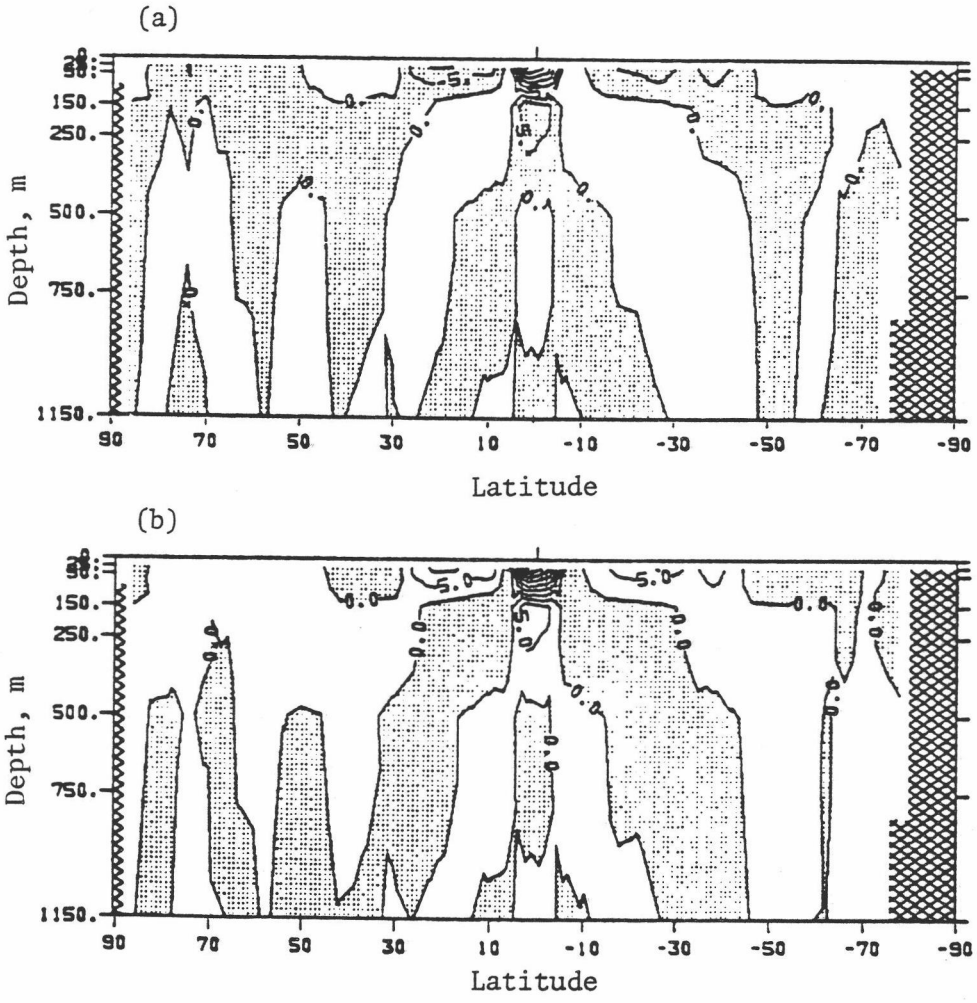

Fig. 3.13. Latitude-depth distribution of the advective terms in Eq. (3.9) annually-integrated for year 12 of the CGCM control run. (a) temperature change due to vertical advection, $\overline{TADVV}^z$, and (b) temperature change due to meridional advection, $\overline{TADVM}^z$. Units are °C/year and negative values are shaded.

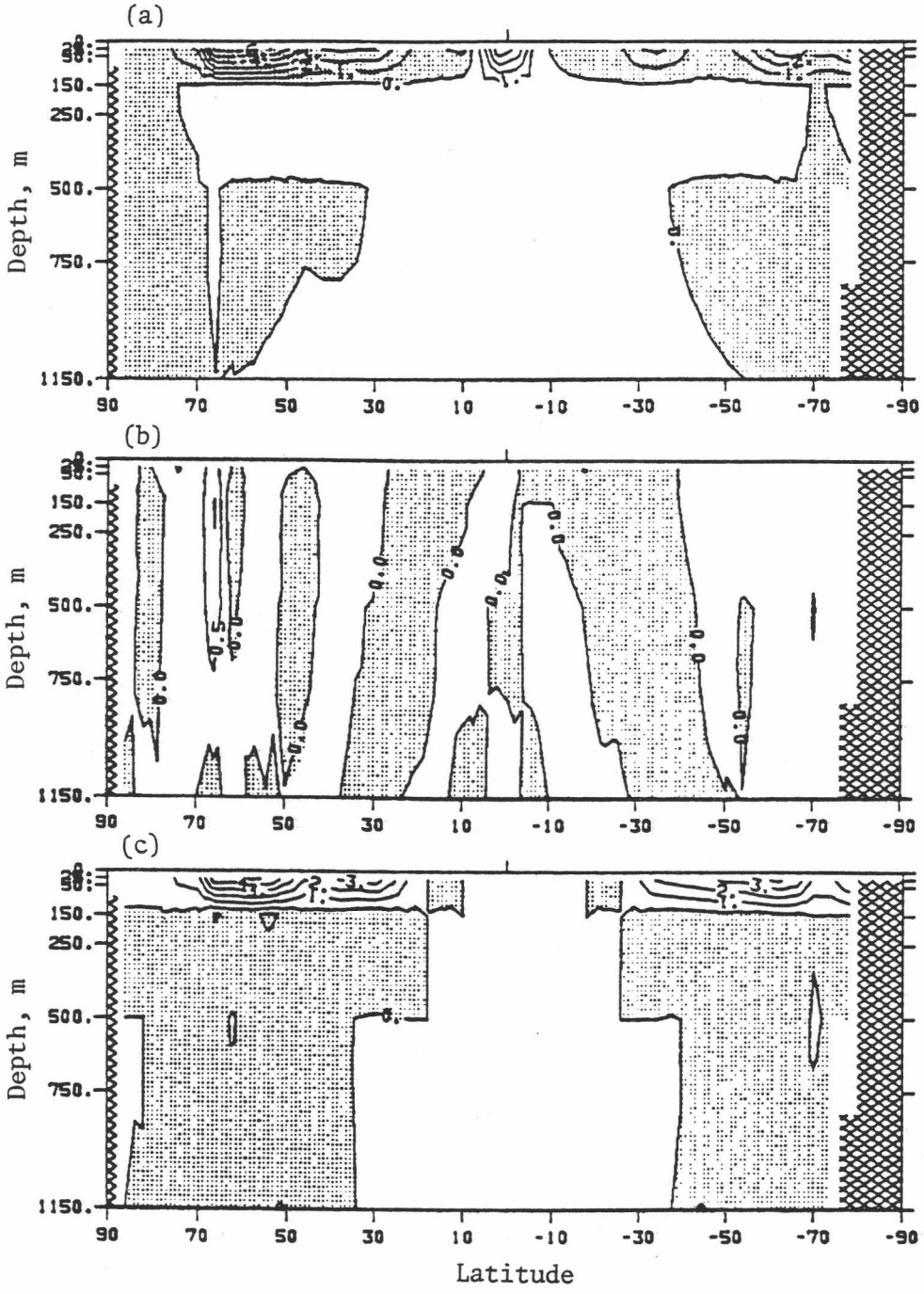

Fig. 3.14. Latitude-depth distribution of the diffusive and convective terms in Eq. (3.9) annually-integrated for year 12 of the CGCM control run. (a) temperature changes due to vertical diffusion, $\overline{\text{TDIFV}}^z$, (b) temperature changes due to meridional diffusion, $\overline{\text{TDIFM}}^z$, and (c) temperature changes due to vertical convection, $\overline{\text{TCONV}}^z$. Units are °C/year and negative values are shaded.

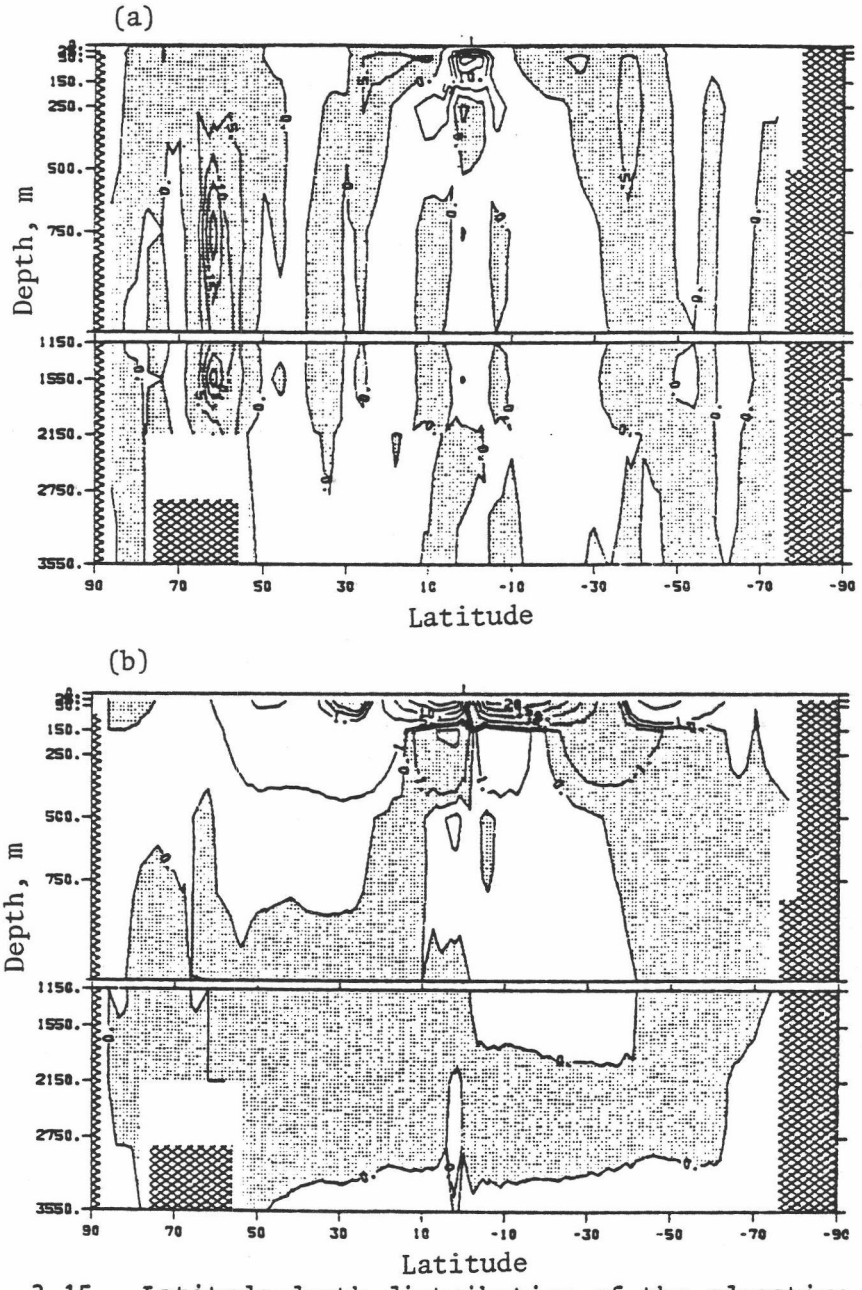

Fig. 3.15. Latitude-depth distribution of the advective flux terms in the annually-averaged zonal mean heat budget for year 12 of the CGCM control run. (a) vertical heat flux, $\overline{FADVV}^z$ in units of 10 W/m^2, with upward values positive and downward values negative, and (b) meridional heat flux, $\overline{FADVM}^z$ in units of 10^5 W/m^2, with northward values positive and southward values negative. Negative values are shaded.

heat transport due to advection is large in the upper ocean with values that are about four orders of magnitude greater than the vertical heat transport due to advection.

The annually-averaged zonal mean heat fluxes by diffusion, $\overline{\text{FDIFV}}^{z}$ and $\overline{\text{FDIFM}}^{z}$, for year 12 of the OGCM control run are presented in Fig. 3.16. This figure shows that heat is generally transported downward by diffusion to the deep layers. This occurs because the temperature decreases downwards everywhere except near the surface in the high latitudes during winter (Fig. 3.1). The large values shown in the figure reflect the large vertical temperature gradient located in the upper layers of the OGCM. The small positive values shown in Fig. 3.16a indicate that the temperature may increase with depth during certain seasons in the polar regions. The meridional heat flux by diffusion shows that poleward heat transport occurs in the equatorial regions in both hemispheres and equatorward heat transport occurs everywhere else in the upper ocean and intermediate water. These features correspond to the horizontal temperature gradients shown in Fig. 3.1. However, the meridional heat flux by diffusion is about one order of magnitude smaller than the meridional heat flux by advection.

The vertical heat flux by convection, $\overline{\text{FCONV}}^{z}$, presented in Fig. 3.17 shows that convection always transports heat toward the ocean surface. (The negative values at low latitudes shown in Fig. 3.17 are artifacts of the graphics presentation.) The convective heat transport is largest in the upper and intermediate ocean in high latitudes.

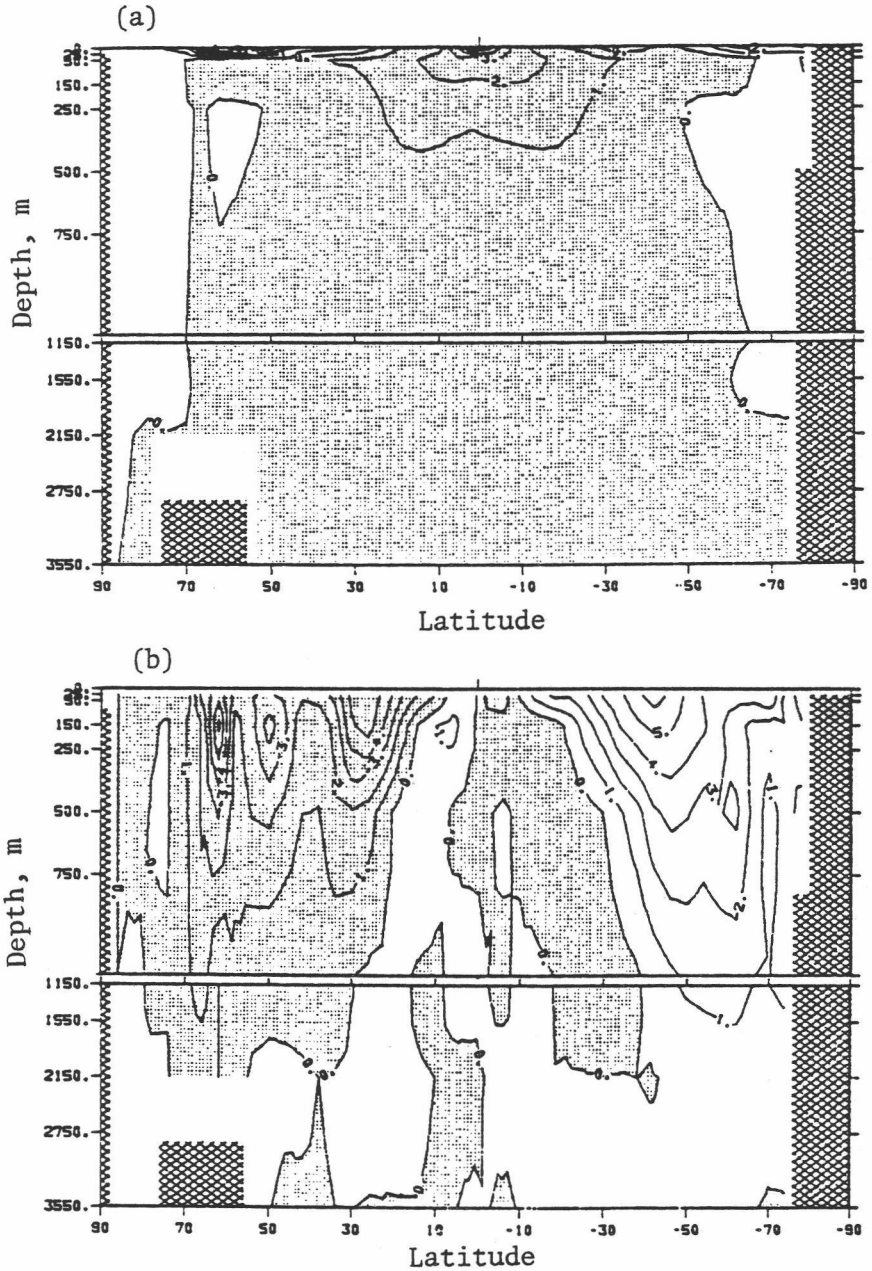

Fig. 3.16. Latitude-depth distribution of the diffusive flux terms in the annually-averaged zonal mean heat budget for year 12 of the CGCM control run. (a) vertical heat transport, $\overline{FDIFV}^z$ in units of 10 W/m^2, with upward values positive and downward values negative, and (b) meridional heat transport, $\overline{FDIFM}^z$ in units of 10^4 W/m^2, with northward values positive and southward values negative. Negative values are shaded.

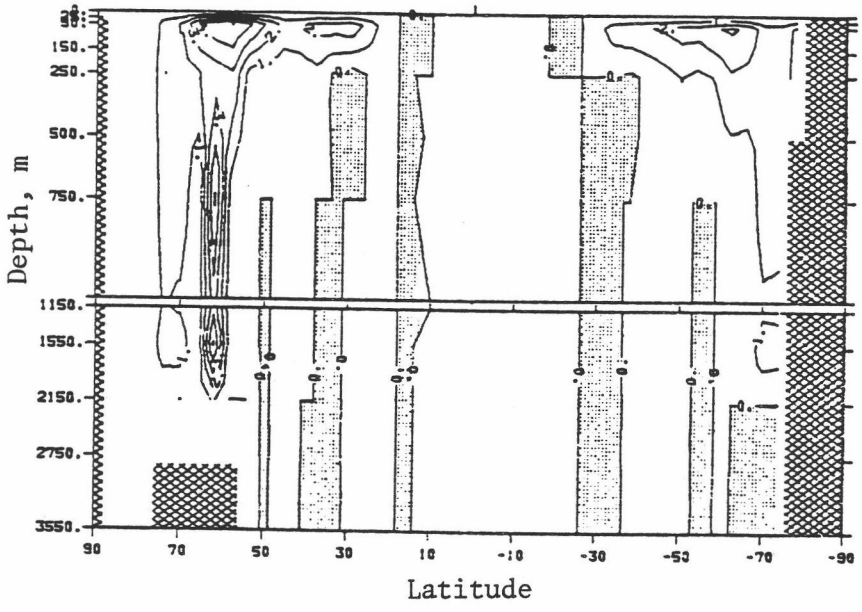

Fig. 3.17. Latitude-depth distribution of the convective flux, $\overline{FCONV}^z$ in units of 10 W/m^2, in the annually-averaged zonal mean heat budget for year 12 of the CGCM control run. Upwward values are positive and downward values negative. Negative values are shaded.

4. ANALYSIS OF CO_2-INDUCED OCEAN TEMPERATURE CHANGES

In the previous chapter selected results from the coupled model control ($1xCO_2$) simulation were presented. These results showed that although the coupled model simulates many of the features of the observed fields of potential temperature, salinity, potential density, ocean currents and heat transports, it produces systematic errors as a result of both the individual atmospheric and oceanic GCMs. In this chapter, we turn our attention to the issue of CO_2-induced climate change and consider further the results from the coupled model $2xCO_2$ simulation.

In considering the global mean $2xCO_2-1xCO_2$ temperature difference for the atmosphere and ocean, we have seen in Fig. 2.8 that there was an initially rapid and vertically uniform warming of the atmosphere followed by a progressively slowing atmospheric warming induced by the CO_2 doubling. Figure 2.8 also showed an initially rapid warming of the sea surface followed by a progressively slowing warming. It was noted in Chapter 2 that the decrease with time in the warming rate of the atmosphere and sea surface was the result of a downward transport of heat into the interior of the ocean. However, by what pathways and through which physical processes does the simulated ocean circulation produce this penetration of the CO_2-induced warming into the ocean? The goal of this chapter is to answer this question.

In the following we first present the methods which are used to analyze the oceanic heat transport processes. Then we analyze

the global mean warming of the ocean and determine which heat transport processes are dominant. Finally, we perform a similar analysis of the zonal mean ocean temperature changes induced by the instantaneous CO_2 doubling.

4.1. Method of Analysis

The zonally averaged First Law of Thermodynamics for the ocean is given by Eq. (3.9). For the $1xCO_2$ and $2xCO_2$ simulations Eq. (3.9) gives

$$\rho c \frac{\partial T(1xCO_2)}{\partial t} = \overline{TADVM}^z(1xCO_2) + \overline{TADVV}^z(1xCO_2) + \overline{TDIFM}^z(1xCO_2) + \overline{TDIFV}^z(1xCO_2) + \overline{TCONV}^z(1xCO_2) \quad (4.1)$$

and

$$\rho c \frac{\partial T(2xCO_2)}{\partial t} = \overline{TADVM}^z(2xCO_2) + \overline{TADVV}^z(2xCO_2) + \overline{TDIFM}^z(2xCO_2) + \overline{TDIFV}^z(2xCO_2) + \overline{TCONV}^z(2xCO_2) , \quad (4.2)$$

where $\overline{TADVM}^z$ and $\overline{TADVV}^z$ are the zonal mean temporal changes in temperature (times density ρ and heat capacity c) due to meridional and vertical advection, respectively, $\overline{TDIFM}^z$ and $\overline{TDIFV}^z$ are the corresponding changes due to diffusion, and $\overline{TCONV}^z$ is the change due to convection. Subtracting Eq. (4.1)

from Eq. (4.2) gives

$$\rho c \overline{\frac{\partial \Delta T}{\partial t}}^{z} = \Delta(\overline{TADVM})^{z} + \Delta(\overline{TADVV})^{z} + \Delta(\overline{TDIFM})^{z} + \Delta(\overline{TDIFV})^{z}$$

$$+ \Delta(\overline{TCONV})^{z} \quad , \tag{4.3}$$

where the "Δ" operator indicates the $2xCO_2$ value minus the $1xCO_2$ value,

$$\Delta(\overline{TADVM})^{z} = \frac{1}{a\cos\phi} \frac{\partial}{\partial \phi} \left[\cos\phi \; \Delta(\overline{\rho cvT})^{z}\right]$$

$$= \frac{1}{a\cos\phi} \frac{\partial}{\partial \phi} \left[\cos\phi \; \Delta\overline{FADVM}^{z}\right] \tag{4.4}$$

is the contribution to the temporal $\overline{\Delta T}^{z}$ change by the meridional advective heat flux $\Delta\overline{FADVM}^{z}$,

$$\Delta(\overline{TADVV})^{z} = \frac{\partial}{\partial z} \Delta(\overline{\rho cwT})^{z}$$

$$= \frac{\partial}{\partial z} \Delta\overline{FADVV}^{z} \tag{4.5}$$

is the contribution to the temporal $\overline{\Delta T}^{z}$ change by the vertical advective heat flux $\Delta\overline{FADVV}^{z}$,

$$\Delta(\overline{TDIFM})^{z} = \frac{1}{a\cos\phi} \frac{\partial}{\partial \phi} \left[\cos\phi \; A_H \; \rho c \frac{\overline{\partial \Delta T}^{z}}{\partial \phi}\right]$$

$$= \frac{1}{a\cos\phi} \frac{\partial}{\partial \phi} \left[\cos\phi \; \Delta\overline{FDIFM}^{z}\right] \tag{4.6}$$

is the contribution to the temporal $\overline{\Delta T}^z$ change by the meridional diffusive heat flux $\overline{FDIFV}^z$,

$$\Delta(\overline{TDIFV})^z = \frac{\partial}{\partial z}\left[\rho c \kappa \frac{\partial \overline{\Delta T}^z}{\partial z}\right]$$

$$= \frac{\partial}{\partial z} \Delta\overline{FDIFV}^z \qquad (4.7)$$

is the contribution to the temporal $\overline{\Delta T}^z$ change by the vertical diffusive heat flux $\Delta\overline{FDIFV}^z$, and $\Delta(\overline{TCONV})^z$ is the contribution to the temporal $\overline{\Delta T}^z$ change by the vertical convective heat flux $\Delta\overline{FCONV}^z$.

These zonal mean components will be presented in section 3 of this chapter together with the corresponding ΔT changes.

Taking the meridional average of Eq. (4.3) from the coast of Antarctica to the North Pole and using the boundary conditions that $\Delta(\overline{FADVM})^z$ and $\Delta(\overline{FDIFM})^z$ vanish at the coast and the pole gives

$$\rho c \frac{\overline{\partial \Delta T}^G}{\partial t} = \Delta(\overline{TADVV})^G + \Delta(\overline{TDIFV})^G + \Delta(\overline{TCONV})^G , \qquad (4.8)$$

where the overbar "$\overline{\quad}^G$" represents the global mean and

$$\Delta(\overline{TADVV})^G = \frac{\partial}{\partial z} \Delta(\overline{\rho c w T})^G$$

$$= \frac{\partial}{\partial z} \Delta\overline{FADVV}^G \qquad (4.9)$$

is the contribution to the temporal $\overline{\Delta T}^G$ change by the vertical advective heat flux $\Delta\overline{FADVV}^G$,

$$\Delta(\overline{\text{TDIFV}})^G = \frac{\partial}{\partial z}\left(\rho c \kappa \frac{\overline{\partial \Delta T}^G}{\partial z}\right)$$

$$= \frac{\partial}{\partial z}\,\Delta\overline{\text{FDIFV}}^G \qquad (4.10)$$

is the contribution to the temporal $\overline{\Delta T}^G$ change by the vertical diffusive heat flux $\Delta\overline{\text{FDIFV}}^G$, and $\Delta(\overline{\text{TCONV}})^G$ is the contribution to the temporal $\overline{\Delta T}^G$ change by the vertical convective heat flux $\Delta\overline{\text{FCONV}}^G$.

The diffusive heat flux should always transport heat downward if the temperature increases upward. In general the convective heat flux transports heat upwards because when convection takes place the more dense water above is generally colder than the less dense water below; however, due to the effect of salinity on the density (Eqs. 3.3 and 3.4), it is possible that the convective heat flux can be downward. The heat flux by advection can be of either sign.

Vertical integration of Eq. (4.3) from the surface (z = 0) to the bottom (z = -D) and use of the boundary conditions

$$\Delta\overline{\text{FADVV}}^z = \Delta\overline{\text{FCONV}}^z = 0 \qquad (4.11)$$

$$\Delta\overline{\text{FDIFV}}^z = \Delta\overline{\text{FTS}}^z \qquad (4.12)$$

at z = 0, with $\Delta\overline{\text{FTS}}^z$ the zonal mean $2xCO_2 - 1xCO_2$ ocean surface heat flux difference, and

$$\Delta\overline{\text{FADVV}}^z = \Delta\overline{\text{FDIFV}}^z = \Delta\overline{\text{FCONV}}^z = 0 \qquad (4.13)$$

at $z = -D$, gives

$$\rho c \frac{\partial (\overline{\Delta T})^z}{\partial t} = \{\Delta \overline{TADVM}\}^z + \{\Delta \overline{TDIFM}\}^z + \Delta \overline{FTS}^z \ , \qquad (4.14)$$

where the terms within the braces are the vertical integrals of the quantities defined in Eqs. (4.4) and (4.6).

Integrating Eq. (4.14) from the Antarctic coast to the North Pole and dividing by the corresponding length gives

$$\rho c \frac{\partial}{\partial t} (\overline{\Delta T})^G = \Delta \overline{FTS}^G \ , \qquad (4.15)$$

which states that the CO_2-induced vertically integrated global mean temperature change is the result of the CO_2-induced global mean ocean surface heat flux.

In the analysis that follows, Eqs. (4.3) and (4.8) have been integrated in time over one-year periods, and the left-hand sides have been calculated exactly from the temperature history data stored once per simulated day during the $1xCO_2$ and $2xCO_2$ simulations. The right-hand sides of the time-integrated Eqs. (4.3) and (4.8) have been calculated from v, w and T also using the once-per-day values from the history data. However, since the time step for the integration of the OGCM was one hour, it is likely that this one-per-day sampling causes a sampling error in the calculated components. Two other sources of error were possible in the analysis. First, the ΔT change due to convection that was saved during the $1xCO_2$ and $2xCO_2$ simulations needs to be correctly applied in the analysis. Such a correct application is described

in Appendix A. Second, the ocean surface heat flux for the ice-covered ocean was not saved during the first 12 years of the $1xCO_2$ simulation. Therefore, as described in Appendix B, a method was developed and used to reconstruct the missing ocean surface heat flux. However, even with the correct application of the saved convective heat flux and the reconstruction of the ice-sea heat flux, the sampling errors can result in a difference between the left- and right-hand sides of the time-integrated forms of Eqs. (4.3) and (4.8). Therefore, in the following discussion we will examine this error and compare it with the individual heat flux components. The latter have been computed here only for year 12 of the $1xCO_2$ and $2xCO_2$ simulations. This temporal limitation of the analysis was made to economize on computer time and will be removed in the sequel to this study.

4.2. Global Mean Oceanic Heat Budget

In this section we consider the global mean oceanic heat budget as defined by Eq. (4.8) and its vertical integral Eq. (4.15). We first show how much heat is gained by the ocean through its surface when the CO_2 concentration is doubled, and the corresponding temperature change. Then we evaluate the contribution of each heat transport process to this warming.

4.2.1. Vertically-integrated heat budget, Eq. (4.15)

The evolutions of the annual global mean ocean surface heat fluxes for the $1xCO_2$ and $2xCO_2$ simulations are shown in Fig. 4.1a

together with the evolution of the $2xCO_2 - 1xCO_2$ heat flux difference. As a whole, the ocean gains heat from the atmosphere in both the $1xCO_2$ and $2xCO_2$ simulations, with values of about 2 W/m^2 and 5 W/m^2, respectively. Thus, neither the $1xCO_2$ nor $2xCO_2$ simulation achieved equilibrium during the 20-year integration. Figure 4.1a shows that when the CO_2 concentration was doubled, the ocean gained an additional amount of heat at a rate of about 3 W/m^2. This corresponds to a warming of the entire ocean of only about 0.005°C/year. This small rate of warming is due to the large heat capacity of the ocean.

Figure 4.1b shows the evolution of the time-integrated ocean surface heat flux for the $1xCO_2$ and $2xCO_2$ simulations together with their difference. The total amount of CO_2-induced heating of the ocean at the end of year 20 is about $1.6x10^9$ J/m^2 which corresponds to a warming of the entire ocean of only about 0.1°C, again as a result of the ocean's large heat capacity.

4.2.2. Vertical distribution of the heat budget, Eq. (4.8)

a. Time evolution of the temperature change

The evolution of the global mean ocean temperature change induced by the CO_2 doubling is shown in Fig. 4.2 as a function of depth. This figure is an extension to year 20 of the results shown in the lower panel of Fig. 2.8. Both Figs. 2.8 and 4.2 show that the warming of the ocean resulting from the $2xCO_2 - 1xCO_2$ ocean surface heat flux begins at the top of the ocean and gradually penetrates into the interior of the ocean. This differs markedly

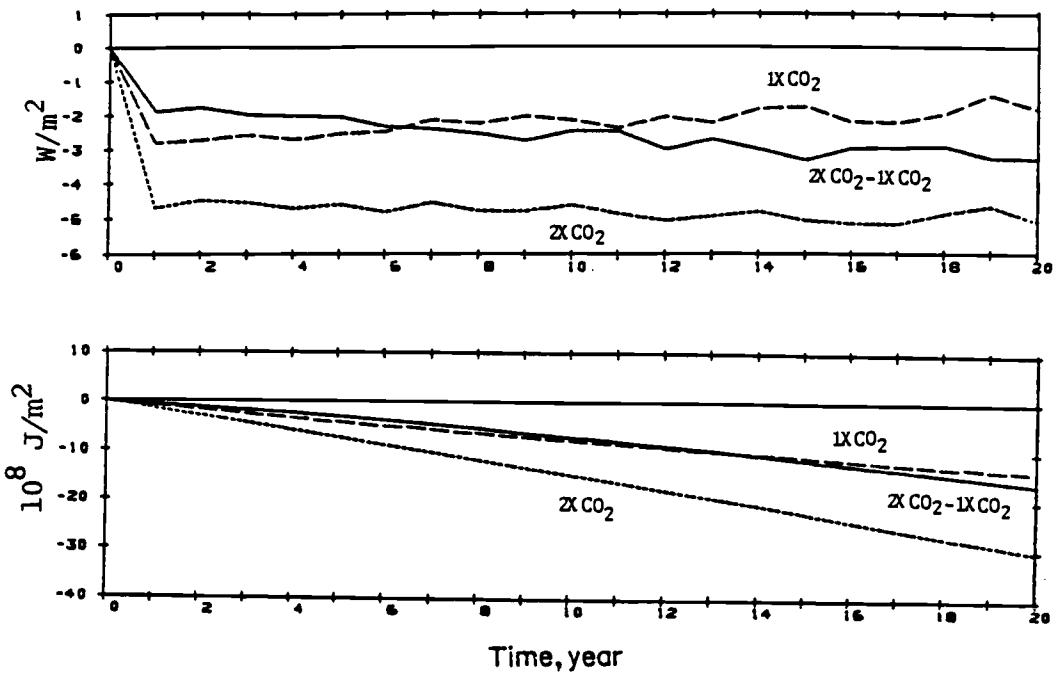

Fig. 4.1. Evolution of the global mean ocean surface heat flux for the $1xCO_2$ and $2xCO_2$ simulations and for the $2xCO_2 - 1xCO_2$ heat flux differences (a) versus time and (b) integrated with respect to time. A negative value represents a flux from the atmosphere into the ocean.

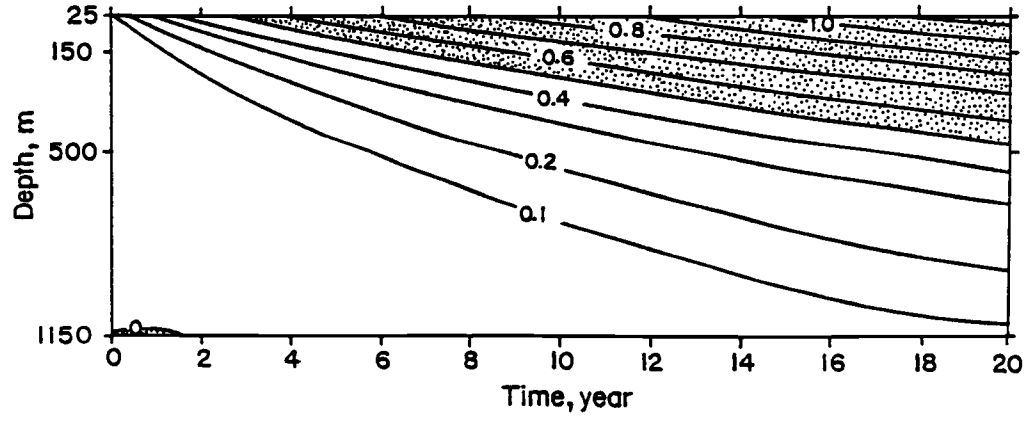

Fig. 4.2. The time-depth distribution of the $2xCO_2 - 1xCO_2$ difference in the global mean ocean temperature (°C).

from the vertically-more-uniform warming of the atmosphere shown in Fig. 2.8. In the next section we analyze the vertical heating distribution and the physical processes that are responsible for the vertical transport of heat into the global ocean.

b. Vertical heat flux

Figure 4.3a presents the vertical heat flux averaged for year 12 of the $1xCO_2$ and $2xCO_2$ simulations together with the $2xCO_2 - 1xCO_2$ differences. This figure clearly shows again that neither the $1xCO_2$ nor the $2xCO_2$ simulation reached equilibrium after only 12 years because in both simulations the total vertical heat flux convergence is nonzero. The heat flux is downward in both simulations from the surface to about 2500 m. The downward heat flux of the $2xCO_2$ simulation is much larger than that of the $1xCO_2$ simulation above 750 m. Figure 4.3a also shows that the difference between the $2xCO_2$ and $1xCO_2$ vertical heat fluxes is downward into the ocean everywhere above 1500m.

Figure 4.3b presents the results that Bryan and Spelman (1985) obtained with the sectorial version of the GFDL coupled atmosphere/ocean general circulation model without the annual insolation cycle. This figure shows that the $1xCO_2$ control run is very close to equilibrium. This equilibrium was obtained using the distorted physics method of Bryan (1984) in which the tendency terms in the primitive equations are multiplied by a factor larger than unity. This acceleration method was not feasible in the OSU coupled model runs in which the annual insolation cycle was

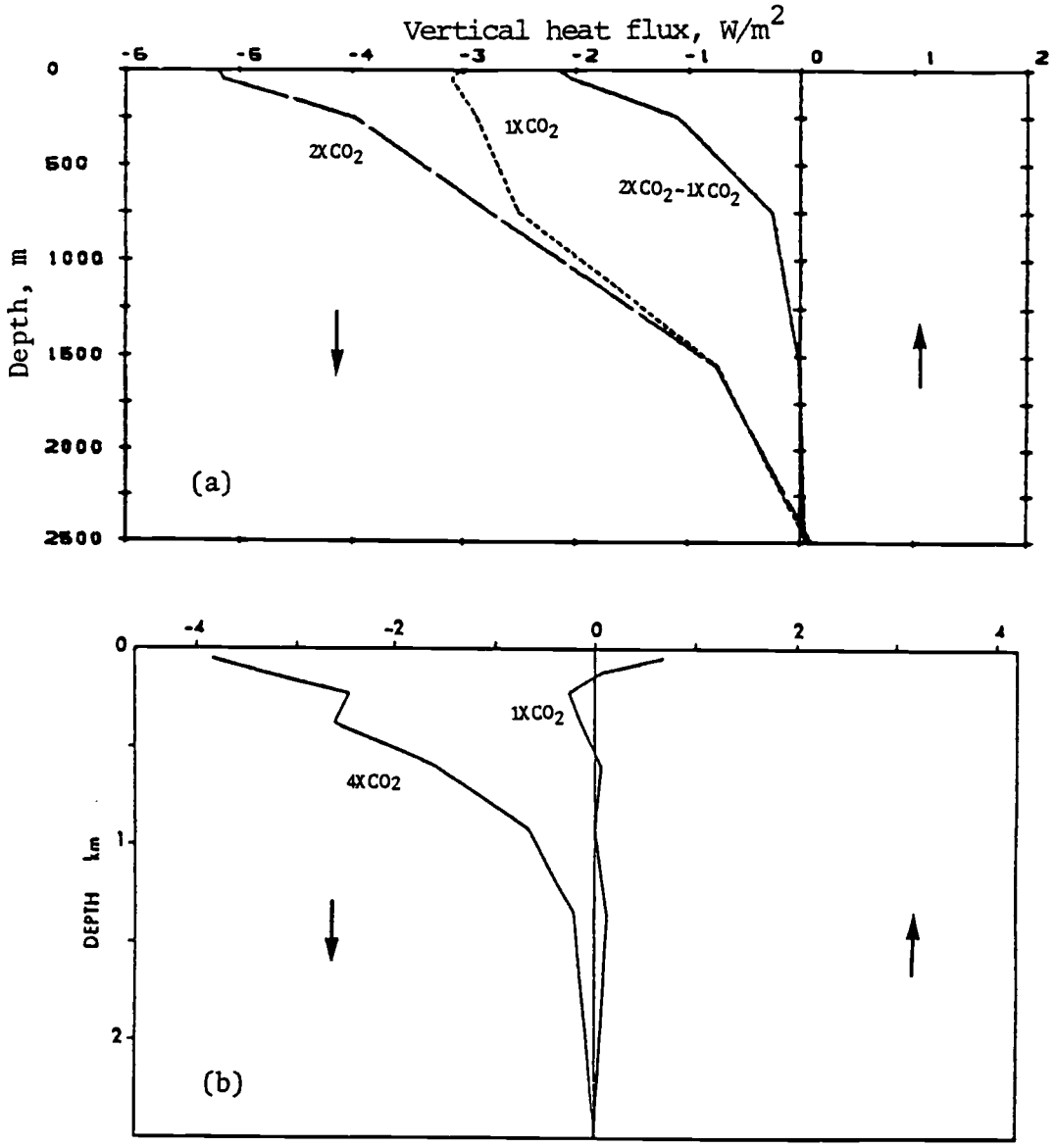

Fig. 4.3. Annual global mean total vertical heat flux for: (a) year 12 of the OSU $2xCO_2$ and $1xCO_2$ simulations and the $2xCO_2-1xCO_2$ differences and (b) years 20-30 of the GFDL $4xCO_2$ and $1xCO_2$ simulations from Bryan and Spelman (1985). The arrows show the signs of the upward (↑) and downward (↓) heat fluxes.

included and the atmosphere and ocean were synchronously coupled. However, the $2xCO_2-1xCO_2$ heat flux difference of the OSU CGCM (Fig. 4.3a) is quite similar to the $4xCO_2-1xCO_2$ heat flux difference of the GFDL CGCM, which is essentially given by the $4xCO_2$ curve because the $1xCO_2$ flux is near zero, even quantitatively considering the latter experiment is a CO_2 quadrupling and the former is a CO_2 doubling. Thus, it appears that insofar as the total vertical heat flux difference is considered, the issue of the control's equilibrium is not of paramount importance.

Figure 4.4 shows the temperature change due to the convergence of the vertical heat fluxes presented in Fig. 4.3a for the OSU model as calculated from the terms on the right-hand side of Eq. (4.8). It can be seen that in year 12 of both the $1xCO_2$ and $2xCO_2$ simulations the ocean warmed from the surface to 2500 m with a maximum warming in the 50-250 m layer. Figure 4.4b gives the actual temperature change computed from the left-hand side of Eq. (4.8) using the CGCM temperature history data. It can be seen here that the largest warming actually occurred in the surface layer for both the $1xCO_2$ and $2xCO_2$ simulations. The difference between the temperature changes of Fig. 4.4a and 4.4b is given in Fig. 4.4c. This figure shows nonzero values in the upper three ocean model layers as a result of the previously mentioned sampling errors. However, the $2xCO_2-1xCO_2$ temperature errors are everywhere quite small, indicating the systematic nature of the error for both the $1xCO_2$ and $2xCO_2$ simulations. Consequently, the reconstructed $2xCO_2-1xCO_2$ temperature differences, which are based on the

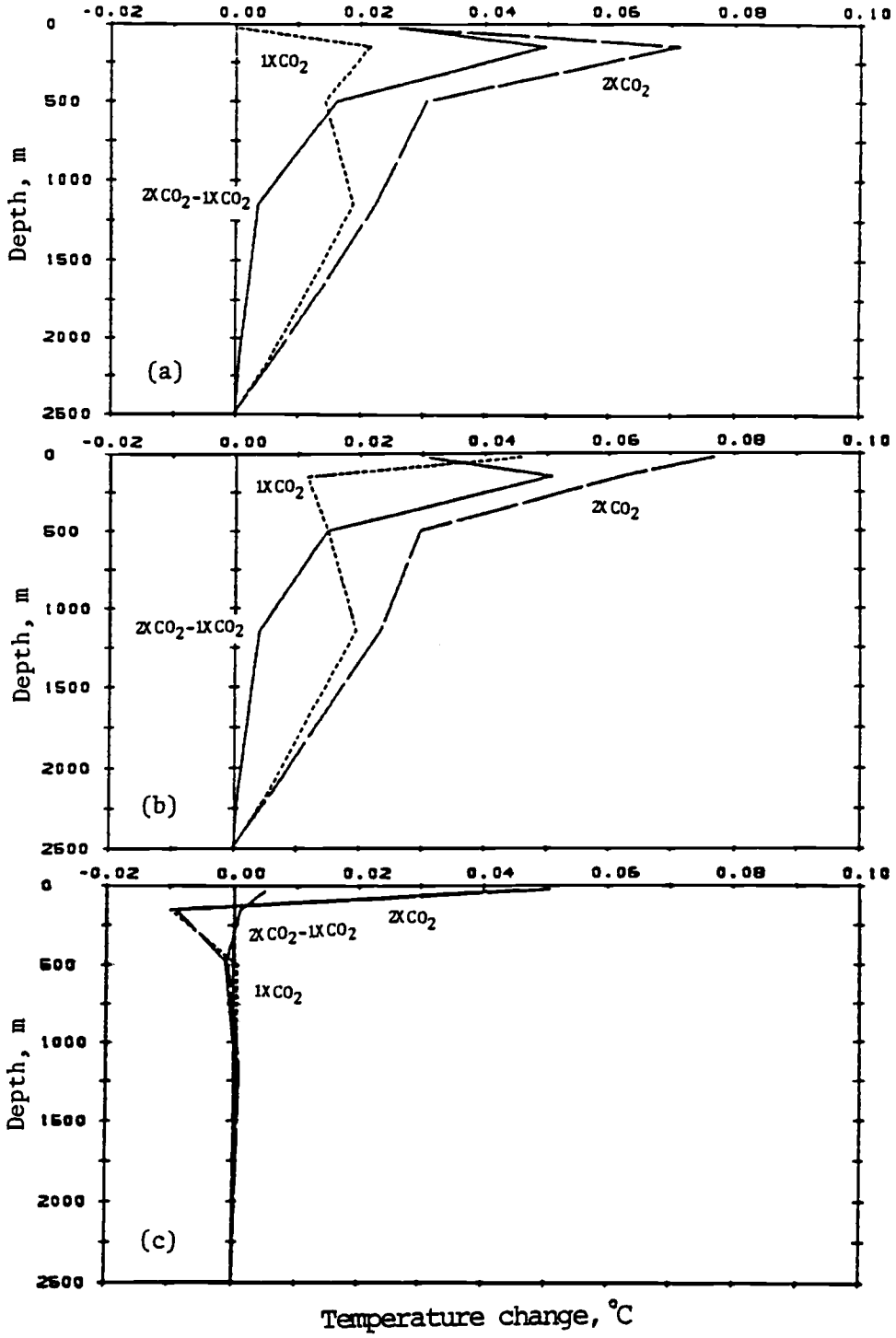

Fig. 4.4. Global mean temperature change for year 12 of the OSU CGCM $1xCO_2$ and $2xCO_2$ simulations, and the $2xCO_2 - 1xCO_2$ difference: (a) changes computed from the right-hand side of Eq. (4.8), (b) changes computed from the left-hand side of Eq. (4.8), and (c) the left-hand side of Eq. (4.8) minus the right-hand side.

reconstructed components of the heat flux differences following Eq. (4.8), are in good agreement with the actual $2xCO_2-1xCO_2$ temperature differences. Therefore, this gives confidence in the reconstructed flux differences. The $2xCO_2-1xCO_2$ temperature changes of both Fig. 4.4a and 4.4b show a maximum warming below the surface of about 0.05°C per year in the 50-250 m layer. This is consistent with the rate that can be inferred from Fig. 4.2.

c. Contribution by individual physical processes

Figure 4.5 shows the vertical heat fluxes due to advection, $\Delta(\overline{FADVV})^G$, diffusion, $\Delta(\overline{FDIFV})^G$, and convection, $\Delta(\overline{FCONV})^G$, for the $NxCO_2-1xCO_2$ differences, as well as for the individual $NxCO_2$ and $1xCO_2$ simulations, for both the OSU (N = 2, Fig. 4.5a) and GFDL (N = 4, Fig. 4.5b) model simulations.

For the $1xCO_2$ case, the upward heat flux by advection nearly balances the downward heat flux by diffusion in the GFDL study, but not in the OSU study where the heat fluxes by both diffusion and advection are downward. This again clearly shows that the OSU $1xCO_2$ simulation is not in equilibrium after only 12 years of integration. The heat fluxes by convection in both the OSU and GFDL $1xCO_2$ simulations are upward, with the former being about three times larger than the latter, perhaps because the OSU simulation was far from equilibrium.

For the $NxCO_2$ cases, Fig. 4.5 shows that both the OSU $2xCO_2$ and the GFDL $4xCO_2$ simulations are not in equilibrium. The total downward heat flux shown in Fig. 4.3 for both the OSU and GFDL

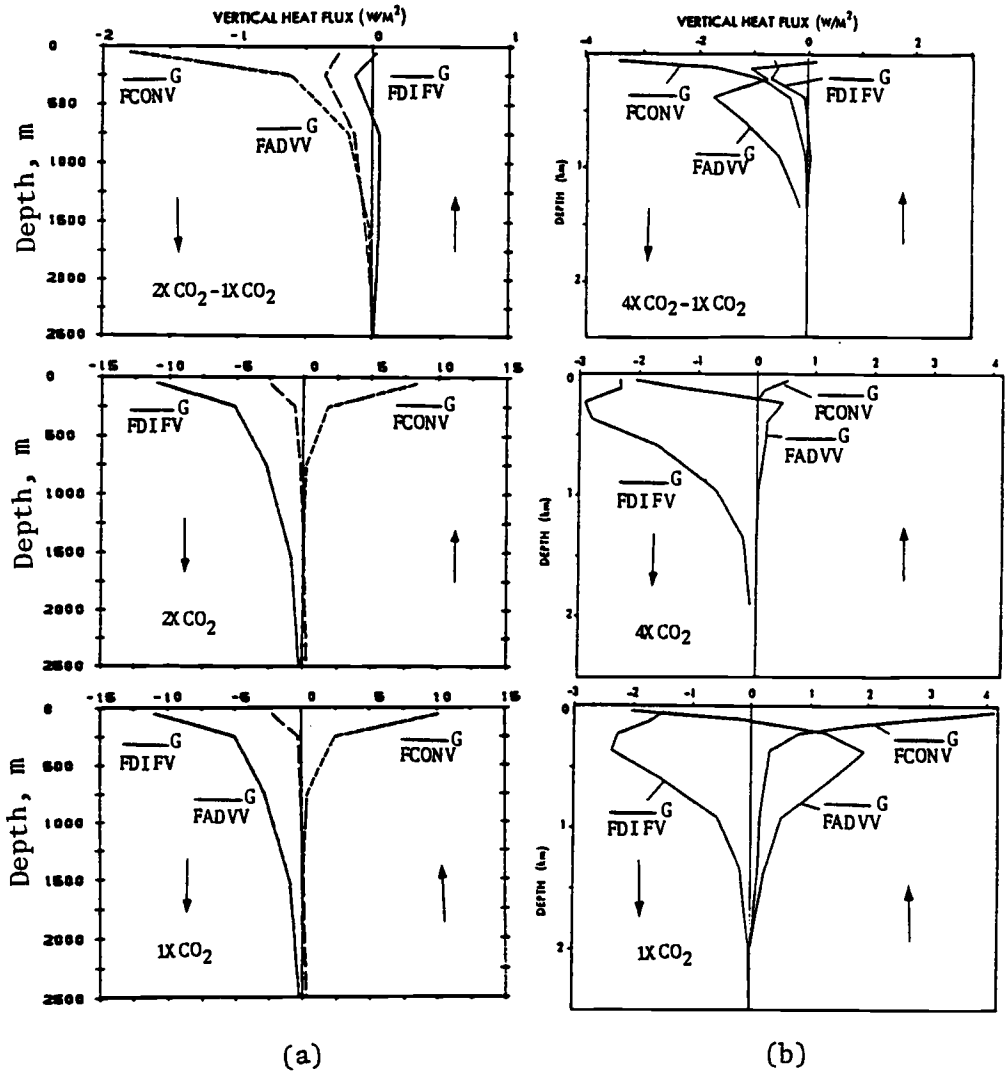

Fig. 4.5. Annual global mean heat flux by advection ($\Delta\overline{FADVV}^G$) diffusion ($\Delta\overline{FDIFF}^G$) and convection ($\Delta\overline{FCONV}^G$) for (a) year 12 of the OSU $2xCO_2-1xCO_2$ difference (upper panel), $2xCO_2$ (middle panel) and $1xCO_2$ (lower panel) simulations and (b) years 20-30 of the GFDL $4xCO_2-1xCO_2$ difference (upper panel), $4xCO_2$ (middle panel) and $1xCO_2$ (lower panel) simulations from Bryan and Spelman (1985).

simulations is principally due to diffusion, with a significant contribution by advection only near the surface.

The top panels of Fig. 4.5 for the $NxCO_2$-$1xCO_2$ heat flux differences show that the upward heat flux by convection is reduced for both models as a consequence of the increased CO_2 concentration. Furthermore, for both models the downward heat flux due to diffusion increased in magnitude near the surface and decreased in magnitude below about 750 m. In the OSU model the downward heat flux by advection has increased in magnitude; similarly, the advection in the GFDL model becomes less upward below 250 m and more downward above 250 m. Consequently, in both models the CO_2-induced surface heating is transported downward into the ocean by the reduced upward convective heat flux and the more downward (negative)/less upward (positive) advective heat flux. The similarity of these vertical heat flux results for the GFDL and OSU coupled models supports the conclusion of Bryan and Spelman (1985) that heat is transported more rapidly into the ocean than a passive tracer because of the reduction in the high-latitude convection in the $NxCO_2$ simulation compared with the $1xCO_2$ simulation.

The annual global mean temperature changes due to the convergence of the vertical heat flux and its components are shown in Fig. 4.6 for year 12 of the OSU $1xCO_2$ and $2xCO_2$ simulations together with the $2xCO_2$-$1xCO_2$ temperature differences. For both the $1xCO_2$ and $2xCO_2$ simulations, the temperature decrease by convection is nearly balanced by the temperature increase due to advection and diffusion. Thus, the total temperature change is the

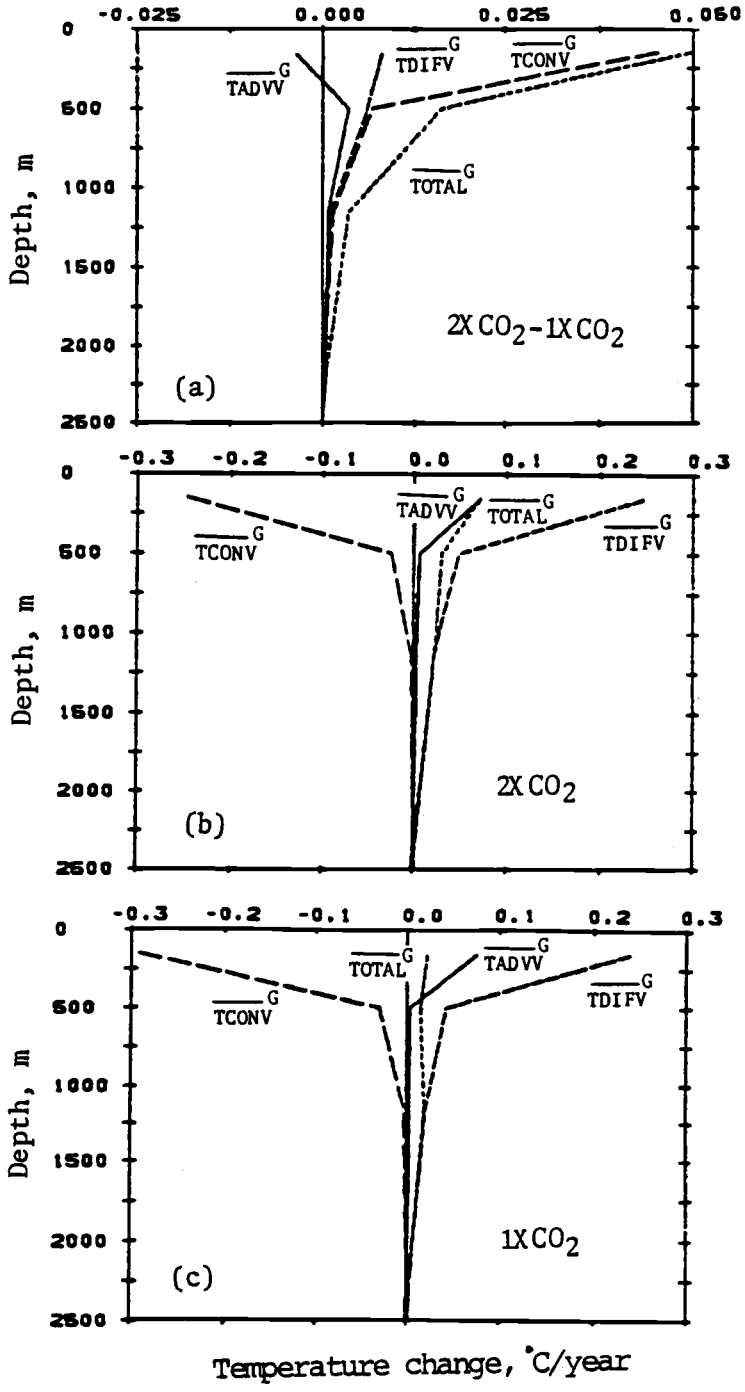

Fig. 4.6. Global mean temperature change by each individual process shown in Eq. 4.8 for (a) $2xCO_2-1xCO_2$ difference, (b) $2xCO_2$ simulation and (c) $1xCO_2$ simulation of the OSU CGCM year 12.

small residual of the larger changes due to the vertical advection, diffusion and convection. For the $2xCO_2-1xCO_2$ difference, the temperature change of each process decreases from the surface to the deep ocean and the total temperature change is mainly contributed by the convection.

4.3. Zonal Mean Oceanic Heat Budget

In Section 4.2 we have discussed the CO_2-induced changes in the oceanic heat fluxes and temperatures in terms of global means. In this section we describe the corresponding zonal mean changes as defined by Eq. (4.3) and its vertical integral Eq. (4.14). First we will present the changes in the vertically integrated heat budget. Then we will present the vertical distribution of the heat budget including the changes in the zonal mean temperature, its contributions by the divergent part of the heat flux and by the heat fluxes due to the individual physical processes.

4.3.1. Vertically integrated heat budget, Eq. (4.14)

To understand how the CO_2-induced heating penetrated into the ocean it is useful to examine the CO_2-induced net surface heat flux simulated by the coupled model. In Section 1 of this chapter (Eq. 4.14) we have shown that the vertically integrated zonal mean temperature change $(\overline{\Delta T})^z$ is the result of the vertically integrated meridional heat flux $(\Delta\overline{FADVM})^z + (\Delta\overline{FDIFM})^z$ and the ocean surface heat flux $(\Delta\overline{FTS})^z$. Figure 4.7 presents these quantities averaged over the entire 20-year period of the

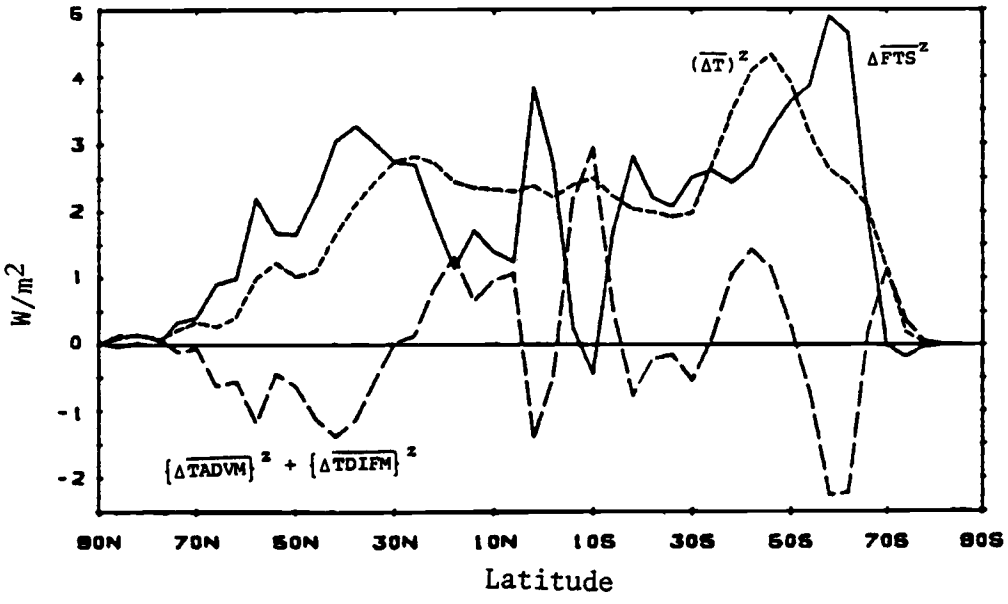

Fig. 4.7. Components of the CO_2-induced changes in the vertically integrated zonal mean oceanic heat budget averaged over the 20-year period of the simulations.

simulations. This figure shows that the CO_2-induced ocean surface heating was into the ocean (positive) virtually everywhere with maximum values at 60°S, the equator, and 40°N. The large value at 60°S is partly due to the large fraction of ocean at that latitude. However, the vertically integrated zonal mean temperature changes in Fig. 4.7 do not coincide with the changes in the ocean surface heat flux. Apparently, the vertically integrated meridional heat flux by advection and diffusion induced by the CO_2 doubling makes a non-negligible contribution to the warming of the vertically integrated ocean.

4.3.2. Vertical distribution of the heat budget, Eq. (4.3)

a. Time evolution of the temperature change

The latitude-depth distribution of the zonal mean $2xCO_2 - 1xCO_2$ ocean temperature change (left-hand side of Eq. 4.3) is shown in Fig. 4.8 integrated in time from the beginning of the coupled model simulation through years 4, 8, 12, 16 and 20. Each of the panels in this figure shows that the CO_2-induced zonal mean temperature changes are positive everywhere except in certain regions of the deep ocean where small negative temperature changes are found. The largest warming occurs near 30°N, 70°N and 35°S in the surface layer, and penetrates to a greater depth in the subtropics and high latitudes than in the tropics. After year 4 there are two warm cores located near 60°S and 70°N at 500 m.

The time evolution of the CO_2-induced temperature change shows that the warming penetrated from the surface to the intermediate ocean. This penetration occurred rapidly in the middle and high latitudes, and slowly in the tropics. After 4 years the largest warming occurred near 70°N with a maximum value of about 1.4°C in the surface layer. Two warm tongues extended downward and poleward from the surface near 30°N and 35°S. The 0.4°C isotherm penetrated to a depth of 250 m at 40°S, 50 m at the equator, 300 m near 30°N and 600 m near 70°N. The basic features of the temperature changes through year 8 are similar to those through year 4 except maximum values of 0.4°C and 0.6°C are found at 500 m near 60°S and 70°N, respectively. After 12 years the warming near 70°N was still confined to the surface layer while the warm core near 500 m increased to 1°C. The 0.4°C isotherm penetrated to 750 m at 65°S, 300 m near the equator, 500 m at 30°N and 1250 m at 70°N. The temperature changes through year 16 show that the warming near 30°N intensified to about 2.2°C in the surface layer. Meanwhile, the warming near 70°N significantly decreased and the largest warming in the surface layer was only 1.2°C. After 20 years the warming near 70°N decreased further, especially near 500 m where the warm core disappeared. However, the warming at 30°N continously increased to a maximum value of about 2.4°C. The warm tongue in the Southern Hemisphere continued to deepen through the 20 years of the simulations. After 20 years the 0.4°C isotherm reached 1200 m at 70°S, 400 m at the equator, 800 m at 30°N and 1400 m at 70°N.

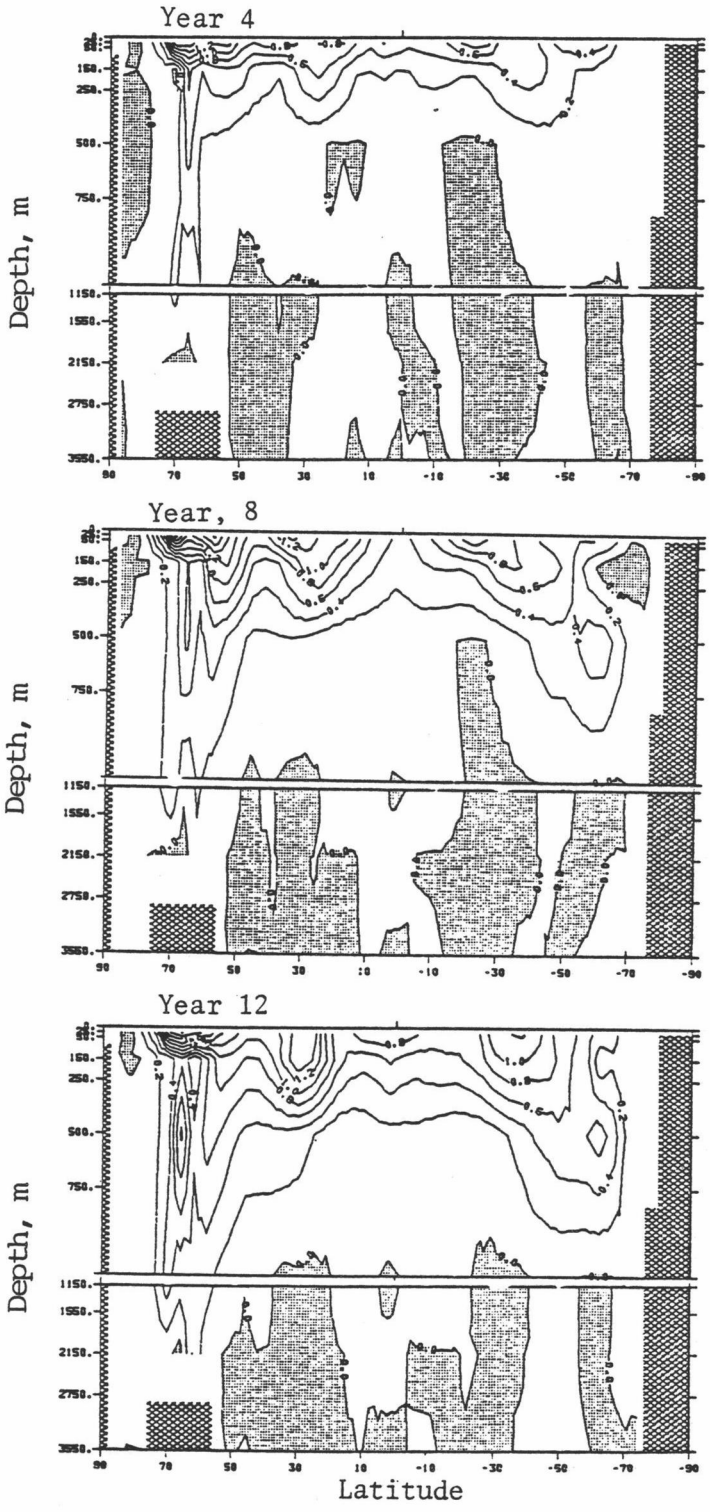

Fig. 4.8. Latitude-depth distribution of the $2xCO_2 - 1xCO_2$ differences in the annual zonal mean ocean temperature (°C) for years 4, 8, 12, 16 and 20. Negative values are shaded.

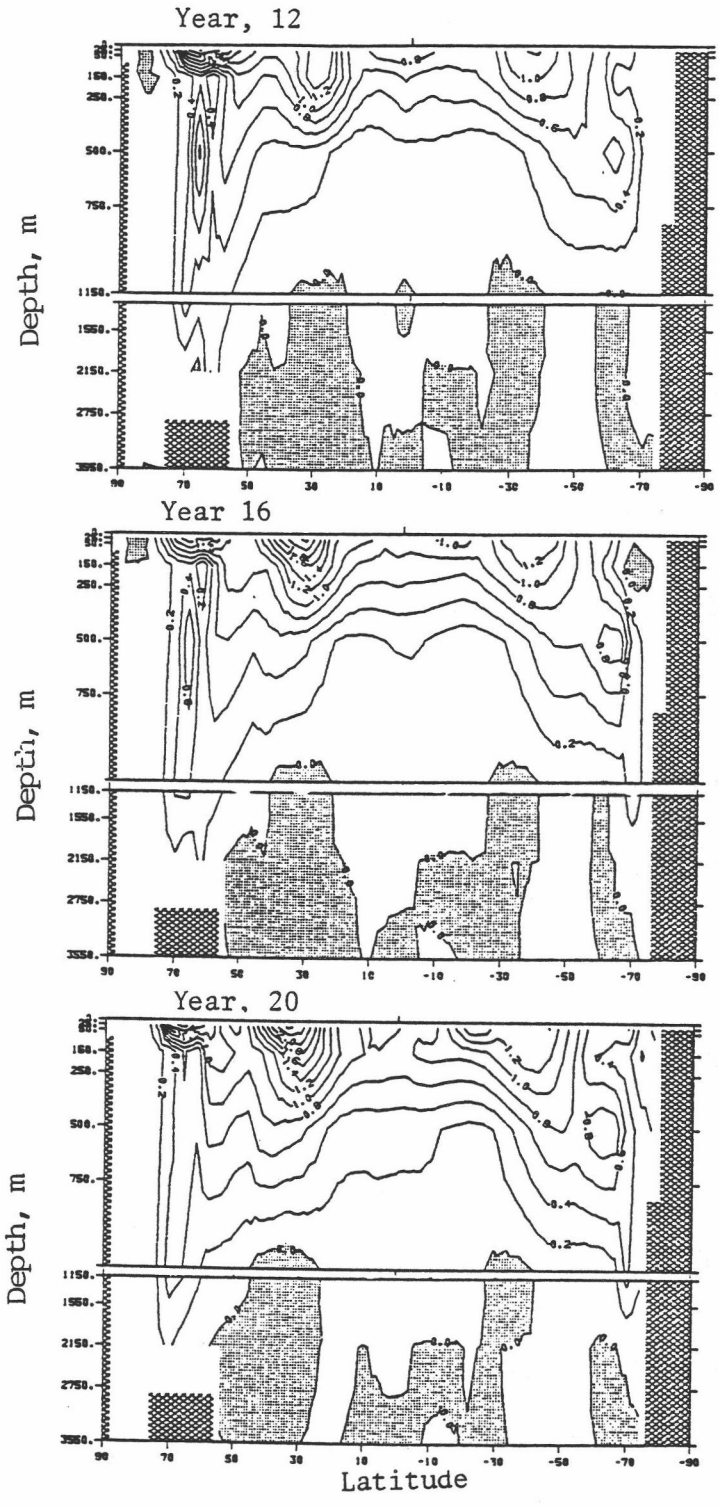

Fig. 4.8. (continued)

The latitudinal distributions of the $2xCO_2 - 1xCO_2$ temperature changes simulated by the coupled GCM are very similar to the latitudinal distribution of the excess ^{14}C over the pre-nuclear value that has been observed in the ocean (Fig. 2.1). This suggests that penetration into the ocean of the doubling CO_2-induced warming simulated by the model may be in reasonable agreement with what would actually occur in nature. In the following we examine how the CO_2-induced warming penetrated into the ocean and which physical processes are responsible for the resulting temperature changes.

b. Divergent part of the meridional and vertical heat fluxes

The analysis of the time evolution of the zonal mean oceanic heat budget can be performed using the stored history data for v, w and T. Alternatively, because the CO_2-induced temperature changes are due only to the divergent part of the heat flux, one can derive this divergent heat flux directly from the temperature changes by solving a Poisson equation with Neumann boundary conditions. We have chosen the latter type of analysis here because of its comparative economy in terms of computer resources and time. Therefore, this method of heat budget analysis is described below.

1) Method of analysis

Multiplication of the oceanic heat budget Eq. (3.7) by ρc and integration with respect to λ and t from 0 to 2π and from 0 to τ, respectively, yields

$$\rho c \delta T = \frac{1}{a\cos\phi} \frac{\partial}{\partial \phi} (\cos\phi \; F_\phi) + \frac{\partial F_z}{\partial z} , \tag{4.16}$$

where the cyclic boundary condition in the zonal direction has been used, and where

$$\delta T = \int_0^{2\pi} \int_0^{\tau} \frac{\partial T}{\partial t} \, dt d\lambda \tag{4.17}$$

$$F_\phi = \int_0^{2\pi} \int_0^{\tau} \rho c \left(-vT + \frac{A_H}{a} \frac{\partial T}{\partial \phi} \right) dt d\lambda , \tag{4.18}$$

and

$$F_z = \int_0^{2\pi} \int_0^{\tau} \left(-\rho c w T + \rho c \kappa \frac{\partial T}{\partial z} + Q_{conv} \right) dt d\lambda \tag{4.19}$$

Subtracting Eq. (4.16) for $1xCO_2$ from Eq. (4.16) for $2xCO_2$ gives

$$\rho c \Delta T = \frac{1}{a\cos\phi} \frac{\partial}{\partial \phi} (\cos\phi \; \Delta F_\phi) + \frac{\partial \Delta F_z}{dz} = \nabla \cdot \vec{\Delta F} \tag{4.20}$$

where

$$\Delta T = \delta T(2xCO_2) - \delta T(1xCO_2) \tag{4.21}$$

$$\Delta F_\phi = F_\phi(2xCO_2) - F_\phi(1xCO_2) \tag{4.22}$$

$$\Delta F_z = F_z(2xCO_2) - F_z(1xCO_2) \tag{4.23}$$

and $\vec{\Delta F}$ is the vector of the total $2xCO_2$-$1xCO_2$ heat flux difference.

In general we can write Eq. (4.20) as

$$\rho c \; \Delta T = \nabla \cdot \vec{\Delta F} = \nabla \cdot (\vec{\Delta F}_D + \vec{\Delta F}_{N,D}) , \tag{4.24}$$

where $\Delta\vec{F}_D$ is the divergent, irrotational part of $\Delta\vec{F}$ and $\Delta\vec{F}_{N,D}$ is the nondivergent, rotational part of $\Delta\vec{F}$. Thus, because $\nabla\cdot\Delta\vec{F}_{N,D} = 0$ by definition, the Eq. (4.24) becomes

$$\rho c\Delta T = \nabla.\Delta\vec{F}_D \tag{4.25}$$

$$= \nabla^2\Phi \ , \tag{4.26}$$

where Φ is the potential defined by

$$\nabla\Phi = \Delta\vec{F}_D \ . \tag{4.27}$$

In spherical coordinates Eq. (4.26) can be written as

$$\rho c\Delta T = \frac{1}{a\cos\phi}\frac{\partial}{\partial\phi}\left(\cos\phi\ \Delta F_{D,\phi}\right) + \frac{\partial\Delta F_{D,z}}{\partial z} \tag{4.28}$$

or

$$\rho c\Delta T = \frac{1}{a\cos\phi}\frac{\partial}{\partial\phi}\left(\cos\phi\frac{1}{a}\frac{\partial\Phi}{\partial\phi}\right) + \frac{\partial^2\Phi}{\partial z^2} \ , \tag{4.29}$$

where

$$\Delta F_{D,\phi} = \frac{1}{a}\frac{\partial\Phi}{\partial\phi} \tag{4.30}$$

and

$$\Delta F_{D,z} = \frac{\partial\Phi}{\partial z} \tag{4.31}$$

are the meridional and vertical components of the divergent heat flux vector, respectively. The boundary conditions for Eq. (4.29) are

$$\Delta F_{D,z} = \frac{\partial \Phi}{\partial z} = \begin{cases} \Delta FTS(\phi) & \text{at } z = 0 \\ 0 & \text{at } z = -D \end{cases} \tag{4.32}$$

$$\Delta F_{D,\phi} = \frac{1}{a}\frac{\partial \Phi}{\partial \phi} = 0 \qquad \text{at } \phi = \pm \frac{\pi}{2}\,, \tag{4.33}$$

where again ΔFTS is the ocean surface heat flux. (In the Southern Hemisphere the latter boundary condition for $\Delta F_{D,\phi}$ should be applied along the Antarctic coast. However, in this analysis the boundary condition is applied at the South Pole so that the dependent variables can be represented as a sum of Legendre polynomials.)

The Poisson equation (4.29) with its Neumann boundary conditions Eqs. (4.32) and (4.33) can be solved by expanding the potential Φ in Legendre polynomials in the meridional direction and by representing the vertical derivatives by finite differences. The details of solving this equation are given in Appendix C.

2) Results

Before presenting the results for $\Delta F_{D,\phi}$ and $\Delta F_{D,z}$, we show in Fig. 4.9 the latitude-depth distribution of the zonally-integrated $2xCO_2 - 1xCO_2$ ocean temperature change integrated in time from the beginning of the coupled model simulations through years 4, 12 and 20. This zonally-integrated temperature change, defined by Eq. (4.17), is presented here in addition to the zonal mean temperature change shown in Fig. 4.8 because the analysis described in the preceding section is for the zonally-integrated heat budget. Of course the zonal mean can be obtained from the zonal

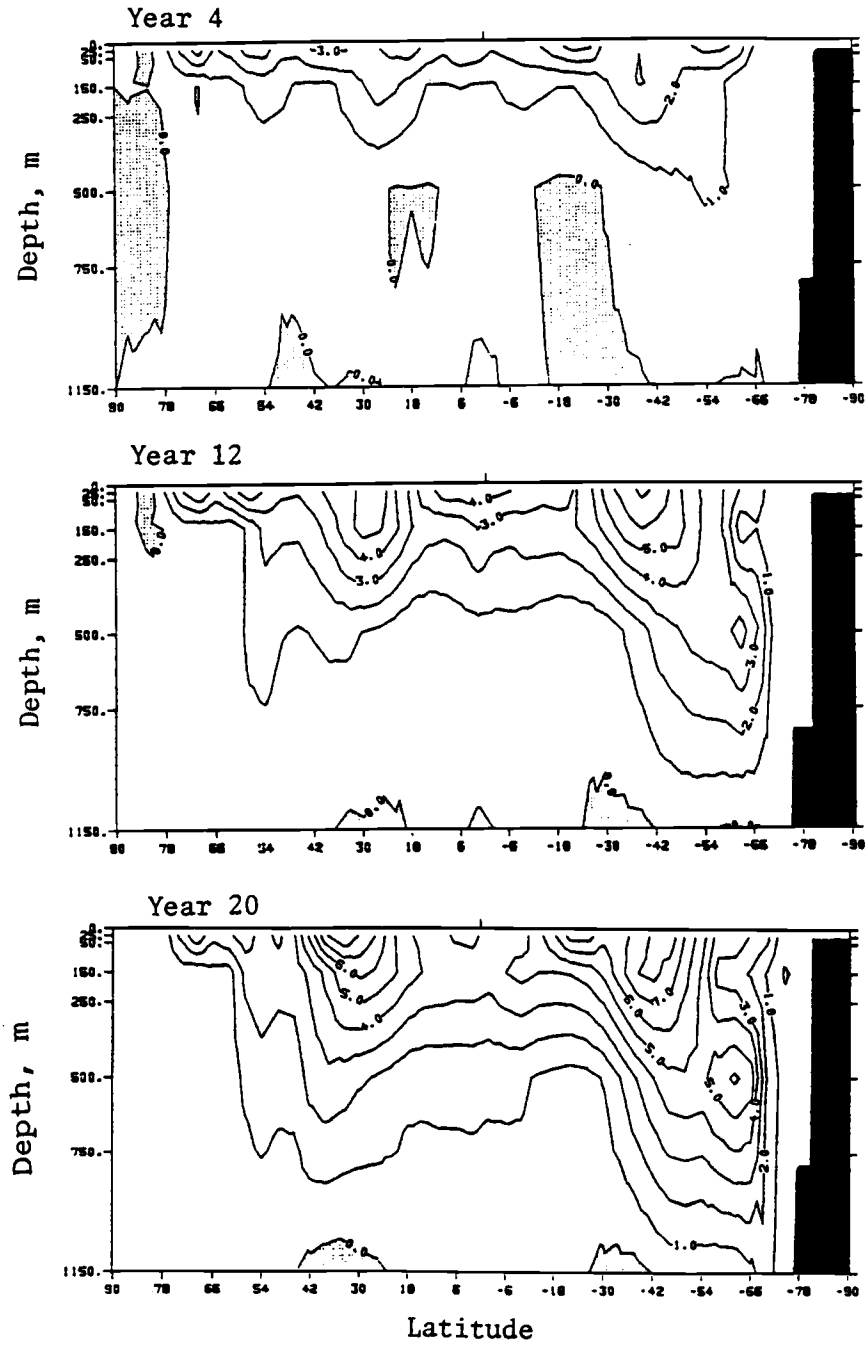

Fig. 4.9. Latitude-depth distributions of the $2xCO_2 - 1xCO_2$ difference in the annual zonally-integrated ocean temperature (°C) through years 4, 12 and 20. Negative values are shaded.

integral by dividing by the number of grid points on the ocean at each latitude. However, since this number is a function of latitude, it enters in the meridional differential operators in the zonal mean heat budget equations (not shown), thus complicating the analysis. Consequently, for simplicity, we have analyzed the zonal integral heat budget.

Figure 4.9 shows that the warming penetrated from the surface to the intermediate ocean and occurred more rapidly in the middle and high latitudes than in the tropics. The warming maxima found near 30°N, 55°N and 65°S correspond to the warming maxima shown in Fig. 4.8. The large warming of the zonally-integrated ocean temperature in the Southern Ocean is due in part to the large zonal extent of the ocean there.

The zonally-integrated divergent vertical and meridional heat fluxes, $\Delta F_{D,z}$ and $\Delta F_{D,\phi}$, are shown in Fig. 4.10 for years 4, 12 and 20. The vertical heat flux distributions (Fig. 4.10a) show a large downward heat transport near 60°S which corresponds to the location of the zonally-integrated maximum warming shown in Fig. 4.9. In the Northern Hemisphere the largest downward transports occur at 40°N and 60°N which also correspond to the warming maxima shown there in Fig. 4.9. Upward heat transport takes place in the subtropics near 10°S through almost all the ocean layers, and occurs in midlatitudes near 25°N and 40°S below 150 m in year 4, and below 400 m in year 20. The pattern of the vertical heat fluxes for years 12 and 20 is quite similar to that of year 4. The only significant differences are that the midlatitude upward heat

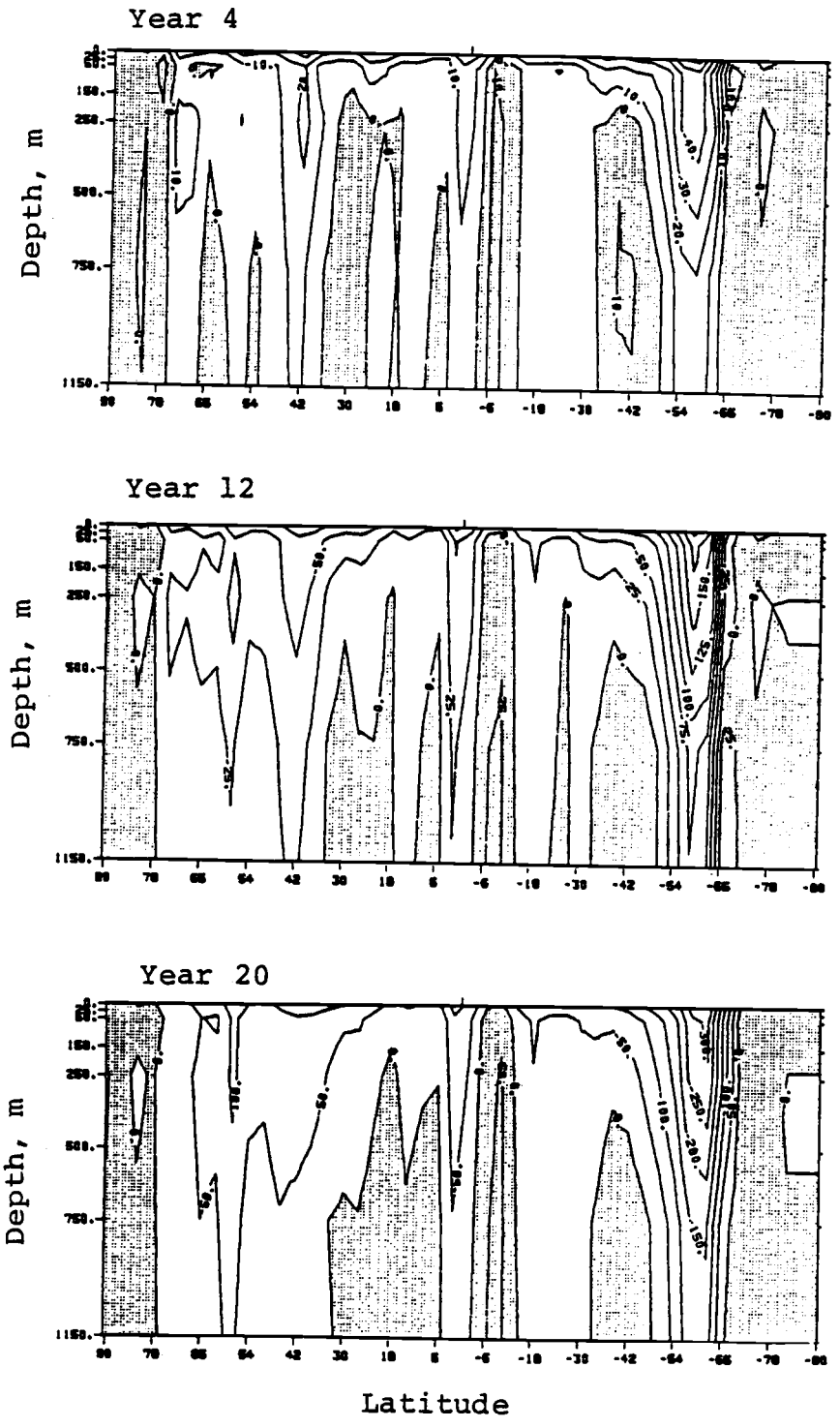

Fig. 4.10a. Latitude-depth distributions of $\Delta F_{D,z}$ (10^8 J/m^2), integrated through years 4, 12 and 20, with positive (upward) values shaded.

fluxes become weak in the first two OGCM layers and the downward heat fluxes increase as more heat enters the ocean with increasing time.

The meridional heat flux (Fig. 4.10b) has a structure that is almost independent of depth. Poleward heat fluxes occur in low and midlatitudes, and equatorward heat fluxes take place in high latitudes. The heat fluxes discussed here are the divergent, nonrotational part which contribute to the temperature change. Since both $\partial \Delta F_{D,\phi}/\partial z$ and $\partial \Delta F_{D,z}/a\partial\phi$ are equal to $\partial^2\phi/a\partial\phi\partial z$ [see Eqs. (4.30) and (4.31)], and the meridional heat flux $\Delta F_{D,\phi}$ is several orders of magnitude larger than the vertical heat flux $\Delta F_{D,z}$, $\partial \Delta F_{D,\phi}/a\partial\phi$ is several orders of magnitude larger than $\partial \Delta F_{D,\phi}/\partial z$. Thus, it is not surprising that $\Delta F_{D,\phi}$ has a structure that is almost independent of depth.

Figure 4.11 shows the zonally-integrated temperature changes due to the vertical and horizontal heat fluxes. The temperature changes due to the vertical heat flux (Fig. 4.11a) are very similar to the actual zonally-integrated temperature changes (Fig. 4.9), while the temperature changes due to meridional heat flux (Fig. 4.11b) are negligibly small everywhere except near 60°S where the warming is as large as 1°C at year 20. Therefore, from these results we conclude that the CO_2-induced warming of the ocean occurs predominantly through the downward transport of heat, with the meridional heat transport having only a secondary role.

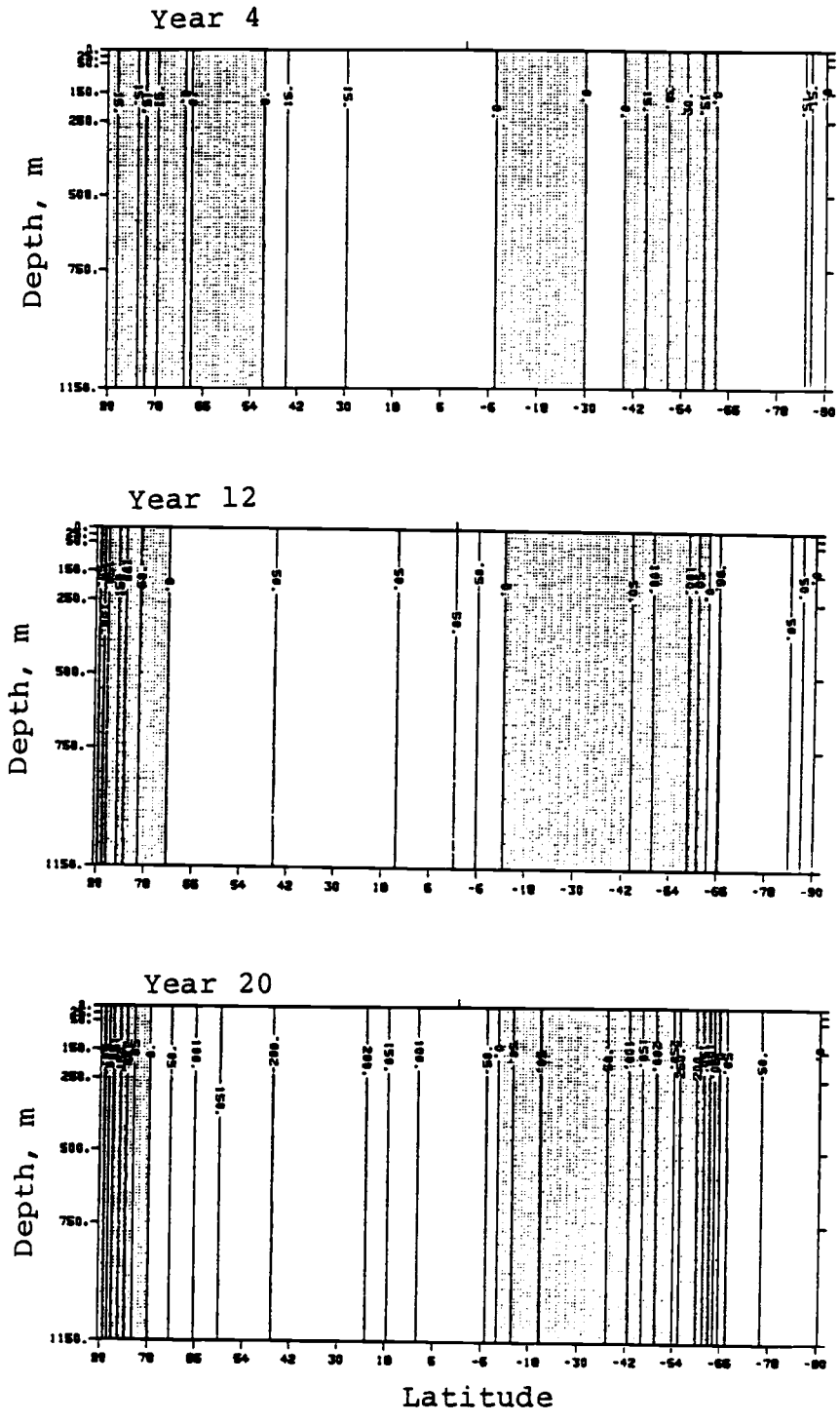

Fig. 4.10b. Latitude-depth distributions of $\Delta F_{D,\phi}$ (10^{10} J/m^2) integrated through years 4, 12 and 20, with negative (southward) values shaded.

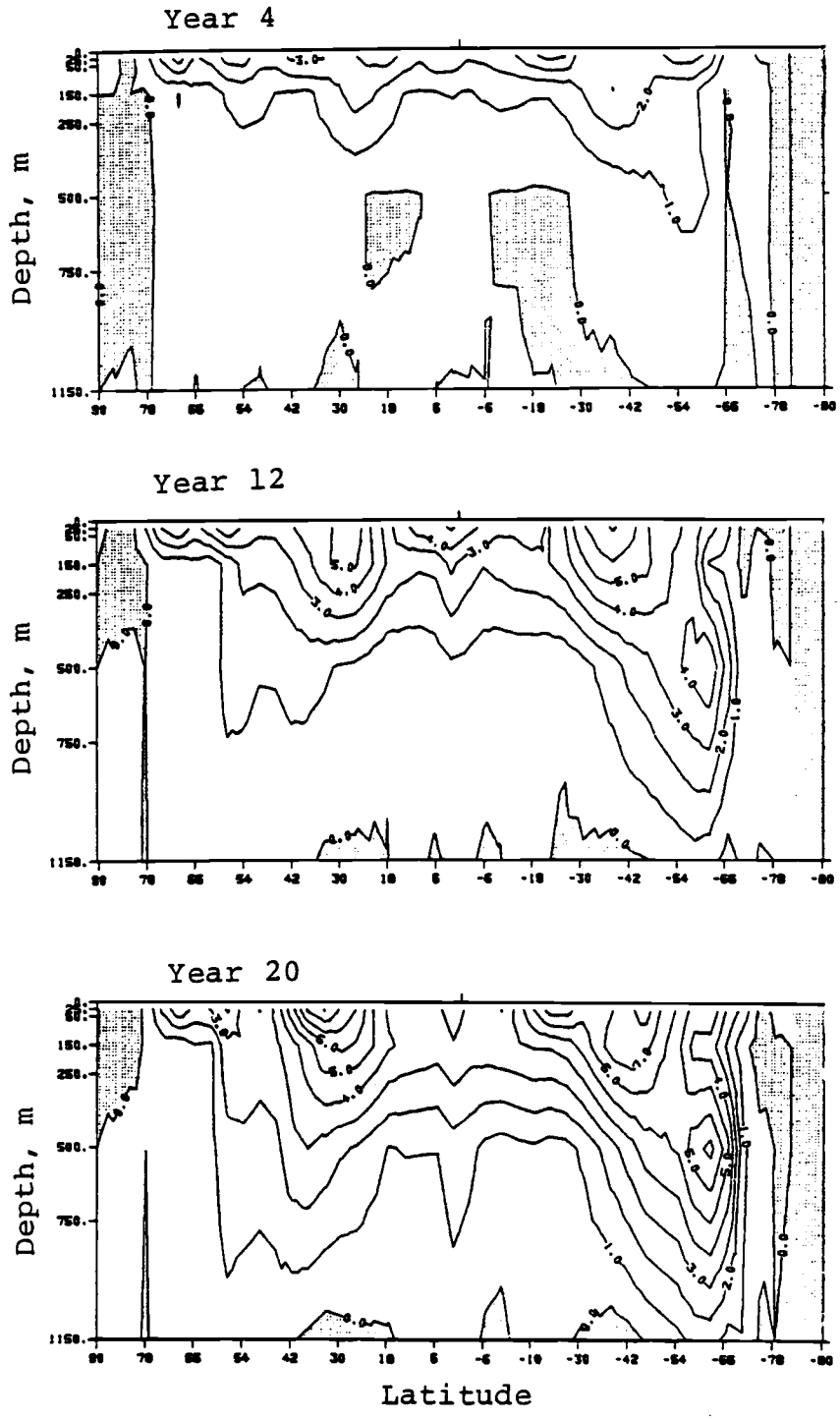

Fig. 4.11a. Latitude-depth distribution $\frac{1}{\rho c}\frac{\partial \Delta F_{D,z}}{\partial z}$ (°C) integrated through years 4, 12 and 20, with negative values shaded.

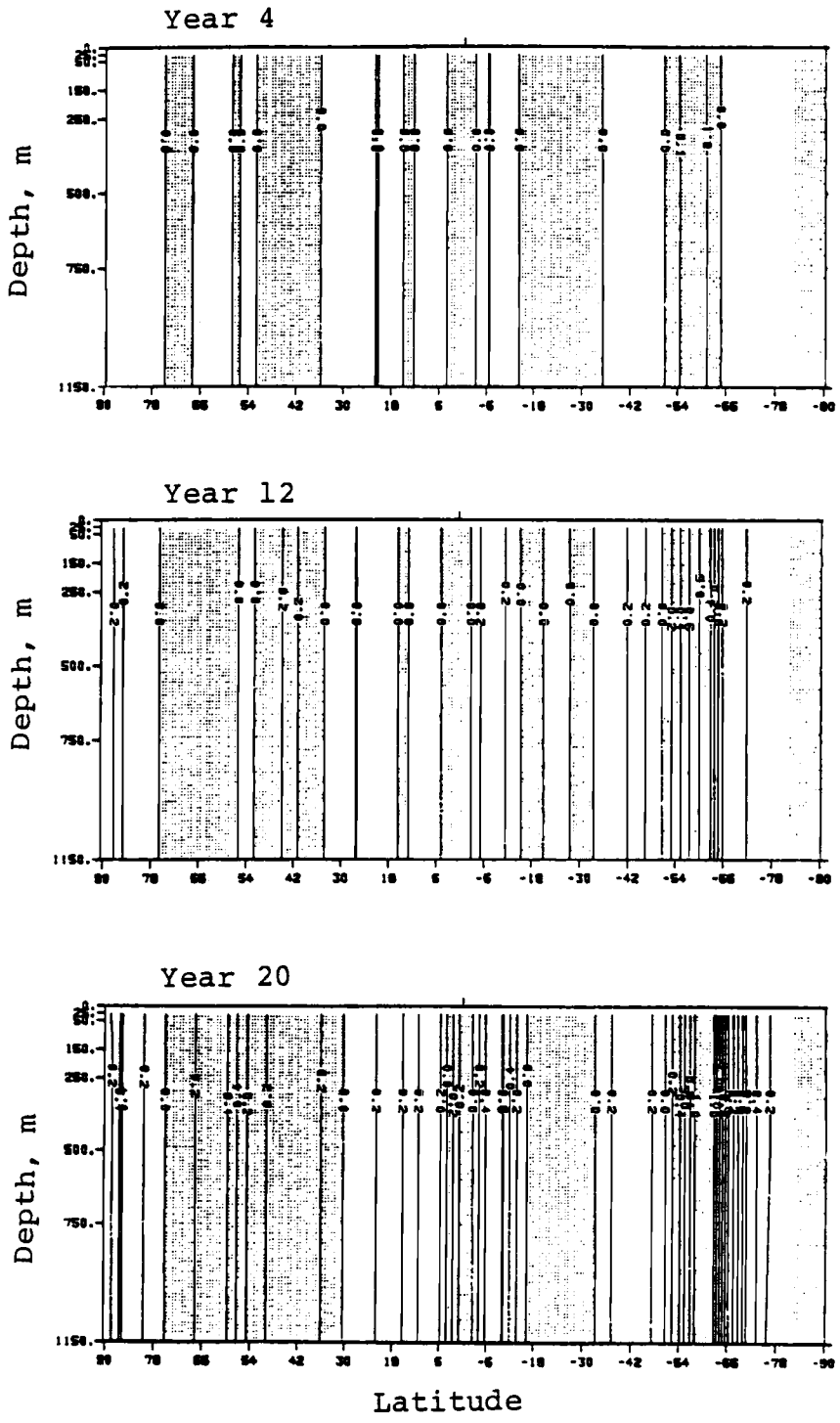

Fig. 4.11b. Latitude-depth distributions of $\frac{1}{\rho c a \cos\phi} \frac{\partial}{\partial \phi} (\cos\phi \Delta F_{D,\phi})$ integrated through years 4, 12 and 20, with negative values shaded.

c. Contribution by individual physical processes

In the previous section we have shown the relative roles of the divergent, nonrotational vertical and meridional heat transports that were derived directly from the temperature history data by solving a Poisson equation. However, the actual heat transport can be obtained from the stored history data for v, w and T. Because such an analysis is much more demanding of computer resources than the preceding analysis, we have performed the analysis here only for year 12 to correspond to the global heat budget analysis of Section 4.2. In Section 4.1 we introduced the First Law of Thermodynamics and defined the zonal mean fluxes and corresponding temperature changes due to the physical processes of advection, diffusion and convection [Eq. (4.3)]. In the following we present these fields for year 12 of the $2xCO_2$-$1xCO_2$ simulations. For the heat transport processes we show the annual mean value for year 12, while for the temperature change we show the value integrated over year 12.

1) Changes due to the total vertical and meridional heat transports

Figure 4.12 shows the annual zonal-mean total vertical and meridional heat flux components, $\Delta F_z = [\overline{\Delta FADVV}^z + \overline{\Delta FDIFV}^z + \overline{\Delta FCONV}^z]$ and $\Delta F_\phi = [\overline{\Delta FADVM}^z + \overline{\Delta FDIFM}^z]$, respectively. The total vertical heat flux is about four orders of magnitude smaller than the total meridional heat flux. The largest downward vertical heat flux occurred near 65°N at 750 m; this corresponds to the strong

vertical motion in that region (Fig. 3.11). In the midlatitude regions heat is also transported downward. The upward heat transport near the tropics in the upper layer might be due to the intensification of upwelling when the CO_2 concentration is doubled as discussed earlier. Figure 4.12b shows that the largest poleward heat transport occurred near 15°N, while everywhere else the meridional heat transport is relatively small. Equatorward heat transport is found in the second and third OGCM layers in both hemispheres.

The temperature change for year 12 is shown in Fig. 4.13 together with the temperature change due to the vertical and meridional heat fluxes. The largest warming during year 12 occurred at the 65°N, equator and 65°S in the surface layer, and near 30°N in the second layer of the OGCM. The largest cooling occurred near 50°N, 20°N and 20°S in the surface layer, and at 65°N in the third OGCM layer. The temperature changes in the Northern Hemisphere are significantly larger than those in the Southern Hemisphere which might be caused by the smaller oceanic area of the Northern Hemisphere. The temperature changes due to the vertical and meridional heat fluxes are nearly equal and of opposite sign, especially in the upper layers of the ocean. Comparing the panels of Fig. 4.13 shows that most of the cooling and warming areas in Fig. 4.13a correspond to the cooling or warming areas in Fig. 4.13b. This agrees with the conclusion of the previous section that the CO_2-induced warming of the ocean occurs predominantly through the downward transport of heat.

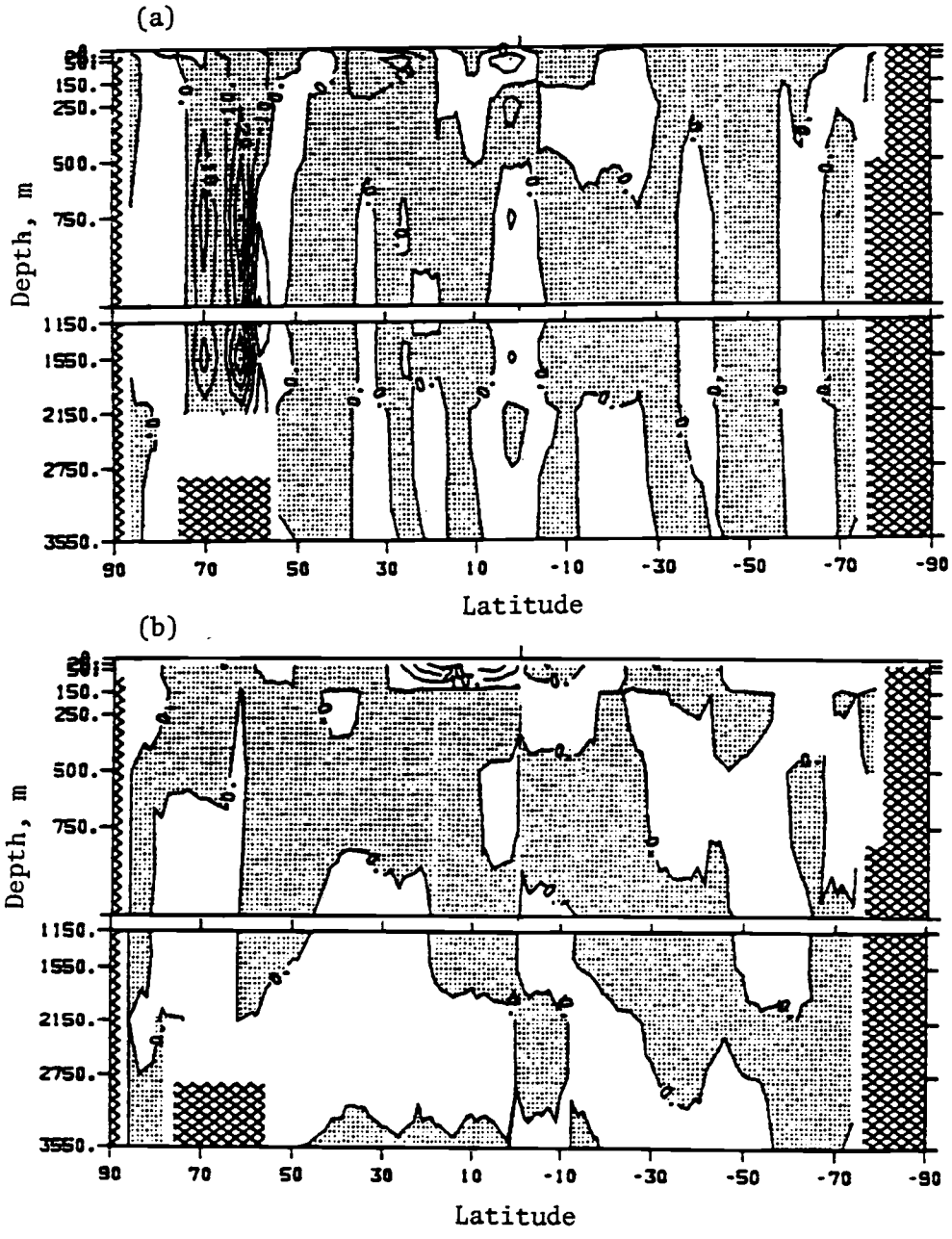

Fig. 4.12. Latitude-depth distributions of the annual zonal mean CO_2-induced heat transport for year 12 by (a) the vertical heat flux ΔF_z (W/m^2), with positive values upward, and (b) the meridional heat flux $\Delta F\phi$ (10^4 W/m^2), with positive values northward. Negative values are shaded.

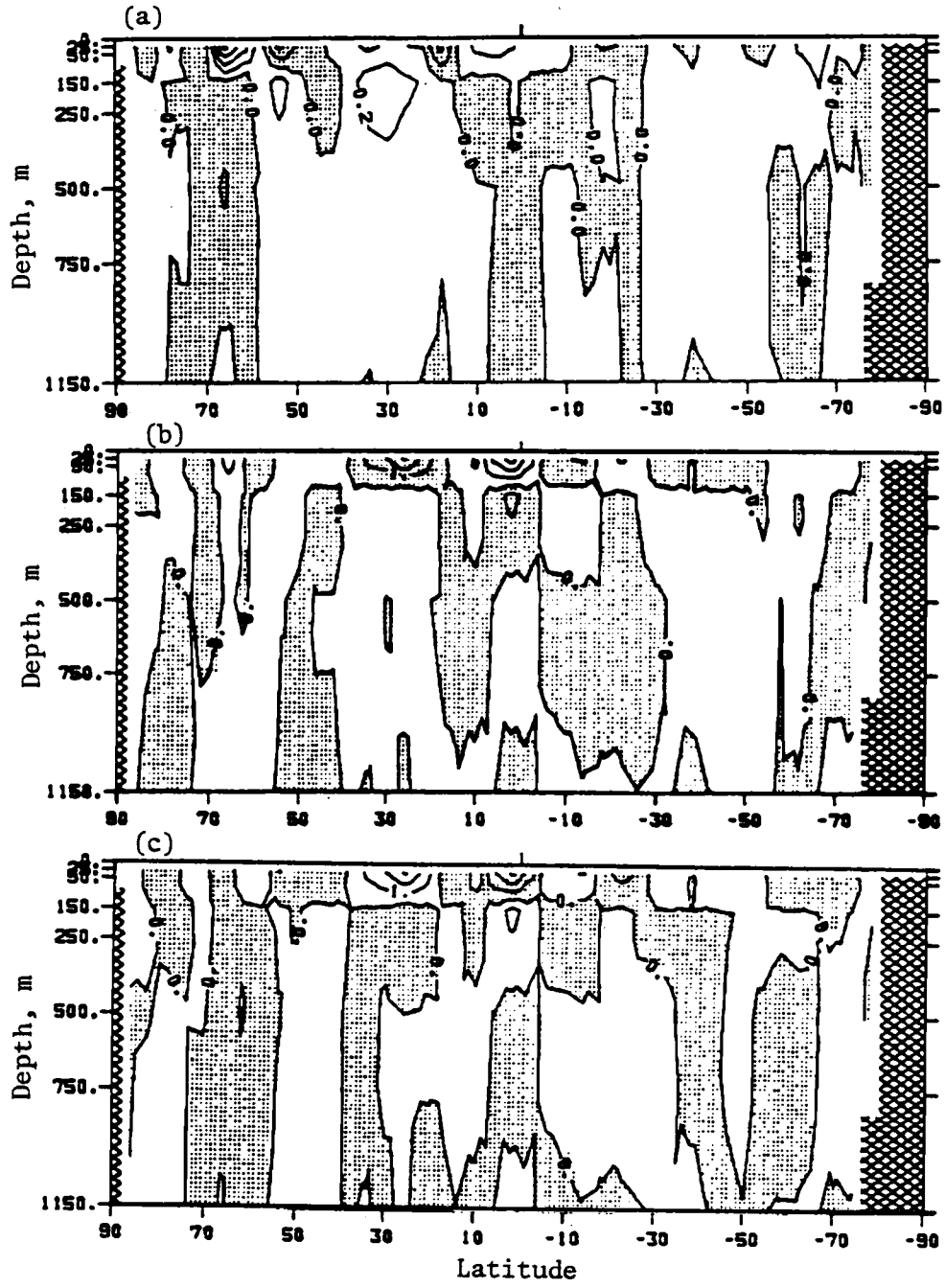

Fig. 4.13. Latitude-depth distributions of the zonal mean temperature change (°C) for year 12 due to (a) the total heat transport, (b) the vertical heat transport and (c) the meridional heat transport. Negative values are shaded.

2) Changes due to each process

The CO_2-induced heat fluxes by the meridional advection and diffusion, $\Delta\overline{FADVM}^z$ and $\Delta\overline{FDIFM}^z$, are shown in Fig. 4.14. The meridional advection is larger than the meridional diffusion by about an order of magnitude. The largest values of the heat flux due to meridional advection (Fig. 4.14a) are located near the surface in the tropical and subtropical regions. In the tropics the advection tends to transport heat toward the poles in each hemisphere in the upper ocean layer, and towards the equator in the second ocean layer. In the high latitudes the advection tends to transport heat toward the equator in both hemispheres in the first ocean layer.

The heat flux by the meridional diffusion extends to deeper layers than the flux by the meridional advection. Figure 4.14b clearly reflects the CO_2-induced temperature changes shown in Fig. 4.8 for year 12. Equatorward heat flux occurred in the tropics, and poleward heat flux occurred in the midlatitudes. The large heat flux convergences near 65°N, 25°N and 70°S correspond to the large temperature change shown in Fig. 4.8 for year 12. Figure 4.14b also shows that the warming penetrated to 2150 m near 65°N by year 12.

The meridional heat transports shown in Fig. 4.14 indicate that the meridional advection is a dominant feature in the meridional heat transport process in the upper layer. However, meridional diffusion is not negligible in the deep layers.

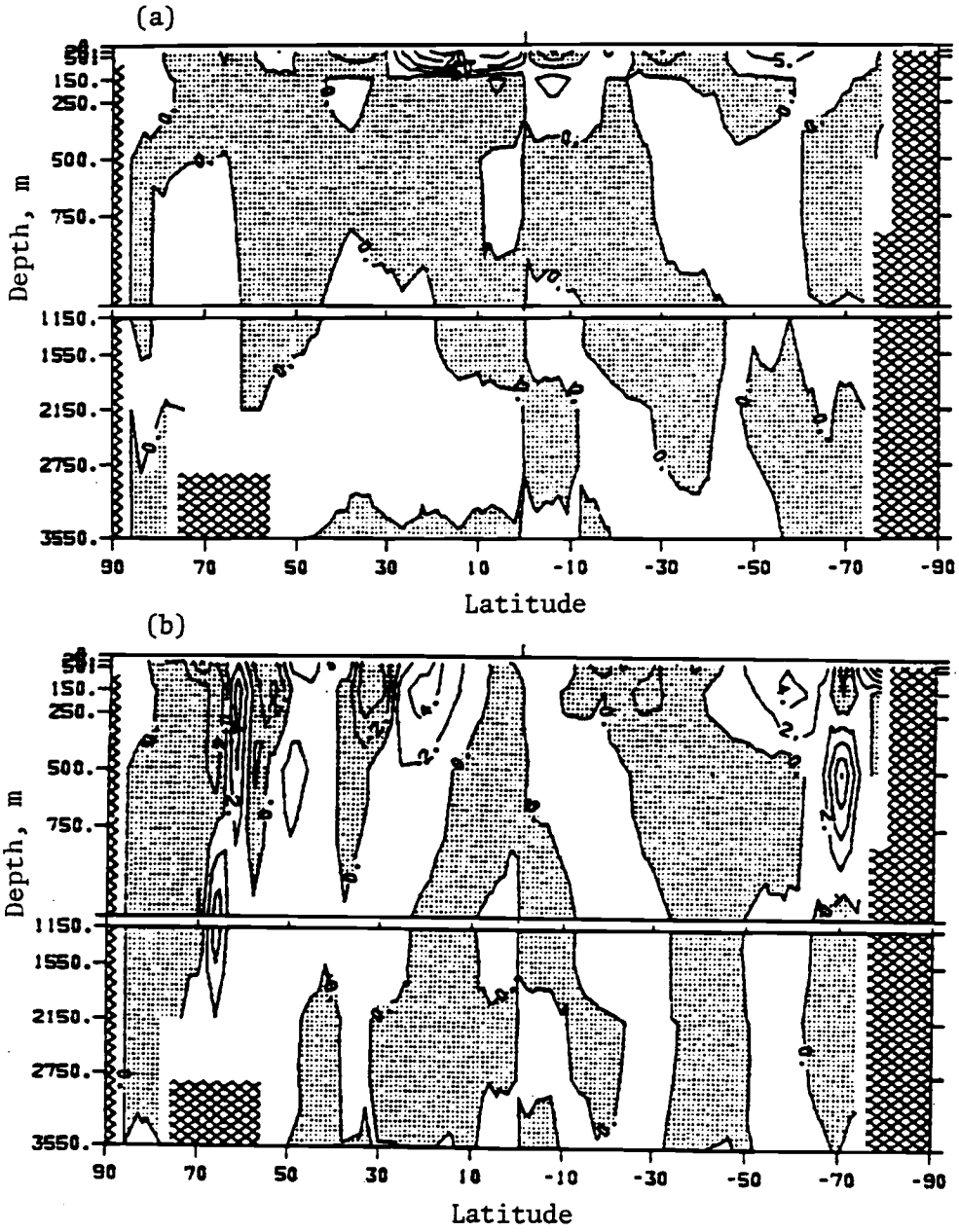

Fig. 4.14. Latitude-depth distributions of the annual zonal mean CO_2-induced heat fluxes for year 12 by (a) the meridional advection $\Delta\overline{FADVM}^z$ (10^4 W/m^2), and (b) the meridional diffusion, $\Delta\overline{FDIFM}^z$ (10^3 W/m^2). Positive values are northward heat fluxes and negative values are shaded.

The heat fluxes due to vertical advection, diffusion and convection, $\Delta\overline{FADVV}^z$, $\Delta\overline{FDIFV}^z$ and $\Delta\overline{FCONV}^z$, respectively, are shown in Fig. 4.15. The vertical advection (Fig. 4.15a) tends to move heat downward in the middle and high latitudes. In the tropical upper layers the advection transports heat upwards; this may be the result of the intensifying upwelling when the CO_2 concentration of the atmosphere is doubled. There are large downward and upward vertical advective heat fluxes near 70°N and 55°N, respectively, which correspond to the strong vertical motion (Fig. 3.11) and the large CO_2-induced temperature change (Fig. 4.8) in that region.

Since the CO_2-induced temperature changes generally decrease with depth (except for the two warm cores near 70°N and 65°S at 500 m; Fig. 4.8), vertical diffusion (Fig. 4.15b) transports heat into the deep ocean. The two areas of upward vertical diffusion of heat near 70°N and 65°S at 500 m correspond to the two warm cores shown in Fig. 4.8 for year 12. The heat flux by vertical diffusion penetrates much deeper near 30°N than elsewhere due to the maximum CO_2-induced temperature change there (Fig. 4.8).

The zonal mean convection processes (Fig. 4.15c) are much stronger in the Northern Hemisphere than in the Southern Hemisphere. Convection transports the CO_2-induced heating downward near 60°N, 30°N and 70°S. In both the $1xCO_2$ and $2xCO_2$ simulations, convection transports heat upward toward the oceanic surface since, in general, the temperature increases downward where the convection occurred (Fig. 3.17). However, for the $2xCO_2-1xCO_2$ difference the convective heat transport can be either upward or downward. Figure

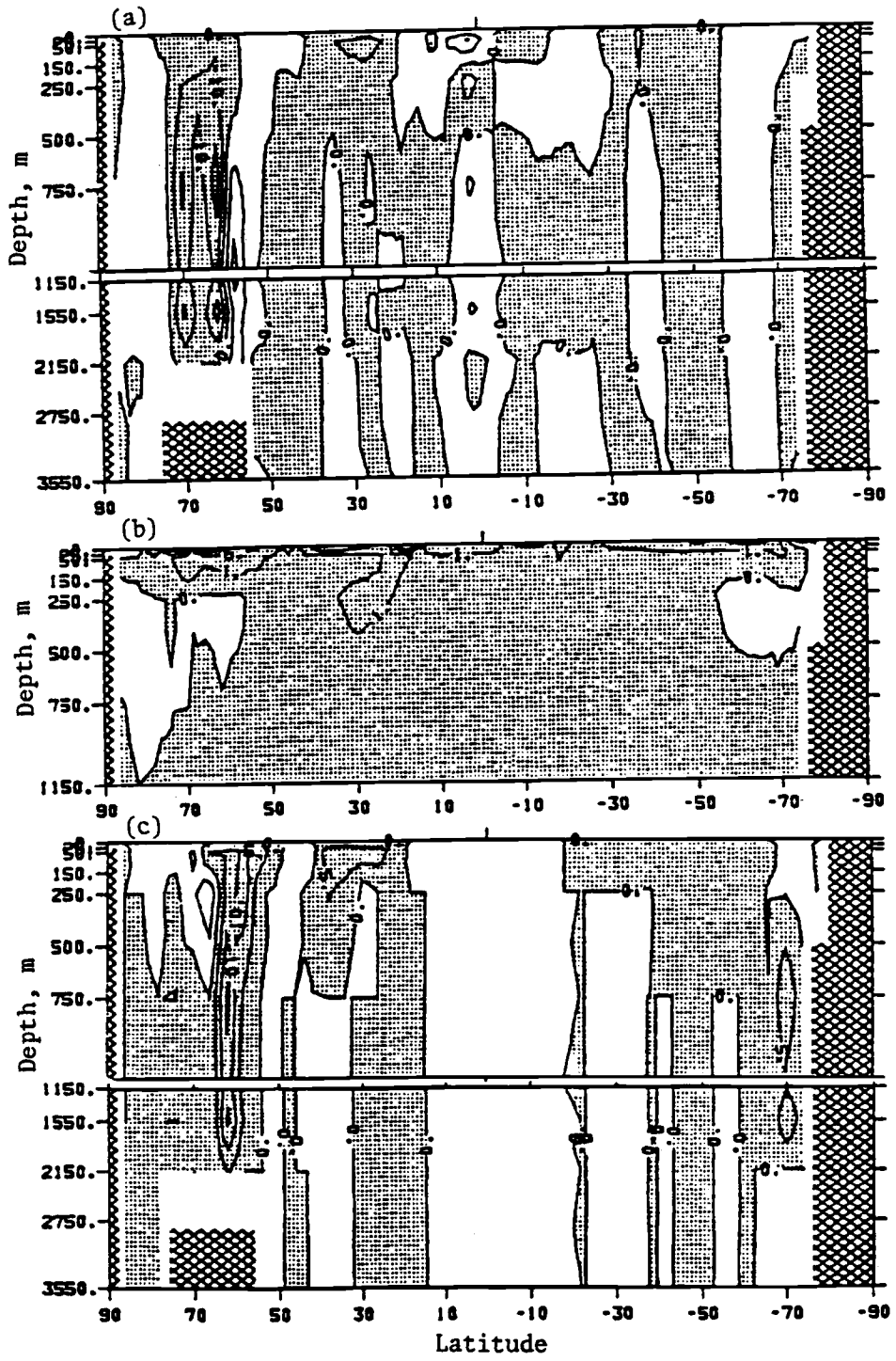

Fig. 4.15. Latitude-depth distributions of the annual zonal mean CO_2-induced heat fluxes for year 12 by (a) vertical advection $\Delta\overline{FADVV}^z$ (W/m^2), (b) vertical diffusion $\Delta\overline{FDIFV}^z$ (W/m^2) and (c) vertical convection $\Delta\overline{FCONV}^z$ (W/m^2). Positive values are upward heat fluxes and negative values are shaded.

4.15c shows that a large downward convective heat flux occurred in high latitudes. This implies that the convection decreased when the CO_2 concentration was doubled in agreement with the interpretation from the global mean analysis (Fig. 4.4). The location of the convection process preferentially in the high latitudes is partly due to the seasonal changes of the ocean surface temperature. During the winter the water in the upper layer can be cooled such that an unstable density stratification begins to occur which is then ameloriated by convective overturning. The decrease of the convection process implies that the ocean becomes more stable after the CO_2 doubling.

Figure 4.16 shows the contributions to the temperature change by the meridional advection and diffusion, $\Delta\overline{\overline{TADVM}}^{z}$ and $\Delta\overline{\overline{TDIFM}}^{z}$, for the annual zonal average of year 12. The temperature changes due to the meridional advection are about an order of magnitude larger than those due to the meridional diffusion, particularly in the upper ocean layer. The tropics are cooled and the subtropics are warmed by the meridional advection in the upper layer. For the meridional diffusion, the largest changes occur at 65°N and 500 m which corresponds the large convergence and divergence of the meridional diffusive heat flux in that area. It is seen that the meridional diffusion tends to decrease the intensity of the warm cores shown in Fig. 4.8 which were built by other physical processes. For the remainder of the ocean the temperature change due to the meridional diffusion is relatively small.

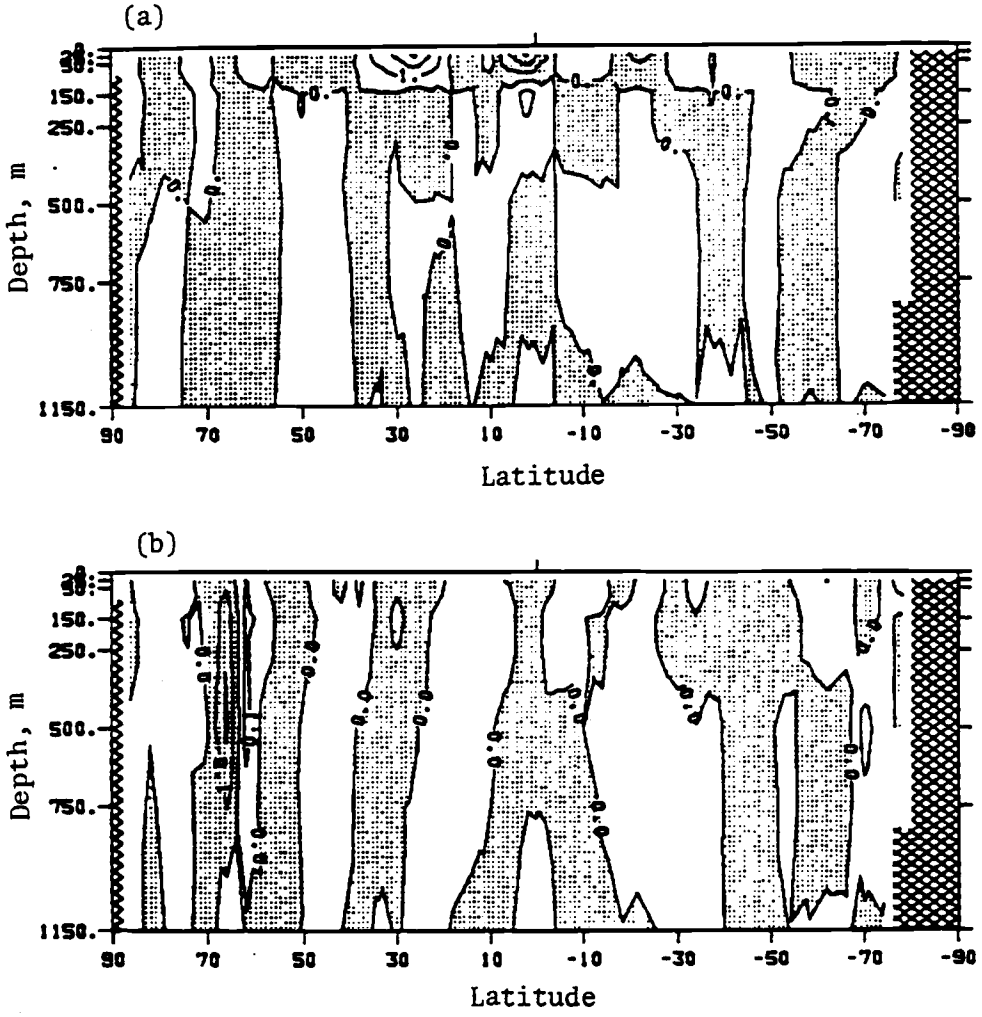

Fig. 4.16. Latitude-depth distributions of the zonal mean temperature change (°C) for year 12 due to the heat fluxes by (a) meridional advection $\Delta\overline{TADVM}^{z}$, and (b) meridional diffusion $\Delta\overline{TDIFM}^{z}$. Negative values are shaded.

The temperature changes due to the vertical advection, vertical diffusion and convection, $\Delta\overline{TADVV}^z$, $\Delta\overline{TDIFV}^z$ and $\Delta\overline{TCONV}^z$, respectively, are shown in Fig. 4.17. It can be seen that large temperature changes due to vertical advection occur in the tropics and midlatitudes in the upper layer. Interestingly, the temperature changes due to the vertical advection have opposite signs in the upper two ocean layers. The temperature change in the upper layers due to the vertical diffusion (Fig. 4.17b) is positive everywhere except in the subtropics and high latitudes. Large changes occurred in the upper layer near 60°N, 30°N and 60°S. The temperature change due to the convection (Fig. 4.17c) shows that cooling occurred near 60°N, 30°N and 50°S in the upper ocean layer, with a corresponding warming in the second layer.

Figures 4.16 and 4.17 show that the temperature change due to vertical advection (Fig. 4.17a) is largely compensated by the temperature change due to the meridional advection (Fig. 4.16a). The vertical diffusion and convection (Fig. 4.17b,c) play important roles in the vertical heat transport, especially in high latitudes. The vertical diffusion tends to warm the upper ocean, while the convection tends to cool the upper ocean and warm the ocean below.

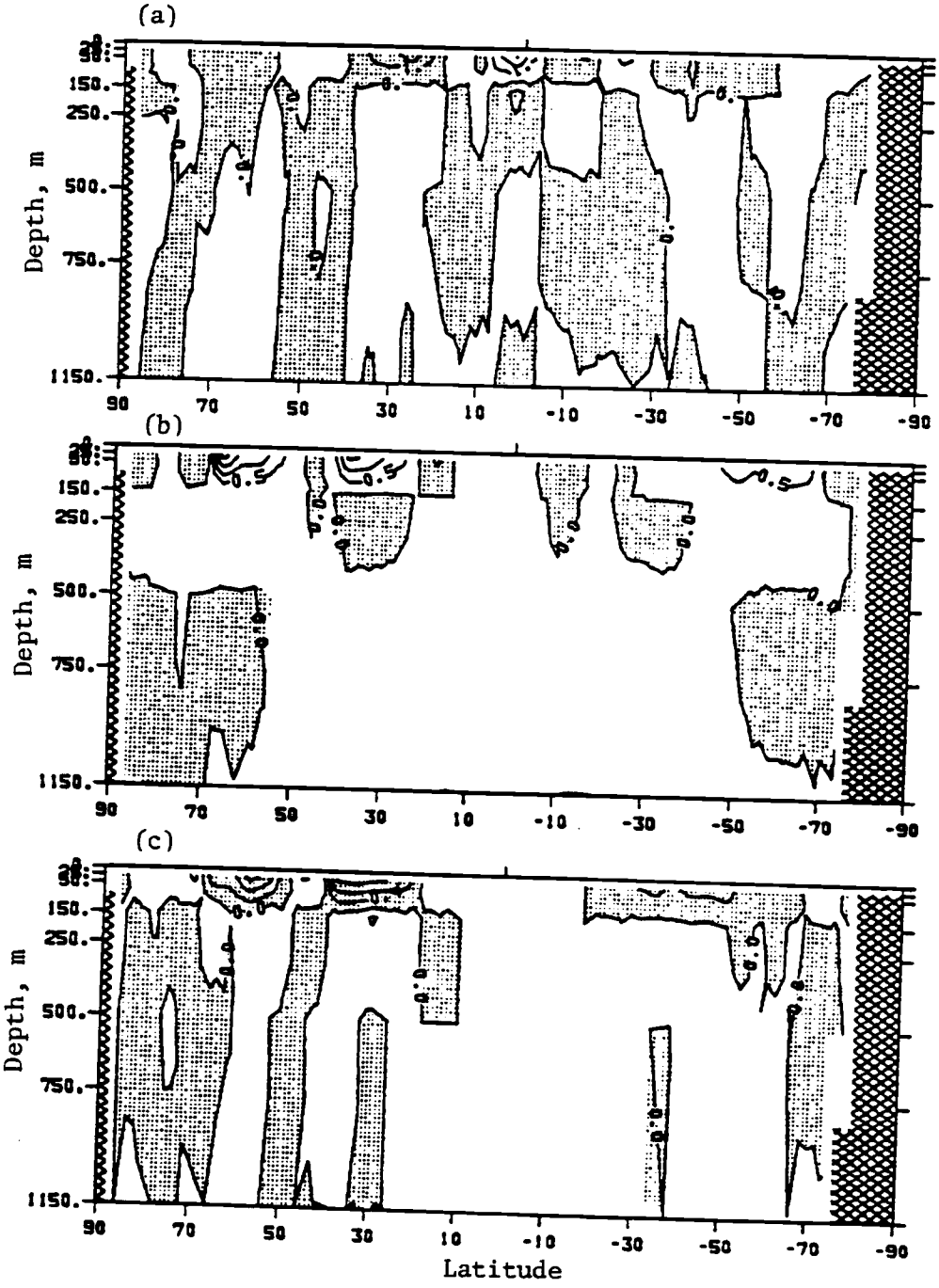

Fig. 4.17. Latitude-depth distributions of the zonal mean temperature change (°C) for year 12 due to the heat fluxes by (a) vertical advection $\Delta\overline{TADVV}^{Z}$, (b) vertical diffusion $\Delta\overline{TDIFV}^{Z}$, and vertical convection, $\Delta\overline{TCONV}^{Z}$. Negative values are shaded.

5. DISCUSSION

The principal objective of the present study was to answer the question: By what pathways and through which physical processes does the simulated ocean general circulation produce the penetration of the CO_2-induced warming into the ocean? The secondary objective was to evaluate the performance of the OGCM in the $1xCO_2$ simulation with the coupled atmosphere/ocean GCM (CGCM). In this chapter we summarize, synthesize and discuss the results of this study.

5.1. Evaluation of the OGCM Performance

The $1xCO_2$ simulation by the CGCM was analyzed by Gates et al. (1985) and Han et al. (1985) who found that there were distinct errors in the simulated sea surface temperature (SST) and sea ice. Furthermore, these errors were found to be largely due to the AGCM. In the present study we have performed a similar analysis of the OGCM performance. In particular, we have restricted attention to the zonal average oceanic fields for which there are observations (Levitus, 1982), namely, potential temperature, salinity and potential density.

The comparison of these simulated and observed fields shows that although they are basically similar, each of the CGCM-simulated fields has distinct errors. There are two possible sources of these errors: 1) the coupling of the AGCM with the OGCM, as in the case of the SST errors, and 2) the OGCM itself. In order to

determine which of these two possibilities was responsible, we looked at the time evolution of the errors in the zonal mean fields. This analysis showed, in fact, that the errors were predominantly generated by the OGCM during its spin-up integration before it was coupled to the AGCM. The spin-up phase had two parts, one with prescribed annual-mean atmospheric boundary conditions, and the other with the corresponding prescribed annual cycle. It was found that the errors in the oceanic zonal means already existed at the end of the OGCM simulation with the annual mean atmospheric boundary conditions.

Before coupling with the AGCM, the OGCM was tested and evaluated, in part, by its ability to simulate the observed SST. However, because the surface air temperature was prescribed as a boundary condition for the OGCM, along with the heat transfer coefficient, it is difficult for the simulated SST to be very different from the prescribed surface air temperature and, therefore, from the observed SST. Such an evaluation for the OGCM is equivalent to evaluating the AGCM by comparing the simulated surface air temperature over the ocean with the observed surface air temperature. Here because the SST is prescribed as a boundary condition for the AGCM, along with the heat transfer coefficient, the simulated surface air temperature cannot be very different from the SST and, therefore, from the observed surface air temperature. In fact, such a comparison shows that the AGCM performs very well. However, when the simulated surface air temperature over land is compared with the observed surface air temperature, the errors of

the AGCM are revealed. The present study shows that it is not sufficient to compare the simulated SST with the observed SST to evaluate the performance of the OGCM. It is also necessary to compare the simulated internal oceanic quantities with the corresponding observed quantities. Such a comparison, like that for the AGCM, reveals the errors of the OGCM. Analysis of the causes of these errors can then be used to improve the performance of the model.

5.2. Pathways and Processes of the CO_2-induced Oceanic Heating

The global mean analysis of the CO_2-induced climate changes shows the ocean gains heat at a rate of about 3 W/m^2 due to the doubling of the CO_2 concentration. This corresponds to a warming of the entire ocean of about 0.005°C/year, a relatively small warming as a result of the ocean's large heat capacity. However, the global mean CO_2-induced warming begins at the top of the ocean and gradually penetrates into the interior of the ocean. At the end of year 20 the warming is about 1.2°C in the 0-50 m layer, 0.9°C in the 50-250 m layer, 0.5°C in the 250-750 m layer, 0.1°C in 750-1550 m layer, and is virtually zero below 1550 m. Thus, there is a net downward heat flux in the global ocean when the CO_2 concentration is doubled. This downward heat flux is predominantly due to the convection process.

The global mean heat transport results of this study have been compared with the results obtained by Bryan and Spelman (1985) with the non-global, annual-mean version of the GFDL coupled GCM. The

GFDL $1xCO_2$ simulation did reach equilibrium while the GFDL $4xCO_2$ simulation and the OSU $1xCO_2$ and $2xCO_2$ simulations did not. However, the results of the OSU and GFDL coupled models show many similarities. In particular, the CO_2-induced heat flux is downward in the ocean, the convective heat flux is dominant in the downward heat transport, and there is even quantitative agreement considering the OSU simulation is for a doubling of CO_2 and the GFDL simulation is for a quadrupling of CO_2. Thus it appears that the issue of the control's equilibrium is not of paramount importance in terms of the CO_2-induced vertical heat flux.

The time evolution of the annual zonal-mean CO_2-induced temperature changes simulated by the OSU model shows that the oceanic surface warming increases from the tropics toward the mid-latitudes of both hemispheres and penetrates gradually to the deep ocean. The oceanic warming penetrates to a greater depth in the subtropics and midlatitudes than in the equatorial region. The latitudinal distributions of the $2xCO_2$-$1xCO_2$ temperature changes simulated by the coupled GCM are very similar to the latitudinal distribution of the excess ^{14}C over the pre-nuclear value that has been observed in the ocean (Broecker et al., 1980).

In addition to the global mean heat budget analysis, we performed an analysis of the CO_2-induced changes in the zonal mean heat budget. Here we synthesize the results of that analysis. Our analysis of the zonal mean heat budget shows that the CO_2-induced warming of the ocean occurs predominantly through the downward transport of heat, with the meridional heat flux being only of

secondary importance. Figure 5.1 shows a schematic diagram of how the CO_2-induced heat penetrates into and through the ocean.

At the ocean's surface the CO_2-induced heating is everywhere into the ocean, but it is not uniform in latitude. The largest surface heating occurred near 60°N, 35°N, 0°, 40°S and 60°S (Fig. 4.7). The penetration of the surface heating is a minimum in the tropics and a maximum in the subpolar latitudes of both hemispheres. In the tropics the heat penetration is minimized by the upwelling of cold water. Part of the CO_2-induced heating of the tropical ocean is transported poleward by the poleward branches of the meridional circulation cells which exist there in association with the upwelling through the conservation of mass.

In the subtropics the CO_2-induced heating is transported downward by the existing downwelling there. These subtropical regions are the locations of the subtropical gyres which are anticyclonic horizontal ocean circulations that are driven by the westerly winds in the midlatitudes of both hemispheres and the equatorial easterly winds. Due to friction in the ocean's surface boundary layer, water is caused to flow horizontally into the gyres (the Ekman transport process) and downwelling occurs there by the conservation of mass. It is likely that this gyral downwelling transports the CO_2-induced surface heating into the subtropical oceans where it combines with the poleward heat flux from the equatorial region.

In the high latitudes of both hemispheres the CO_2-induced surface heating penetrates much deeper than elsewhere. In these regions the suppressed convection plays a very important role in

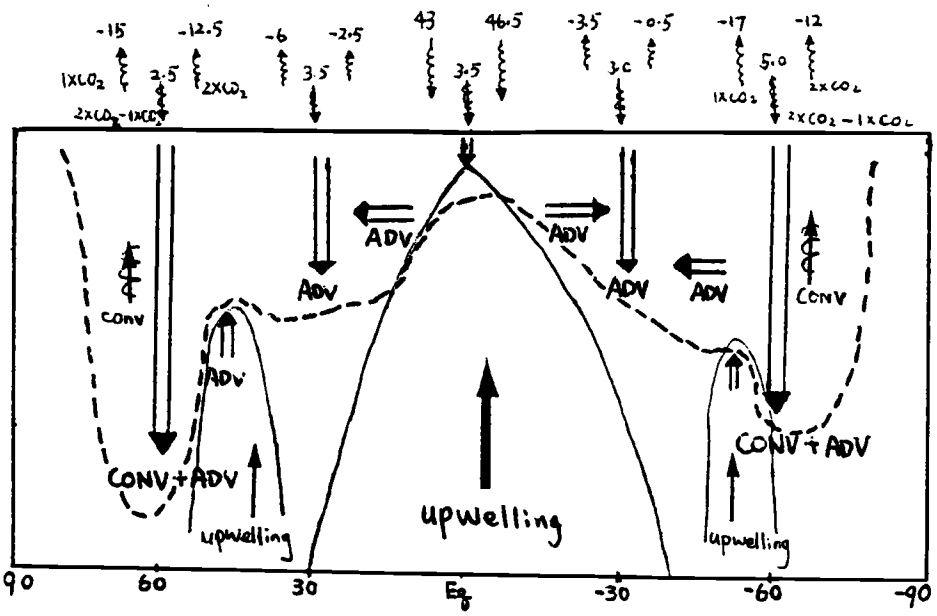

Fig. 5.1. Schematic digram of the pathway of the CO_2-induced heating. Open and solid arrows represent the heat fluxes and the currents, and the solid and dashed lines represent the regions of upwelling and the CO_2-induced temperature change profile.

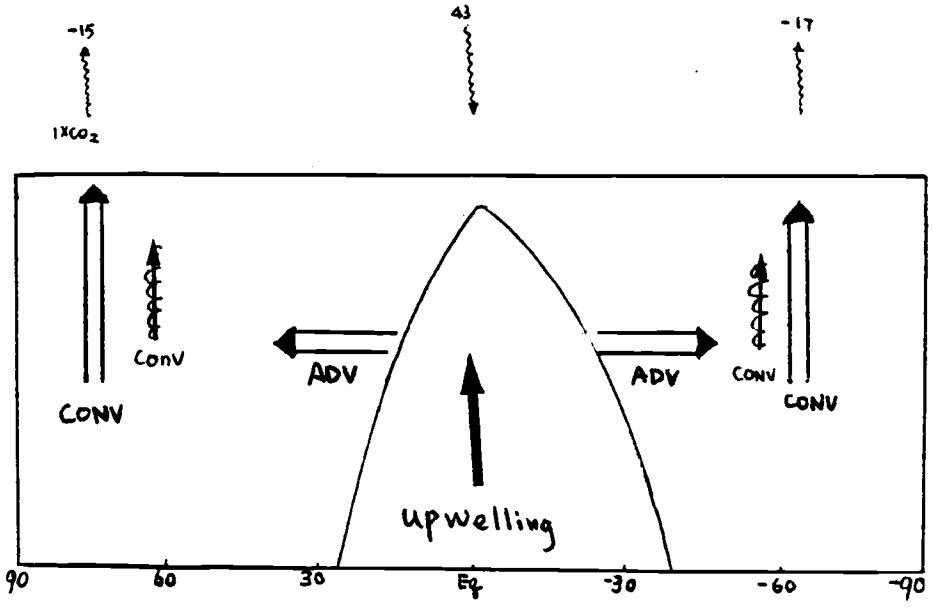

Fig. 5.2. Schematic digram of the heat transports for the normal ($1XCO_2$) case. The arrows and the solid lines have the same meaning as in Fig. 5.1.

the penetration of the CO_2-induced heating. Figure 5.2 shows that in the normal $1xCO_2$ case, the ocean gains heat from the atmosphere in the tropics and loses heat to the atmosphere in high latitudes. The heat gained by the ocean in the tropics is transported poleward and then upward, mostly through the convection process, to balance the surface cooling in high latitudes. However, when the CO_2 concentration is increased, the warming of the ocean surface at high latitudes stabilizes the oceanic stratification and reduces the intensity of the convective overturning. This reduces the ability of the ocean to lose heat to the atmosphere in high latitudes which results in a net uptake of the CO_2-induced surface heating by the global ocean.

The present study has focused on understanding the penetration of the CO_2-induced heating into and through the ocean in terms of the global- and zonal-averages. However, it remains to investigate and understand the full geographic characteristics of the CO_2-induced heating, such as the relative contribution by each ocean and by the zonally-asymmetric features of the oceans such as the gyres, boundary currents and regionalized convection centers. Such an investigation requires a detailed three-dimensional heat budget analysis. We intend to conduct such an analysis as a sequel to this study.

5.3. The Relative Penetration of Passive Tracers and CO_2-induced Heating

The transient response of the climate system to an abrupt CO_2 increase has been investigated with planetary energy balance, radiative-convective and general circulation models. These studies have obtained estimates of the e-folding time, τ_e, that range from 10 to 100 years. The factors that cause the wide range in τ_e have been discussed by Wigley and Schlesinger (1985) from their analytical solution for an energy balance climate/box-diffusion ocean model. They concluded that to determine the value of τ_e requires a coupled global atmosphere/ocean GCM. By using such a model, Schlesinger et al. (1985) obtained τ_e of about 50-75 years. However, it is essential to test this finding with observations.

Since we cannot observe the penetration of heat into and through the ocean, it has been proposed to use an observable surrogate such as the penetration of a passive tracer. However, different studies have given different answers regarding the relative penetration speed of heat and a passive tracer. Kellogg (1983) speculated that a CO_2-induced heating would penetrate into the ocean more slowly than a passive tracer due to the reduction in the ocean's vertical convection as a result of the heating. This speculation is not correct because convection occurs only in the high latitudes, as shown above and by Bryan and Spelman (1985), not everywhere in the global ocean as Kellogg implicitly assumed. Schlesinger et al. (1985) showed that the heating induced by a CO_2

doubling penetrated as fast as a passive tracer, while Bryan and Spelman (1985) showed that the heating induced by a CO_2 quadrupling penetrated about twice as fast as a passive tracer. In both cases the penetration of the CO_2-induced heating occurs predominantly through the reduction in the high-latitude convective overturning. The study by Bryan and Spelman (1985) indicates that the passive tracer data are not indicative of the vertical penetration of a large heat anomaly into the ocean. But is the penetration rate of a passive tracer indicative of the penetration rate of heat for a smaller heat anomaly such as that due to the actual increase of CO_2?

The results of Schlesinger et al. (1985) showed that the penetration of heat and a passive tracer are the same in terms of the global mean. However, in this study we have shown that the heat penetration modifies the convection in the high latitude, while by definition a passive tracer cannot change the convection. Thus, even though the global means are the same, there must be latitudinal differences between the penetration of heat and a passive tracer. How large are these latitudinal differences? If they are small, then the past and planned future measurements of the penetration rate of passive tracers can be used as a surrogate for the penetration of the CO_2-induced heating, and the passive tracer observations can then be used to test the model predictions of the characteristic response time of the climate system to increasing CO_2 concentration. To address this issue we can use the CGCM to simulate the penetration of a passive tracer and compare the

results with those from the present study for the penetration of CO_2-induced heating. Such a passive tracer/CO_2-induced heating comparison study is planned as a continuation of the current research.

REFERENCES

Alexander, R.C., and R.L. Mobley, 1976: Monthly averaged sea surface temperature and ice-pack limits on a 1° global grid. Mon. Wea. Rev., 104, 143-148.

Broecker, W.S., and T.-H. Peng, 1982: Tracer in the sea. Lamont-Doherty Geological Observatory, Columbia University, Palisades, New York, 690 pp.

Broecker, W.S., T.-H. Peng and R. Engh, 1980: Modeling the carbon system. Radiocarbon, 22, 565-598.

Bryan, K., and M.J. Spelman, 1985: The ocean's response to a CO_2-induced warming. J. Geophys. Res., 90, 11679-11688.

Bryan, K., F.G. Komro and C. Rooth, 1984: The ocean's transient response to global surface temperature anomalies. In Climate Processes and Climate Sensitivity, Maurice Ewing Series, 5, J.E. Hansen and T. Takahashi, Eds., American Geophysical Union, Washington, D.C., 29-38.

Bryan, K., F.G. Komro, S. Manabe and M.J. Spelman, 1982: Transient climate response to increasing atmospheric carbon dioxide. Science, 215, 56-58.

Bryden, H.L., 1973: New polynomials for thermal expansion, adiabatic temperature gradient and potential temperature of sea water. Deep-sea Res., 20, 401-408.

Elliott, W.P., L. Machta and C.D. Keeling, 1985: An estimate of the biotic contribution to the atmospheric CO_2 increase based on direct measurements at Mauna Loa Observatory. J. Geophys. Res., 90, 3741-3746.

Eckart, C., 1958: Properties of water. Part II. Amer. J. Sci., 256, 225-240.

Esbensen, S.K., and Y. Kushnir, 1981: The heat budget of the global ocean: An atlas based on estimates from surface marine observations. Report No. 29, Climatic Research Institute, Oregon State University, Corvallis, OR, 27 pp.

Gates, W.L., 1976a: Modeling the ice-age climate. Science, 191, 1138-1144.

Gates, W.L., 1976b: The numerical simulation of ice-age climate with a global general circulation model. J. Atmos. Sci., 33, 1844-1873.

Gates, W.L., Y.-J. Han and M.E. Schlesinger, 1985: The global climate simulated by a coupled atmosphere-ocean general circulation model: Preliminary results. In Coupled Ocean-Atmosphere Models, J.C.J. Nihoul, Ed., Elsevier, Amsterdam, 131-151.

Ghan, S.J., J.W. Lingaas, M.E. Schlesinger, R.L. Mobley and W.L. Gates, 1982: A documentation of the OSU two-level atmospheric general circulation model. Report No. 35, Climatic Research Institute, Oregon State University, Corvallis, OR, 395 pp.

Gordon, A.L., 1975a: Review of present knowledge of the ocean circulation: General ocean circulation. In Numerical Model of Ocean Circulation. National Academy of Sciences, Washington, D. C., 39-53.

Gordon, A.L., 1975b: Review of present knowledge of the ocean circulation: Heat and salt balance within the cold waters of the world ocean. In Numerical Models of Ocean Circulation. National Academy of Sciences, Washington, D. C., 54-56.

Han, Y.-J., 1984a: A numerical world ocean general circulation model. Part I. Basic design and barotropic experiment. Dyn. Atmos. Oceans, 8, 107-140.

Han, Y.-J., 1984b: A numerical world ocean general circulation model. Part II. A baroclinic experiment. Dyn. Atmos. Oceans, 8, 141-172.

Han, Y.-J., M.E. Schlesinger and W.L. Gates, 1985: A analysis of the air-sea-ice interaction simulated by the OSU coupled atmosphere-ocean general circulation model. In Coupled Ocean-Atmosphere Models, J.C.J. Nihoul, Ed., Elsevier, Amsterdam, 167-182.

Hansen, J., A. Lacis, D. Rind, G. Russell, P. Stone, I. Fung, R. Ruedy and J. Lerner, 1984: Climate sensitivity: Analysis of feedback mechanisms. In Climate Processes and Climate Sensitivity, Maurice Ewing Series, 5, J.E. Hansen and T. Takahashi, Eds., American Geophysical Union, Washington, D.C., 130-163.

Hoffert, M.I., A.J. Callegari and C.-T. Hsieh, 1980: The role of deep sea heat storage in the secular response to climate forcing. J. Geophys. Res., 85, 6667-6679.

Kellogg, W.W., 1983: Feedback mechanisms in the climate system affecting future levels of carbon dioxide. J. Geophys. Res., 88, 1263-1269.

Kellogg, W.W., and R. Schware, 1982: Society, science and climate change. Foreign Affairs, 1076-1109.

Jones, P.D., T.M.L. Wigley and P.B. Wright, 1986: Global mean temperature, 1861-1984. (In press).

Levitus, S., 1982: Climatological Atlas of the World Ocean, NOAA Professional Paper No. 13, U.S. Government Printing Office, Washington, D.C., 173pp.

Manabe, S., 1969: Climate and the ocean circulation. I. The atmospheric circulation and the hydrology of the earth's surface. Mon. Wea. Rev., 97, 739-774.

Manabe, S., and A.J. Broccoli, 1984: Influence of the CLIMAP ice sheet on the climate of a general circulation model: Implications for the Milankovitch theory. In Milankovitch and Climate, Part 2, Edited by A. Berger et al., D. Reidel Pub., Dordrecht, Netherlands, pp. 789-800.

Manabe, S., and A.J. Broccoli, 1985a: A comparison of climate model sensitivity with data from the last glacial maximum. J. Atmos. Sci., 42, 2643-2651.

Manabe, S., and A.J. Broccoli, 1985b: The influence of continental ice sheets on the climate of an ice age. J. Geophys. Res., 90, 2167-2190.

Manabe, S., and D.G. Hahn, 1977: Simulation of the tropical climate of an ice age. J. Geophys. Res., 82, 3889-3911.

Manabe, S., and D.G. Hahn, 1981: Simulation of atmospheric variability. Mon. Wea. Rev., 109, 2260-2286.

Manabe, S., and R.T. Wetherald, 1975: The effects of doubling the CO_2 concentration on the climate of general circulation model. J. Atmos. Sci., 32, 3-15.

Manabe, S., and R.T. Wetherald, 1980: On the distribution of climate change resulting from an increase in CO_2-content of the atmosphere. J. Atmos. Sci., 37, 99-118.

Manabe, S., K. Bryan and M.J. Spelman, 1979: A global ocean-atmosphere climate model with seasonal variation for future studies of climate sensitivity. Dyn. Atmos. Oceans, 3, 393-426.

Nordhaus, W.D., and G.W. Yohe, 1983: Future paths of energy and carbon dioxide emissions. In Changing Climate, National Academy of Sciences, Washington, D.C., 87-153.

Oeschger, H., H. Siegenthaler, U. Schotterer and A. Gugelman, 1975: A box diffusion model to study the carbon dioxide exchange in nature. Tellus, 27, 168-192.

Parkinson, C.L., and W.M. Washington, 1979: A large-scale numerical model of sea ice. J. Geophys. Res., 84, 311-337.

Reid, J.L., 1981: On the mid-depth circulation of the world ocean. In Evolution of Physical Oceanography, Scientific Surveys in Honor of Henry Stommel, B.A. Warren and C. Wunch Eds., The M.I.T. Press, Cambridge, pp. 70-111.

Rooth, C.G., and H.G. Ostlund, 1972: Penetration of tritium into the Atlantic thermocline. Deep Sea Res., 19, 481-492.

Rotty, R.M., 1983: Distribution of and changes in industrial carbon dioxide production. J. Geophys. Res., 88, 1301-1308.

Sarmiento, J.L., 1983a: A tritium box model of the North Atlantic thermocline. J. Phys. Oceanogr., 13, 1269-1294.

Sarmiento, J.L., 1983b: A simulation of bomb tritium entry into the Atlantic Ocean. J. Phys. Oceanogr., 13, 1924-1939.

Schlesinger, M.E., 1985: Equilibrium and transient climatic effects of increased atmospheric CO_2. Report No. 67, Climatic Research Institute, Oregon State University, Corvallis, OR, 41pp.

Schlesinger, M.E., and W.L. Gates, 1980: The January and July performance of the OSU two-level atmospheric general circulation model. J. Atmos. Sci., 37, 1914-1943.

Schlesinger, M.E., and W.L. Gates, 1981: Preliminary analysis of the mean annual cycle and inter annual cycle variability simulated by the OSU two-level atmospheric general circulation model. Climatic Research Institute, Oregon State University, Report No. 23, 47pp.

Schlesinger, M.E., and J.F.B. Mitchell, 1985: Model projections of equilibrium climate response to increased CO_2. In The Potential Climatic Effects of Increasing Carbon Dioxide, M.C. MacCracken and F.M. Luther, Eds., DOE/ER-0237, U.S. Department of Energy, Washinton, D.C., 81-147.

Schlesinger, M.E., W.L. Gates and Y.-J. Han, 1985: The role of the ocean in CO_2-induced climate warming: Preliminary results from the OSU coupled atmosphere-ocean GCM. In Coupled Ocean-Atmosphere Models, J.C.J. Nihoul, Ed., Elsevier, Amsterdam, 447-478.

Semtner, A.J., 1976: A model for the thermodynamic growth of sea ice in numerical investigations of climate. J. Phys. Oceanogr., 6, 379-389.

Shukla, J., D. Straus, D. Randall, Y. Sud and L. Marx, 1981: Winter and summer simulations with the GLAS climate model. Technical Memorandum 83866, Laboratory for Atmospheric Sciences Modeling and Simulation Facility, NASA Goddard Space Flight Center, Greenbelt, Maryland, 282pp.

Spelman, M.J. and S. Manabe, 1984: Influence of oceanic heat transport upon the sensitivity of a model clmate. J. Geophys. Res., 89, 571-586.

Stommel, H., 1958: The abyssal circulation. Deep-sea Res., 5, 80-82.

Stommel, H. and A.B. Arons, 1960a: On the abyssal circulation of the world ocean. I. Stationary planetary flow pattern on a sphere. Deep-sea Res., 6, 140-154.

Stommel, H. and A.B. Arons, 1960b: On the abyssal circulation of the world ocean. II. An idealized model of the circulation pattern and amplitude in oceanic basins. Deep-sea Res., 6, 217-233.

Stowe, K.S., 1979: Ocean Science. John Wiley and Sons, Inc., 610 pp.

Veronis, G., 1981: Dynamics of large-scale ocean circulation. In Evolution of Physical Oceanography, Scientific Survey in Honor of Henry Stommel, B.A. Warren and C. Wunch Eds., The M.I.T. Press, Cambridge, 140-183.

Warren, B.A., 1981: Deep circulation of the world ocean. In Evolution of Physical Oceanography, Scientific Surveys in Honor of Henry
Stommel, B.A. Warren and C. Wunch Eds., The M.I.T. Press, Cambridge, 6-41.

Washington, W.M., and G.A. Meehl, 1984: Seasonal cycle experiment on the climate sensitivity due to a doubling of CO_2 with an atmospheric general circulation model coupled to a simple mixed-layer ocean model. J. Geophys. Res., 89, 9475-9503.

Washington, W.M., A.J. Semtner, Jr., G.A. Meehl, D.J. Knight and T.A. Mayer, 1980: A general circulation experiment with a coupled atmosphere, ocean and sea ice model. J. Phys. Oceanogr., 10, 1887-1980.

Wetherald, R.T., and S. Manabe, 1972: Response of the joint ocean-atmosphere model to the seasonal variation of the solar radiation. Mon. Wea. Rev., 100, 42-59.

Wigley, T.M.L., and M.E. Schlesinger, 1985: Analytical solution for the effect of increasing CO_2 on global mean temperature. Nature, 315, 649-652.

WMO, 1983: Report of the WMO (CAS) Meeting of Experts on the CO_2 Concentrations from Pre-Industrial Times to I.G.Y. World Climate Programme, WCP-53, WMO/ICSU, Geneva, 34pp.

Wunch, C., 1984: The ocean circulation in climate. In The Global Climate, J.T. Houghton, Ed., University Press, Cambridge, 189-204.

APPENDICES

APPENDIX A

Correction of the Saved Temperature Change Due to Convection

The equation of the First Law of Thermodynamics can be written as

$$\frac{\partial T}{\partial t} = f(t,T) + Q_{conv}(t,T) \ , \qquad (A.1)$$

where $Q_{conv}(t,T)$ is the heating due to convection and $f(t,T)$ is that due to all other processes. In the OGCM simulation a leapfrog scheme (Fig. A.1) was used to integrate Eq. (A.1), with a forward scheme inserted every 15 time steps. The daily accumulated temperature change due to convection, $(\Delta T_{conv})_{acc}$, was output as history data. The procedure for calculating this accumulated convective heating was

$$(\Delta T_{conv})_{acc} = E_{conv} + O_{conv} \ , \qquad (A.2)$$

where

$$E_{conv} = \sum_{k=1}^{12} (\Delta T_{conv})_{2k} \qquad (A.3)$$

and

$$O_{conv} = \sum_{k=1}^{12} (\Delta T_{conv})_{2k-1} \qquad (A.4)$$

are the accumulations for the even- and odd-numbered time steps, respectively. However, since E_{conv} and O_{conv} individually

represent the 24-hour accumulation, $(\Delta T_{conv})_{acc}$ given by Eq. (A.2) is approximately twice the actual 24-hour accumulation, with the approximation being due to the periodic insertion of the forward integration scheme. Consequently, we correct this error by dividing the saved accumulated temperature change due to convection by 2.

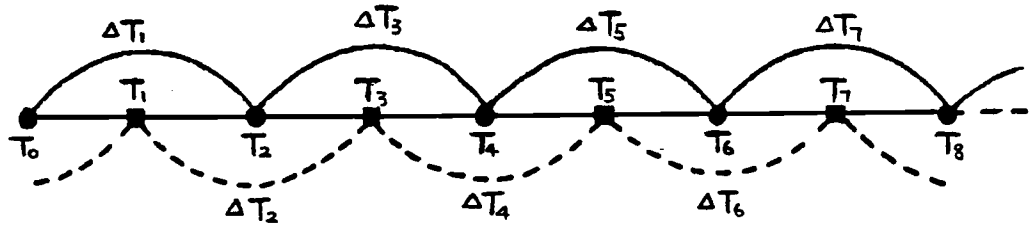

Fig. A.1. Sequence of the time step in the time integration procedure for the temperature change in the CGCM.

APPENDIX B

Reconstruction of the Ocean Surface Heat Flux FTS

As shown by Eqs. (3.16), (4.14) and (4.15), the analysis of the penetration of the CO_2-induced warming into the ocean requires knowledge of the heat flux across the ocean surface, FTS, for both the $1xCO_2$ and $2xCO_2$ simulations. For ice-free ocean, FTS is the same as the air-sea heat flux, BS, and for ice-covered ocean FTS is the ice-sea heat flux. Unfortunately, during the first 12 years of the $1xCO_2$ simulation, the FTS data were saved only for the ice-free ocean. However, using the saved $1xCO_2$ daily accumulated air-sea heat flux, ACBS, and the sea ice thickness, HI, it is possible to reconstruct the missing FTS data for the ice-covered ocean. This reconstruction method, which has been used in the analysis of the CO_2-induced heating presented in the text, is described below.

In the coupled atmosphere/ocean model the heat flux across the ocean surface is

$$FTS = \begin{cases} BS & \text{if no sea ice} \\ \dfrac{\rho c \kappa (T_o - T_{ice})}{\Delta z_1 / 2} & \text{if sea ice .} \end{cases} \qquad (B.1)$$

Here T_{ice} is the temperature of the sea ice at its base (T_{ice} = 1.96°C), T_o is the temperature of the upper layer of the ocean which cannot be less than T_{ice}, ρ is density of the ocean water (ρ = 1.025 g/cm^3), c is the heat capacity of the ocean water (c = 0.96 cal/g/°C), κ is the thermal diffusivity of sea water (κ =

1 cm/s), and z is the thickness of the first oceanic layer (Δz_1 = 50 m).

During the simulations the sea ice thickness, HI, was saved at six-hour intervals and the daily-accumulated air-sea heat flux, ACBS, was saved for each 24-hour period. Using these data and Eq. (B.1) we can approximate the daily accumulated FTS by

$$\text{ACFTS} = \sum_{i=1}^{4} \frac{\rho c \kappa \left(T_o - T_{ice}\right)}{\Delta z_1/2} \delta_i + \frac{1}{4}\left(1 - \delta_i\right)\text{ACBS}, \qquad \text{(B.2)}$$

where

$$\delta_i = \begin{cases} 1 & \text{if sea ice (HI > 0)} \\ 0 & \text{if no sea ice (HI = 0)} , \end{cases}$$

and i = 1, 2, 3, 4 correspond to the simulation hours 0, 6, 12 and 18 GMT, respectivily. In Eq. (B.2) one-quarter of the ACBS data is added to the accumulated FTS for each sampling time when there is no sea ice, and the actual ice-sea heat flux is added each time when there is sea ice. The result of this reconstruction will be exactly correct only when sea ice did not exist during the 24-hour period. If sea ice existed for this entire period the reconstruction can be in error because only four samples are used to estimate the ice-sea heat flux instead of the actual 24 time points. If sea ice existed for only part of the 24-hour period, then the reconstruction can be further in error as a result of selecting the ice-free term instead of the correct ice-covered term, and vice versa.

The reconstruced ACFTS given by Eq. (B.2) was tested for year 13 of both the $1xCO_2$ and $2xCO_2$ simulations during which the actual FTS data were saved. It was found that the reconstruction method performed very well for those tests except in certain regions where sampling errors were involved. Figure B.1 shows the actual zonal mean FTS, the zonal mean of the reconstructed FTS, and their difference averaged for year 13 of the $1xCO_2$ simulation. It can be seen that the magnitude of the error is relative small and the errors occurred near the active ice melting and freezing areas. These errors were mostly caused by the formation or melting of sea ice within the six-hour periods.

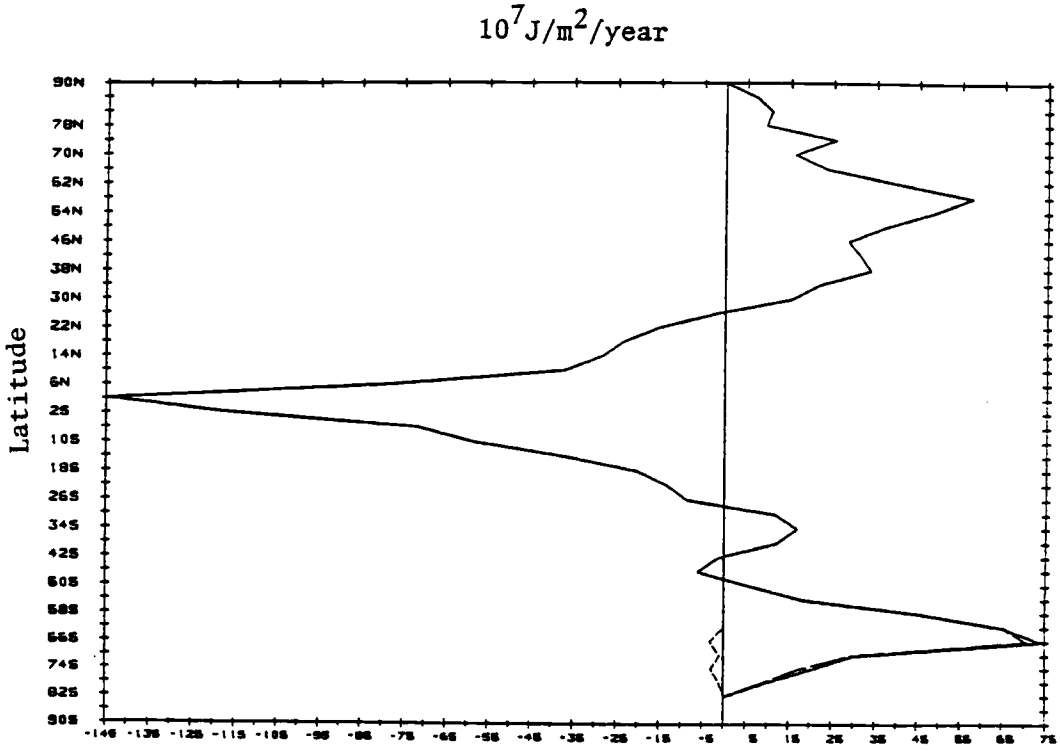

Fig. B.1. Comparison of the annual zonal mean FTS as reconstructed by Eq. (B.2) (dashed line) and as actually simulated (solid line) for year 13 of the CGCM control run, together with their difference (dotted line).

APPENDIX C

Numerical Solution of the Poisson Equation with Neumann Boundary Conditions

In Chapter 4 we obtained Eq. (4.28) for the zonally and time integrated $2xCO_2-1xCO_2$ temperature difference ΔT, that is,

$$\rho c \Delta T = \frac{1}{a\cos\phi} \frac{\partial}{\partial \phi} (\cos\phi \Delta F_{D,\phi}) + \frac{\partial \Delta F_{D,Z}}{\partial z} \quad . \tag{C.1}$$

This equation can be written in terms of a potential Φ as in Eq. (4.29),

$$\rho c \Delta T = \frac{1}{a\cos\phi} \frac{\partial}{\partial \phi} \left(\cos\phi \frac{1}{a} \frac{\partial \Phi}{\partial \phi}\right) + \frac{\partial^2 \Phi}{\partial z^2} \quad , \tag{C.2}$$

where

$$\Delta F_{D,\phi} = \frac{1}{a} \frac{\partial \Phi}{\partial \phi} \tag{C.3a}$$

and

$$\Delta F_{D,Z} = \frac{\partial \Phi}{\partial z} \tag{C.3b}$$

are the meridional and vertical components of the divergent part of the heat flux vector, respectively. The boundary conditions for Eq. (C.2) are

$$\Delta F_{D,Z} = \frac{\partial \Phi}{\partial z} = \begin{cases} \Delta FTS(\phi) & \text{at } z = 0 \\ 0 & \text{at } z = -D \end{cases} \tag{C.4}$$

where ΔFTS is the CO_2-induced ocean surface heat flux, and

$$\Delta F_{D,\phi} = \frac{1}{a}\frac{\partial \Phi}{\partial \phi} = 0 \qquad \text{at } \phi = \pm\frac{\pi}{2} \quad . \tag{C.5}$$

In the Southern Hemisphere the boundary condition for $\Delta F_{D,\phi}$ should be applied along the Antarctic coast. However, in this analysis the boundary condition is applied at the South Pole so that dependent variables can be represented as a sum of Legendre polynomials.

Equation (C.2) with boundary conditions (C.4) and (C.5) is a Poisson equation with Neumann boundary conditions, this system of equations requires that the compatibility condition

$$\int_{-D}^{0}\int_{-\pi/2}^{\pi/2} \rho c a \cos\phi \, \Delta T \, dz d\phi = \int_{-\pi/2}^{\pi/2} a\cos\phi \, \Delta FTS(\phi) d\phi \tag{C.6}$$

be satisfied for the solution to exist. This condition simply states that the change in the internal energy $\rho c \Delta T$ integrated over the entire fluid domain must equal the total flux of energy across the entire ocean surface.

We obtain the solution of Eq. (C.2) subject to equations (C.4)-(C.6) as follows. First, we substitute

$$x = \sin\phi \quad \text{and} \quad \frac{dx}{d\phi} = \cos\phi \tag{C.7}$$

into Eq. (C.2) to obtain

$$\rho c \Delta T = \frac{1}{a^2}\frac{d}{dx}\left[(1-x^2)\frac{\partial \Phi}{\partial x}\right] + \frac{\partial^2 \Phi}{\partial z^2}$$

$$= \frac{1}{a^2}\left[(1-x^2)\frac{\partial^2 \Phi}{\partial x^2} - 2x\frac{\partial \Phi}{\partial x}\right] + \frac{\partial^2 \Phi}{\partial z^2} \tag{C.8}$$

Because the differential operator in x of this equation is identical to that for the Legendre differential equation,

$$(1-x^2)\frac{d^2y}{dx^2} - 2x\frac{dy}{dx} + n(n+1)y = 0 \quad , \tag{C.9}$$

where n is the degree, we represent Φ as the sum of the eigenfunctions for Eq. (C.8), the Legendre polynomials $P_n(x)$, times expansion coefficients R_n which are function of z,

$$\Phi = \sum_{n=0} R_n(z)\, P_n(x) \quad . \tag{C.10}$$

Subtituting Eq. (C.10) into Eq. (C.8) gives

$$\rho c \Delta T = \sum_{n=0} \left\{ \frac{R_n(z)}{a^2} \left[(1-x^2) \frac{d^2P_n(x)}{dx^2} - 2x \frac{dP_n(x)}{dx} \right] \right.$$

$$\left. + P_n(x) \frac{d^2R_n(z)}{dz^2} \right\} \quad . \tag{C.11}$$

Then, using Eq. (C.9) with $y = P_n(x)$ we obtain

$$\rho c \Delta T = \sum_{n=0} \left[\frac{d^2R_n(z)}{dz^2} - \frac{n(n+1)}{a^2} R_n(z) \right] P_n(x) \quad . \tag{C.12}$$

Next, we expand ΔT in terms of Legendre polynomials as

$$\Delta T(\phi, z) = \sum_{m=0} B_m(z)\, P_m(x) \tag{C.13}$$

where $B_m(z)$ are the expansion coefficients which are functions of z. Subtituting Eq. (C.13) into Eq.(C.12) gives

$$\rho c \sum_{m=0} B_m(z)P_m(x) = \sum_{n=0} \left[\frac{d^2R_n(z)}{dz^2} - \frac{n(n+1)}{a^2} R_n(z)\right]P_n(x). \qquad (C.14)$$

Since the Legendre polinomials are orthognal on the interval $-1 \leq x \leq 1$, that is,

$$\int_{-1}^{1} P_n(x)P_m(x)dx = \delta_{nm} \quad , \qquad (C.15)$$

where δ_{nm} is the Kronecher δ. Eq. (C.14) can be satisfied only if

$$\rho c B_n(z) = \frac{d^2R_n(z)}{dz^2} - \frac{n(n+1)}{a^2} R_n(z), \; n = 0, 1, 2, \ldots \qquad (C.16)$$

These equations are a set of ordinary differential equations in z.

Similarly, we expand ΔFTS in a series of Legendre polinomials,

$$\Delta FTS(\phi) = \sum_{j=0} FT_j P_j(x) \qquad (C.17)$$

where the FT_j are the expansion coefficients. Subtituting this and Eq. (C.10) into Eq. (C.4) and using Eq. (C.15) then gives

$$\frac{dR_n(z)}{dz} = \begin{cases} FT_n & \text{at } z = 0 \\ 0 & \text{at } z = -D \end{cases} \qquad n = 0, 1, 2, 3, \ldots . \qquad (C.18)$$

The second boundary condition Eq. (C.5) is automatically satisfied by the Legendre polynomials in the expansion Eq. (C.10) for Φ.

Substituting Eqs. (C.13) and (C.17) into Eq. (C.6) gives for the compatibility condition

$$\sum_{m=0} \rho c \int_{-D}^{0} \int_{-1}^{1} aB_m(z)P_m(x)dxdz = \sum_{j=0} \int_{-1}^{1} aFT_jP_j(x)dx \qquad (C.19)$$

Noting from Eq. (C.14) with m = 0 and $P_o(x) = 1$ that

$$\int_{-1}^{1} P_n(x)dx = \begin{cases} 0 & n \neq 0 \\ 2 & n = 0 \end{cases} , \tag{C.20}$$

the compatibility condition becomes

$$\int_{-D}^{0} \rho c \, B_o(z)dz = FT_o \quad . \tag{C.21}$$

To solve Eq. (C.16) subject to the boundary conditions Eq. (C.18) and the compatibility condition Eq. (C.21), we employ finite differences to represent the derivatives. Thus, using centered differences, Eq. (C.15) can be written as

$$\tau_i(R_n)_{i-1} - (\tau_i + \beta_i + \alpha^2)(R_n)_i + \beta_i(R_n)_{i+1} = -\rho c(B_n)_i \tag{C.22}$$

$n = 0, 1, 2, \ldots$ and $i = 2, 3, 4, 5$.

Here i is the index of the vertical layers of the ocean model, with i = 1 and 6 representing the top and bottom layers, respectively, with z is the thickness of layer i, and

$$\tau_i = \frac{2}{\Delta z_i(\Delta z_i + \Delta z_{i-1})} , \tag{C.23a}$$

$$\beta_i = \frac{2}{\Delta z_i(\Delta z_i + \Delta z_{i+1})} , \tag{C.23b}$$

$$\alpha^2 = \frac{n(n+1)}{a^2} \quad . \tag{C.23c}$$

The boundary conditions Eq. (C.17) are, using one-sected differences,

$$(R_n)_{\frac{1}{2}} = (R_n)_1 + FT_n \frac{\Delta z_1}{2} \tag{C.24a}$$

and

$$(R_n)_{\frac{13}{2}} = (R_n)_6 \quad . \tag{C.24b}$$

Equation (C.22) with Eqs. (C.23) and (C.24) are solved individually for n = 1,2 ... using the Gauss elimination method. However, for n = 0 a solution of these equations that satisfies the compatability condition Eq. (C.21) exists only if Δz_i is constant. One way to solve this problem would be use more points in the finite-difference representation of the derivatives and use the increased degrees of freedom thereby attained to satisfy Eq. (C.20) rather than to increase the order of accuracy as usually done. However, here we have taken the simple expedicent approach of interpolating linearly in the vertical direction to a uniform vertical grid with Δz = 200 m.

Having now obtained the solution for the potential Φ, the heat fluxes $\Delta F_{D,\phi}$ and $\Delta F_{D,z}$ are given by Eqs. (C.4), (C.10) and the recurrence relation

$$\begin{aligned}(1-x^2)P'_n(x) &= nP_{n-1}(x) - nxP_n(x) \\ &= (n+1)xP_n(x) - (n+1)P_{n+1}(x)\end{aligned} \tag{C.25}$$

as

$$\Delta F_{D,\phi} = \frac{1}{a}\frac{\partial \phi}{\partial \phi} \tag{C.26}$$

$$= \begin{cases} \frac{1}{a}\sum_{n=0} R_n(z)\left[\frac{1}{\sqrt{1-x^2}}\left((n+1)xP_n(x) - (n+1)P_{n+1}(x)\right)\right] & x \neq \pm 1 \\ 0 & x = \pm 1 \end{cases} \tag{C.27}$$

and

$$\Delta F_{D,z} = \frac{\partial \phi}{\partial z} \tag{C.28}$$

$$= \sum_{n=0} \frac{dR_n(z)}{dz} P_n(x) \tag{C.29}$$